SWEET NANOMEDICINE IN VIVO: GLYCONANOPARTICLE FOR IMAGING AMYLOID BETA FIBRILS IN ALZHEIMER'S DISEASE, AND HYALURONAN NANOPARTICLES FOR IMAGING AND THERAPY OF INFLAMMATORY ATHEROSCLEROSIS DISEASE

By

Seyedmehdi Hossaini Nasr

A DISSERTATION

Submitted to
Michigan State University
in partial fulfilment of the requirements
for the degree of

Chemistry-Doctor of Philosophy

2018

ABSTRACT

SWEET NANOMEDICINE IN VIVO: GLYCONANOPARTICLE FOR IMAGING AMYLOID BETA FIBRILS IN ALZHEIMER'S DISEASE, AND HYALURONAN NANOPARTICLES FOR IMAGING AND THERAPY OF INFLAMMATORY ATHEROSCLEROSIS DISEASE

By

Seyedmehdi Hossaini Nasr

This dissertation is about design and synthesis of glyconanoparticles for certain *in vivo* applications including imaging amyloid beta fibrils in Alzheimer's disease, imaging inflammatory atherosclerotic plaques and inhibition of atherosclerotic plaque inflammation. Amyloid beta (Aβ) accumulation and deposition in the brain tissue are one of the most important hallmarks of Alzheimer's disease (AD). Therefore, Aβ is an attractive target for imaging AD, however, designing a nanoprobe with the ability to pass through the blood brain barrier (BBB) and reaching Aβ plaques is a significant challenge. The first part of this dissertation covers the synthesis of a glyconanoparticle enabling to pass the BBB and bind with Aβ fibrils. Briefly, synthesis, characterization and application of this glyconanoparticle for magnetic resonance imaging (MRI) of Aβ plaques in a mouse model of AD (B6C3) have been presented.

Majority of patients that experience cardiac arrests have atherosclerosis, which is the inflammatory disease of arterial walls and the major cause of heart attacks and strokes. Imaging techniques that can enable detection of atherosclerotic plaques before clinical manifestation are urgently needed. CD44 is a cell surface protein overexpressed in the plaque tissues and its expression level is associated with the risk of plaque rupture. The second chapter explains atherosclerosis disease and nanomedicine for targeting inflammatory atherosclerotic plaques. The third chapter of this dissertation presents the development of hyaluronan (HA) coated iron oxide nanoparticles for active targeting of the plaques. These nanoprobes can not only bind with atherosclerotic plaques through their HA ligands but also function as T_2 based MRI contrast agents for plaque diagnosis.

Moreover, the effect of nanoprobe morphology on inflammation has been studied indicating that engineering nanoprobe shape could decrease inflammatory responses, which makes it a superior candidate for imaging inflammatory atherosclerotic plaques. Concisely, design and synthesis of HA conjugated nanoworm (HA-NW) have been explained. Then, inflammatory responses to HA conjugated nanoparticles in vitro and *in vivo* in apoE knockout mouse model have been presented. Finally, the ability of HA-NW for *in vivo* imaging of atherosclerotic plaques by MRI has been studied.

The last part of this dissertation goes over design and synthesis of hyaluronan conjugated atorvastatin nanoparticle (HA-ATV NP). This therapeutic formulation has been designed to deliver ATV to the inflammatory atherosclerotic plaques to reduce plaque inflammation. Then, HA-ATV NP anti-inflammatory effects in vitro and its therapeutic effect *in vivo* in apoE knockout mouse model have been explained. It has been shown that intravenous administration of this formulation (high dose, 8.5 mg ATV/ kg), every other day for one week can significantly reduce the plaques inflammation.

Dedicate to my mom and dad (Mah Soltan & Mohammad), my brother (Saeed), and my sister (Zoha) for their endless support and kindness.

ACKNOWLEDGEMENTS

First, I would like to thank my advisor Prof. Xuefei Huang for all his support and mentorship during my PhD study. Undoubtedly, Prof. Huang is one of the most influential people in my life specially in the development of my academic characteristic. I feel extremely grateful to him not only for his immense knowledge and brilliant thinking but also for his patience and motivation during my PhD training.

Then, I would like to express my gratitude to my guidance committee Prof. Babak Borhan, Prof. Erik M. Shapiro and Prof. Heedeok Hong. Although, I have learnt a lot from Prof. Borhan, but also his humanistic attitude was always encouraging and heartwarming for me. I would like to thank Prof. Erik M. Shapiro for his generous support toward my PhD projects. I really appreciate his deep knowledge in nanomedicine and imaging fields which helped me a lot accomplishing my research projects. A special thank goes to Prof. Heedeok Hong and his group for being always nice, professional and helpful to me.

My sincere thanks also goes to Prof. Chunqi Qian for his priceless help specially for imaging studies related to the atherosclerotic projects. Besides, I would like to thank Prof. Robert Wiseman and Prof. David C. Zhu for their support on imaging studies. Then, I would like to thank Prof. Narayanan Parameswaran and his lab for training me doing molecular biology assays. A special thanks goes to Prof. Kurt Zinn for providing generous access to his laboratory facilities.

I would like to thank Dr. Christiane Mallett, Dr. Anne Tonson, Dr. Mohammad H. El-dakdouki and Dr. Sherif Ramadan for all I have learnt from them.

I am very thankful to my present and past labmates: Herbert, Steve, Zhaojun, Berm, Weizhun, Xuanjun, Tianlu, Kedar, Setare, Peng, Qian, Changxin, Jingguang, Zahra, Zeren, Jicheng, Zibin, Mengxia, Hunter, Kunli, Shuyao, Jia and Shivangi for being excellent team members during my PhD years. Moreover, I would like to appreciate undergraduate and high school students Joe Sheena, Anthony Smith, Nicole Desmet, Ryan Taggarse and Carol Wu for their inspiring attitude towards research.

I would like to express my appreciation to Dr. Rouzbeh Eskandari and Dr. Hovig Kouyoumdjian two great friends for all the motivation and inspiration with my PhD challenges. I am also thankful to my friends Alborz, Nariman, Ali Akbar, Alireza, Hadi, Rasoul, Kiana, Olivia, Anthony and Mohammad for all the years of friendship here in MSU and of course many other friends who made contributions on the family's behalf.

Then, my highest level of gratitude and appreciation goes to my mom and dad for all their endless support and kindness. I would like to thank them for the ethical and humanistic values they have taught me during my life and I am also very thankful to my dear brother Saeed and the angel of my family Zoha (my dear sister) for their encouraging and understanding attitude.

And finally, I would like to apologize to everybody who I might have hurt by my actions

or by my words during my years at the graduate school.

THANK YOU...

TABLE OF CONTENTS

LIST OF TABLES

LIST OF FIGURES

KEY TO ABBREVIATIONS

Aβ (amyloid β)

AD (Alzheimer's disease)

ApoE (Apolipoprotein E)

ATV (Atorvastatin)

BSA (bovine serum albumin)

Cox-2 (cyclooxygenase-2)

CRP (C-reactive protein)

CSF (cerebrospinal fluid)

CDMT (2-chloro-4,6-dimethoxy-1,3,5-triazine)

DLS (dynamic light scattering)

DMEM (Dulbecco's Modified Eagle Medium)

ECH (epichlorohydrin)

EDCI (ethyl-(3,3-dimethylaminopropyl) carbodiimide hydrochloride)

ELISA (enzyme linked immunosorbent assay)

FBS (fetal bovine albumin)

FITC (fluorescein isothiocyanate)

GM1 (monosialotetrahexosyl ganglioside)

HA (Hyaluronic acid)

HA-ATV NP (Hyaluronic acid conjugated atorvastatin nanoparticle)

HA-SPION (Hyaluronic acid conjugated superparamagnetic iron oxide nanoparticle)

HA-NW (Hyaluronic acid conjugated nanoworm)

HDL (High-density lipoprotein)

HRP (horseradish peroxidase)

ICAM-1 (intercellular adhesion molecule 1)

ICP (inductively coupled plasma)

ID/g (injected dose per gram)

IL-1α (interleukin 1 alpha)

IL-1β (interleukin 1 beta)

iNOS (inducible nitric oxide synthases)

LDL (High-density lipoprotein)

LPS (lipopolysaccharide)

mAb (monoclonal antibody)

MCP-1 (Monocyte chemoattractant protein 1)

MRI (magnetic resonance imaging)

MTS (3-(4,5-dimethylthiazol-2-yl)-5-(3-carboxy-methoxyphenyl)-2-(4-sulfophenyl)-2H-tetrazolium)

MWCO (molecular weight cutoff)

NP (nanoparticle)

NP-BSAx-Sia (sialic acid coated bovine serum albumin nanoparticle)

NW (Nanoworm)

NMM (N-methylmorpholine)

PAMAM (polyamidoamine)

PBS (phosphate buffered saline)

PCSK-9 (proprotein convertase subtilisin/kexin type 9)

PET (positron emission tomography)

ROI (region of interest)

ROS (reactive oxygen species)

RQ (relative quantification)

rt-PCR (real time polymerase chain reaction)

Sia (sialic acid)

SPION (Superparamagnetic iron oxide nanoparticle)

SPP1 (secreted phosphoprotein 1)

^{99m}Tc (Technetium 99)

TEER (transendothelial electrical resistance)

TEM (transmission electron microscope)

Tg (transgenic)

TGA (Thermal Gravimetric Analysis)

TMAOH (tetramethylammonium hydroxide)

TMB (3,3′,5,5′-tetramethylbenzidine)

TNFα (tumor necrosis factor alpha)

Chapter 1: Amyloid Beta Fibril Detection in an Animal Model of Alzheimer's Disease Using Glyconanoparticle

Adapted with permission from:

Detection of β-Amyloid by Sialic Acid Coated Bovine Serum Albumin Magnetic Nanoparticles in a Mouse Model of Alzheimer's Disease, Seyedmehdi Hossaini Nasr, Hovig Kouyoumdjian, Christiane Mallett, Sherif Ramadan, David C. Zhu, Erik M. Shapiro, and Xuefei Huang. *Small*, **2018**, 14, 1701828. Copyright (2018) John Wiley & Sons.

1.1. Introduction

Alzheimer's disease (AD) is the most common type of dementia. Studies by the Alzheimer's Disease International Institute indicate that in 2016, about 47 million people worldwide lived with dementia and this number is expected to rise to 132 million in 2050[1-3]. The economic impact of AD is estimated to be $818 billion in 2016. These staggering numbers suggest new methods for diagnosis and treatment of AD are urgently needed, and early detection of AD can potentially improve the prognosis for AD patients[4-5].

The accumulation and deposition of β-amyloid (Aβ) peptides in brain tissues are one of the most distinctive hallmarks of AD[6]. Strong correlations have been found between Aβ deposition and the beginning of atrophy at early stage of AD[7]. As a result, Aβ has been an attractive target for the development of non-invasive methods for AD detection. Positron Emission Tomography (PET) has been used clinically for AD brain imaging[8]. Pittsburgh Compound-B[9-10] is a ^{11}C containing PET tracer that can selectively bind with β-sheeted Aβ aggregates, which has been approved by FDA for imaging Aβ plaques in brains. However, PET has inherent low spatial resolution and utilizes ionizing radiation. An appealing alternative for Aβ imaging is Magnetic Resonance Imaging (MRI) due to its non-invasive nature and high spatial resolution. Advanced Aβ plaques can be detected directly via MRI due to the accumulation of iron ions in plaque tissues leading to contrast changes from the surrounding tissues[11-14]. For early plaque detection, the inherent contrast associated with the plaques is not sufficient. Thus, contrast agents are needed to enable plaque imaging by MRI, which are most commonly delivered by nanoparticles (NPs)[15-20].

One significant challenge in Aβ imaging using NP contrast agents is the blood brain barrier (BBB), which has tight junctions between endothelial cells lining the blood vessels in the brain[21-22] and severely limits entries of macromolecules such as NPs into brains[21, 23]. In order to overcome this,

a common approach is to add mannitol into the NP formulation, which transiently opens up the BBB allowing particles to diffuse into brain tissues[24-25]. However, it is challenging to apply this approach to humans due to the concern for possible brain infections with the opened BBB. NPs that are able to penetrate the BBB without the need for mannitol are desirable for Aβ imaging.

To facilitate selective binding of NPs to Aβ plaques, Aβ targeting agents are needed to functionalize the NPs. The most extensively utilized ones are either full length or fragments Aβ as these peptides can aggregate with Aβ plaques thus enriching contrast agents in plaque sites[15, 18-19, 25-26]. Wadghiri and coworkers pioneered Aβ coated magnetic NPs to image Aβ in mouse models of AD[18]. A potential drawback using Aβ based targeting vectors is the concern that they can possibly lead to further growth of plaques. Alternatively, Aβ binding monoclonal antibodies (mAbs) have been explored as targeting agents[27]. However, besides their high costs and potential immunogenicities, the use of mAbs has side effects[28]. For instance, the administration of anti-Aβ mAbs Bapineuzumab and Gantenerumab increased the risk of amyloid related imaging abnormalities of brains, including chronic brain hemorrhages and swelling of brains[29-30]. Small molecules such as curcumin[31] and Congo red[32] have been tested as Aβ targeting agents. NPs bearing these ligands require mannitol to facilitate their entries into brain tissues.

Sialic acid is an interesting ligand for Aβ binding studies[33]. Sialic acid is a monosaccharide with a nine-carbon backbone, which is mostly found at terminal ends of saccharide chains such as gangliosides rich in the nervous system[34]. Located on neuronal membranes, monosialotetrahexosyl ganglioside (GM1) is the most abundant ganglioside in the brain. Studies have shown that residues His13 to Leu17 located at the N-terminal of the Aβ peptide are important for their interactions with GM1 and His13 is responsible for specific interaction with the sialic acid moiety of GM1[35-38]. By binding with Aβ, exogenous GM1 can inhibit Aβ induced cytokine release and inflammatory

responses by neuronal cells[39]. The intrinsic ability of sialic acid to bind with Aβ fibrils and its biocompatibility make it suitable for Aβ studies, especially when multiple copies of it can be placed on a nanostructure resulting in enhanced avidities[33]. Sialic acid conjugated second generation polyamidoamine (PAMAM) dendrimers were found to decrease Aβ toxicity towards SH-SY5Y neuroblastoma cells[40-41]. While increasing the multivalency of these dendrimers improved Aβ binding, third and fourth generation PAMAM dendrimers caused cell death due to their inherent cellular toxicities limiting their utility *in vivo*. Other sialic acid bearing NP platforms investigated for Aβ studies include gold nanoshells deposited on carbon electrode[42], chitosan polysaccharides[43] and magnetic NPs[44]. No in vivo studies have been reported using these constructs presumably due to either the inherent toxicity of the carrier or the limited abilities to pass the BBB[41, 43, 45].

Herein, we report the synthesis of sialic-acid-functionalized bovine serum albumin (BSA) coated magnetic NPs (NP-BSAx-Sia). As crossing BBB is a significant barrier for brain imaging, NP-BSAx-Sia can overcome this roadblock, pass through BBB and bind with Aβ peptide with high selectivities. Furthermore, administration of this probe to AD mice enables *in vivo* detection of AD plaques through MRI without the need for mannitol to open the BBB. This is the first time that sialic acid NPs have been utilized to image Aβ *in vivo*. The high biocompatibility, magnetic relaxivity, and Aβ selectivity coupled with its ability to cross the BBB render NP-BSAx-Sia a promising contrast agent for non-invasive imaging of Aβ.

1.2. Synthesis and characterization of NP-BSAx-Sia

The synthesis of NP-BSAx-Sia started from the preparation of iron oxide NPs through the thermal decomposition method[46]. Heating a mixture of $Fe(acac)_2$ and hexadecanediol in the presence of oleic acid and oleylamine from 200 - 300 ^{o}C in benzyl ether formed magnetite NPs (Figure 1). The

hydrophobic particles were rendered water soluble through ligand exchange with tetramethylammonium hydroxide (TMAOH) followed by incubation with BSA[47], which can non-covalently absorb on the surface of the NPs providing a protein layer for further functionalization. The resulting NPs were incubated with 2,2'-(ethylenedioxy)bis(ethylamine) **1** and ethyl-(3,3-dimethylaminopropyl) carbodiimide hydrochloride (EDCI), which could covalently crosslink the carboxylic acids of immobilized BSA through amide bond formation leading to NP-BSAx. Sialic acid was then introduced onto the NPs through EDCI mediated amide bond formation with sialic acid derivative **2**,[44] followed by subsequent ester hydrolysis generating the NP-BSAx-Sia. The prepared NPs were further labeled when needed with the fluorophore fluorescein isothiocyanate (FITC) by presumably reacting with residual amines on NP-BSAx-Sia to form NP-BSAx-Sia-FITC enabling their tracking by fluorescence for cellular experiments.

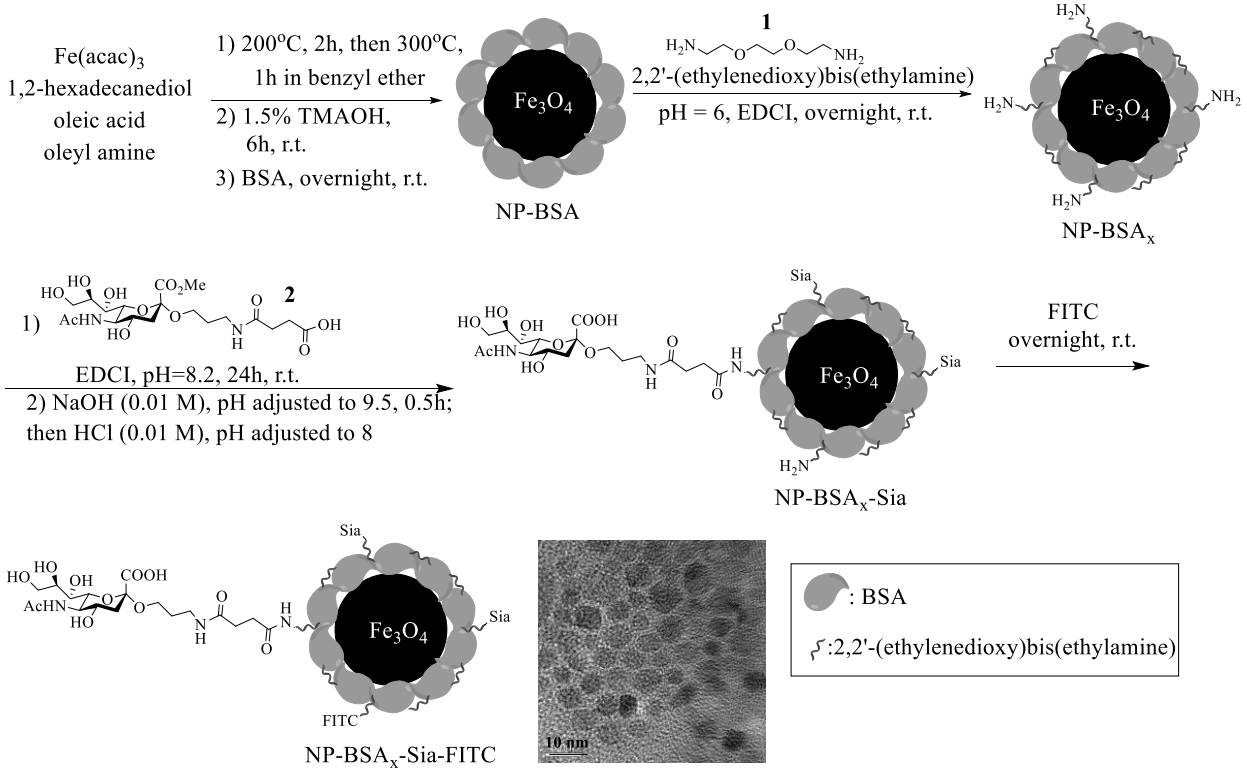

Figure 1-1. Synthesis of NP-BSAx-Sia and NP-BSAx-Sia-FITC. The scale bar for TEM image is 10 nm.

The NPs were characterized with a variety of methods. The average core diameters of the NPs were 5 nm as determined by transmission electron microscopy (TEM) **Figure 1-1** with an average hydrodynamic diameter of 87 nm in PBS buffer analyzed by dynamic light scattering (DLS). The cationization of BSA through amination is important to facilitate BBB crossing[47-48]. Zeta potential (ζ) surface charge measurements was a convenient method to monitor the amination process. The BSA coated magnetic NPs as synthesized had a negative zeta potential of -6.6 mV in PBS buffer. Upon reaction with diamine **1**, ζ values increased to +11.2 mV suggesting the successful introduction of amines onto the NPs. The number of 2,2'-(ethylenedioxy)bis(ethylamine) reacted with BSA was analyzed by mass spectrometry of BSA functionalized in solution under the identical reaction condition as NP modification. Based on the molecular weight difference of BSA before and after functionalization, the average number of diamine **1** introduced was estimated to be 33 per BSA molecule **Figure 1-2**. However, the maximum theoretical possible number of diamine per BSA molecule is 99.

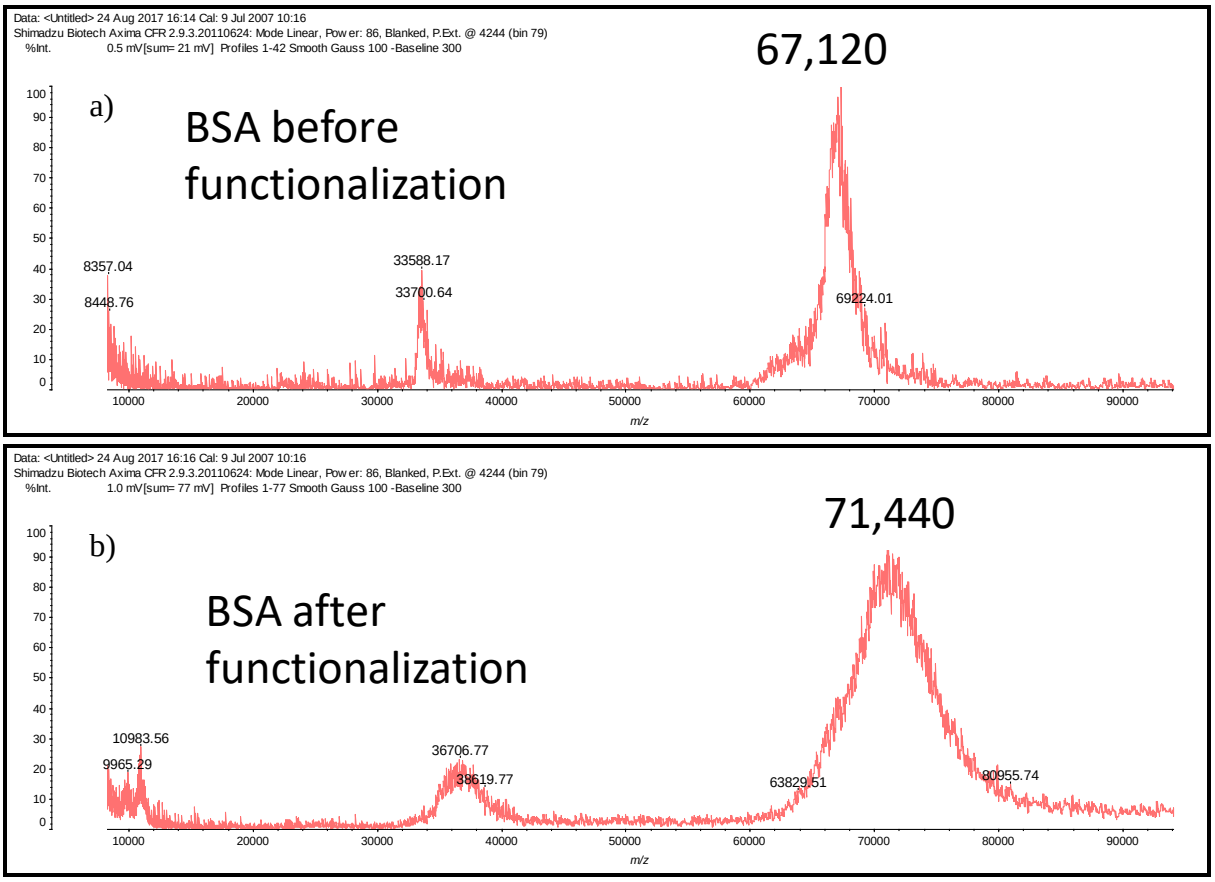

Figure 1-2. MALDI-MS of BSA (a) before and (b) after reaction with 2,2'-(ethylenedioxy)bis(ethylamine) **1**. Functionalization with diamine **1** caused the average molecular weight of BSA to increase from 67,120 to 71,440. This mass change corresponds to on average the addition of 33 molecules of **1** to each BSA following amide formation.

Amidation of NP-BSAx with sialic acid lowered the ζ value to +5.2 mV indicating the conversion of some of the positively charged amines to neutral amides. The total organic content was determined by thermogravimetric analysis (TGA) to be 74% of the weight of the NP-BSAx-Sia **Figure 1-3a**. The amount of sialic acid on NP-BSAx-Sia was quantified by thiobarbituric acid assay[49] following mild acid treatment of the NPs to cleave off the sialic acid. The amount of sialic acid accounted for 7% of the weight of NPs with an average of 118 sialic acid molecules per NP-

BSAx-Sia. The NP-BSAx-Sia has high magnetic relaxivities with an r_2* value of 220 L mmol^{-1}s^{-1} (7 Tesla) suggesting these particles are good T_2* based MRI contrast agents **Figure 1-3b**. The NPs are colloidal stable as there were little changes in their hydrodynamic sizes or surface charges when kept in solution for more than three weeks **Figure 1-3c**.

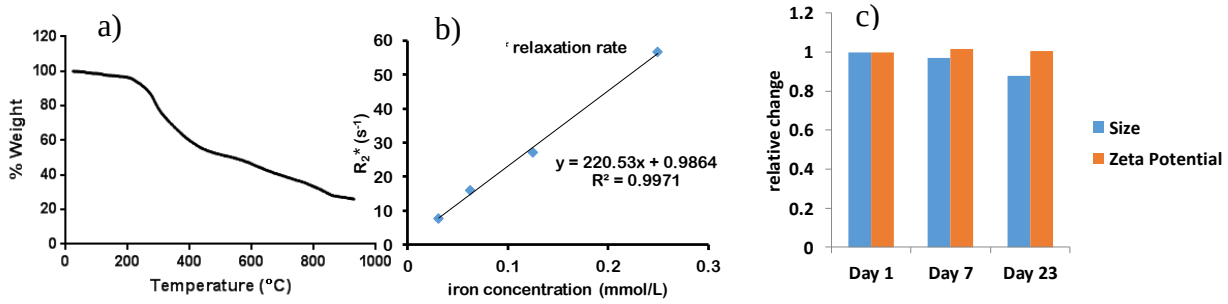

Figure 1-3. (a) Thermogravimetric analysis (TGA) of NP-BSAx-Sia; (b) r_2* relaxivity measurement of NP-BSAx-Sia; and (c) There were little changes in size and zeta potential for NP-BSAx-Sia in PBS over 23 days indicating the colloidal stability of the NPs.

1.3. NP-BSAx-Sia Was Biocompatible and Non-toxic to Cells

For *in vivo* applications of NPs, it is critical that the particles are biocompatible. Brain endothelial cells are a critical component of the BBB that controls passages of exogenous molecules into the brain[50]. Damages to this barrier can expose the brain to a variety of harmful compounds that are normally excluded from the brain. To evaluate their biocompatibilities, NP-BSAx-Sia and NP-BSAx were incubated with brain endothelial cells bEnd.3 and their effects on cell viabilities were analyzed using the 3-(4,5-dimethylthiazol-2-yl)-5-(3-carboxy-methoxyphenyl)-2-(4-sulfophenyl)-2H-tetrazolium (MTS) cell viability assay. As shown in **Figure 1-4**, with concentrations examined up to 1 mg/mL, NP-BSAx-Sia did not have any adverse effects on cell viability. In contrast, cells incubated with NP-BSAx above 0.25 mg/mL exhibited reduced viability with only 40% alive at 1

mg/mL of NP-BSAx. These results indicate that NP-BSAx-Sia has good biocompatibility and NP-BSAx is not suitable for *in vivo* applications due to potential toxicities.

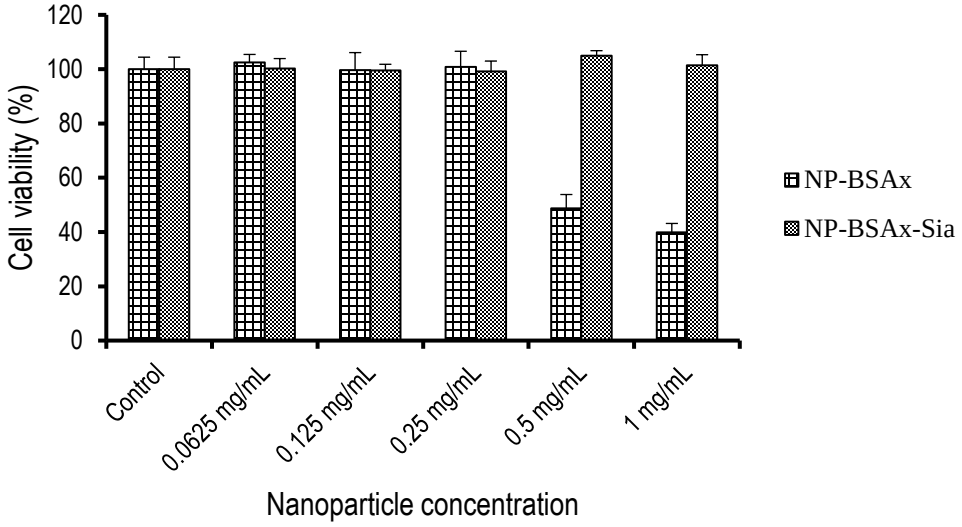

Figure 1-4. Viability of bEnd.3 cells following treatment with various concentrations of NP-BSAx and NP-BSAx-Sia. While NP-BSAx exhibited cytotoxicity above 0.25 mg/mL, NP-BSAx-Sia did not cause any toxicities in the concentrations examined.

1.4. NP-BSAx-Sia Enabled In Vivo Imaging of Aβ Plaques in A Human AD Mouse Model

To test the possibility of Aβ detection *in vivo*, a human AD model utilizing double transgenic (Tg) mice was established. These mice express a chimeric mouse/human amyloid precursor protein (Mo/HuAPP695swe) and a mutant human presenilin 1 (PS1-dE9) at central nervous system neurons. Both mutations are associated with early-onset AD. These mice secrete human Aβ peptides, which are known to form Aβ plaques as those in humans[51-52].

Tg mice in the age range of 39 to 42 weeks were used for *in vivo* Aβ plaque detection studies. When these mice were imaged directly by T_2* weighted MRI using a 3D gradient echo sequence, no abnormalities could be observed suggesting plaques were invisible under this condition **Figure**

1-5b,d. Following administration of NP-BSAx-Sia, contrast changes in brains were continuously monitored by MRI. Distinct dark spots due to loss of signals were observed in multiple slices of the brain in both cortex and hippocampus regions 1 hour after injection of NP-BSAx-Sia **Figure 1-5e** and **Figure 1-6**. The relative contrast changes reached their maximum values between 1-3 hours. The signal changes lasted more than one day with the intensities returning to pre-injection levels after 72 hours **Figure 1-5a**. Multiple slices and locations showed significant signal decreases upon NP-BSAx-Sia administration **Figure 1-5c,e, Figure 1-6** and **Figure 1-7d**. The signal changes were not due to presence of NPs in the blood as the signal intensities from the brain blood vessels returned to basal levels two hours after NP administration **Figure 1-5** and **Figure 1-8**.

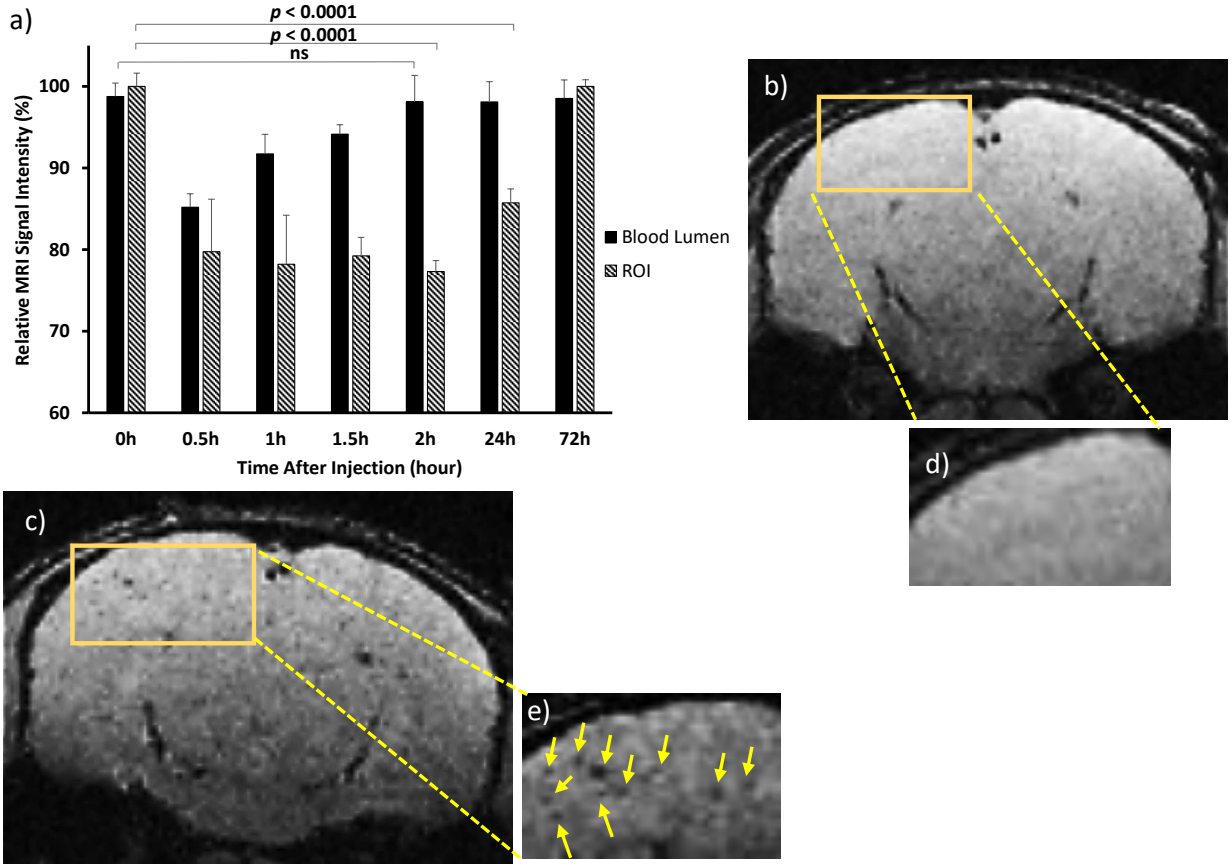

Figure 1-5. T_2* weighted MRI signal intensity changes of Tg mouse brain before and after administration of NP-BSAx-Sia. Mice were scanned at different time intervals (0.5, 1, 1.5, 2, 24

Figure 1-5 (cont'd) and 72 hours) after NP administration. a) Quantification of relative signal intensity changes in one region of interest (ROI) vs blood vessel in the brain. The observed signal changes in the region of interests were presumably due to NP binding with Aβ plaques, not from the blood pool effect as contrast of brain blood vessels returned to basal levels two hours after NP administration. The contrast changes in region of interest lasted more than 24 hours. Statistical analysis was performed using student t test. Selected MR images showing contrast changes. MR images of mouse brain b) before NP injection; and c) 1.5 hours after NP injection. d) Expansion of the boxed region of figure b; e) Expansion of the boxed region of figure c. The arrows indicate the location of contrast change.

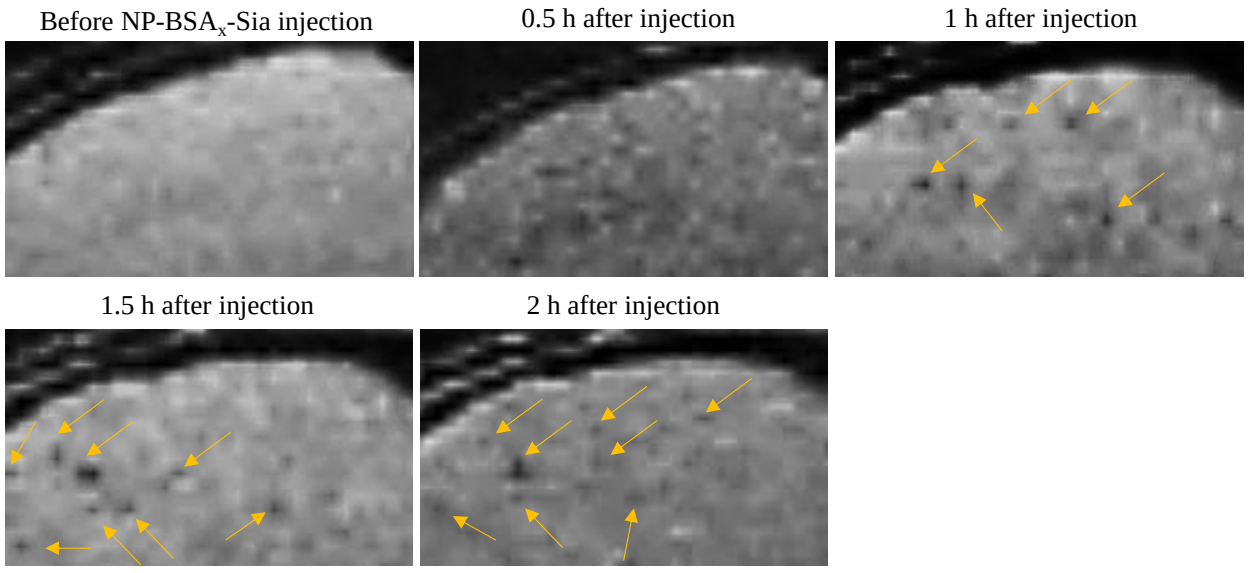

Figure 1-6. In vivo MRI of Tg mouse brain before and after injection of NP-BSAx-Sia showed signal loss in some spots in the brain presumably due to binding of particles with Aβ plaques. The animal was scanned at different time intervals (0.5, 1, 1.5, 2 hours) after injection.

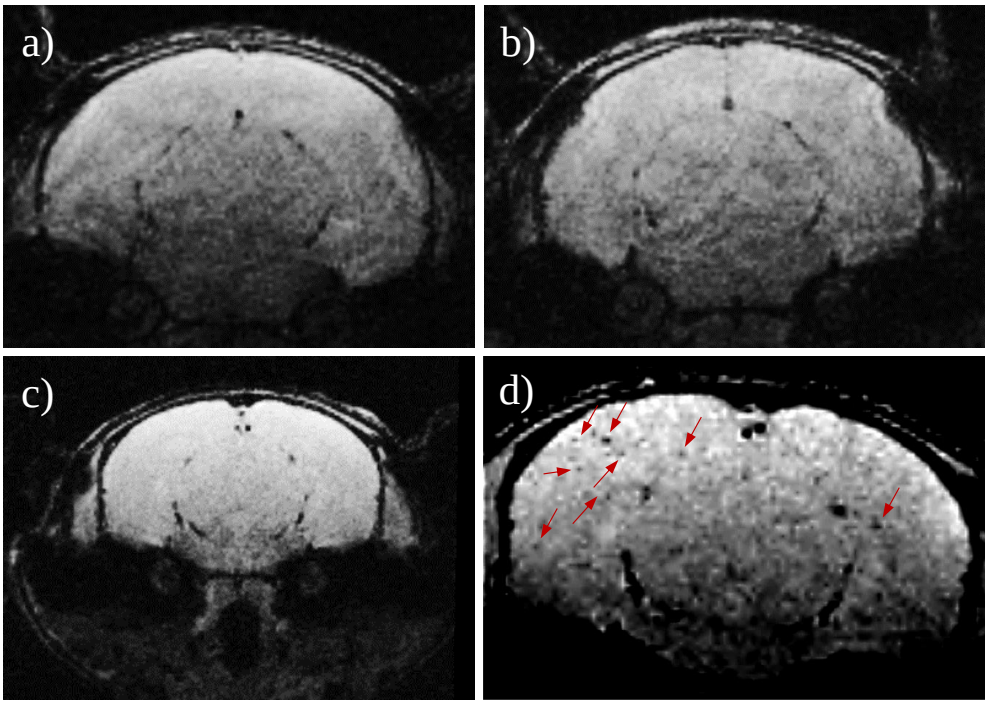

Figure 1-7. a) In vivo MRI of brain of a wild type mouse before and b) 1.5 hour after injection of NP-BSAx-Sia. (c) and (d) are images of a brain slice of Tg mouse. c) before and d)1.5 hour after injection of nanoparticles respectively. c) and d) are presented here to aid in comparison with the images (a and b) from wild type mice. Regions of interest of signal changes have been highlighted by red arrows.

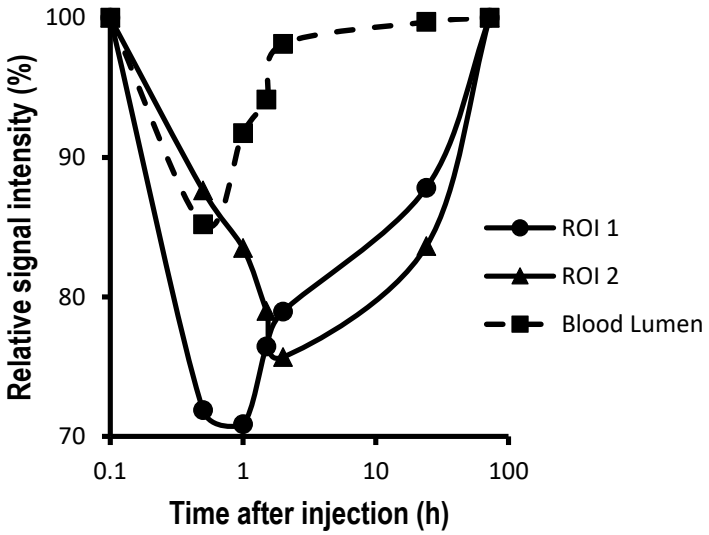

Figure 1-8. Relative MRI signal intensity changes for two ROIs presumably due to NP binding to Aβ plaques vs lumen of brain blood vessels.

For control experiments, NP-BSAx-Sia was injected to age matched wild type mice, which do not express human Aβ in the brain. In contrast to Tg mice, no hypo-intense spots were observed in T_2* weighted images of the brains of wild type mice **Figure 1-7a,b**. To further verify the importance of NP-BSAx-Sia in Aβ imaging, Feridex®, a type of commercially available superparamagnetic iron oxide NPs, were injected to Tg mice at the same dose of Fe (8 mg/kg) as NP-BSAx-Sia. No dark spots were observed in the brain in T_2* weighted images of these brains suggesting little Feridex® particles were retained in the brains of Tg mice **Figure 1-9**.

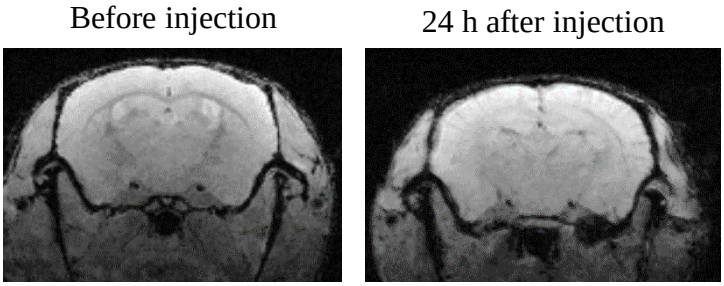

Figure 1-9. In vivo T_2* weighted MRI of Tg mouse brain after injection of Feridex®. Feridex® (8 mg/kg) was injected to Tg mouse then mouse brain was imaged. In contrast to Tg mouse receiving NP-BSAx-Sia, no significant local changes were observed in MRI suggesting little binding of Feridex to brain tissues.

1.5. Histological Analysis Confirmed the Presence of NP in Brains of Tg Mice After Administration of NP-BSAx-Sia

Four hours after injection of NP-BSAx-Sia to Tg mice, their brains were harvested and subjected to histological analysis. Thioflavin-s staining on AD brain slices showed punctate patterns of staining confirming the presence of Aβ plaques in these brains **Figure 1-10a,b** in contrast to wild type mice **Figure 1-10c**. Prussian blue staining showed the blue coloration on slices in hippocampus and cortex **Figure 1-10d,e** supporting the penetration and retention of NP-BSAx-Sia into the brain. In brains of wild type mice after NP administration, Prussian blue failed to show any blue staining **Figure 1-10f,g** consistent with MR images observed *in vivo* indicating the absence of NPs in these brains.

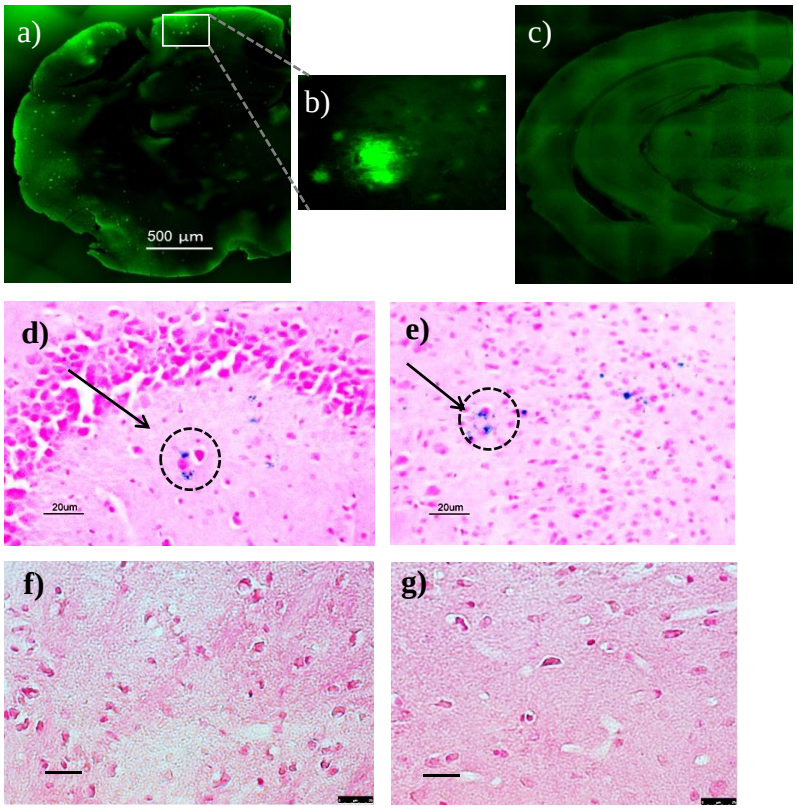

Figure 1-10. (a,b) Thioflavin-S staining of Tg mouse brain indicated the presence of Aβ deposition. The scale bar is 500 µm; (c) Thioflavin-S staining of wild type mouse brain showed no Aβ plaques. (d,e) Prussian blue staining of brain tissue from Tg mice following intravenous NP administration. Representative areas of Prussian blue staining are highlighted in the circles. The presence of blue staining confirms the presence of Fe in Tg mouse brain presumably due to NP accumulation. (d) showed the location of Fe near hippocampus and (e) in the cortex. (f-g) Wild type mouse brain after intravenous NP administration showed no Prussian blue staining due to the absence of NPs in the brains. Scale bars are 20 µm.

1.6. Discussion

While the etiology of AD has not been firmly established, AD detection based on biomarker such as Aβ can potentially provide early intervention of the disease to improve patient prognosis.

Samples from the cerebrospinal fluid (CSF) obtained through lumbar puncture can allow the analysis of fluids surrounding the brain reflecting key aspects of pathology[3]. The invasive nature of this approach renders it not ideal for routine evaluation of AD. Compared to CSF, blood samples are more readily available. However, extensive research aimed at identifying blood-based biomarkers has not led to satisfactory results[53-55]. With the possibility of directly imaging Aβ, MRI based neuroimaging methods aided by NP contrast agents provide an attractive alternative for early detection of AD.

One significant hurdle in delivering NPs to the central nervous system is the BBB, due to the tight junctions between brain endothelial cells lining brain vascular vessels. NPs including magnetic NPs have been shown to bind Aβ *in vitro*[44, 56-57]. However, presumably due to their poor abilities to penetrate into brains, they are not useful for *in vivo* brain imaging. These results are consistent with our observations using the iron oxide magnetic NP Feridex®, as no significant contrast changes have been observed in T_2* weighted images of AD mouse brains after administration of Feridex® and clearance of the particles from blood circulation **Figure 1-9**. It is well known that pegylation can passivate NPs and improve their tissue penetration[58]. PEG molecules have been installed on Aβ(1-42) peptide bearing iron oxide NPs, which enhanced their abilities to cross the BBB. One drawback is that retention of these NPs has also been observed in brains of normal mice in T_2* weighted MR images, which can possibly produce false positive identification[15].

Receptor mediated transcytosis is another strategy to facilitate BBB penetration, which immobilizes ligands on NPs to target endocytic receptors expressed on brain endothelial cells[59]. The efficiency of transport across the BBB using this approach is restricted by the number of receptors exposed on brain endothelial cell surface. In addition, the ligand for binding the

endocytic receptor may compete against that for Aβ binding for the limited number of conjugation sites on NP surface, lowering targeting efficiency.

Biocompatibility is another important parameter for *in vivo* applications as some biological probes can cause significant toxicities. For example, cationic nanoparticles can not only disrupt cell membranes due to their interactions with negatively charged cell surface but also cause lysosomal and mitochondrial damages[60]. Glycosylation can be an effective approach to reduce the toxicities of probes[61]. In our study, the NP-BSAx showed significant toxicities to bEnd.3 cells at doses above 0.25 mg NP/mL **Figure 1-4**. For *in vivo* mouse imaging studies, 8 mg Fe/kg NP administered was equivalent to a blood concentration of 0.8 mg NP/mL suggesting the NP-BSAx was undesirable due to toxicity concerns. This difficulty is overcome by sialic acid functionalization of the NPs, which greatly improved biocompatibility of the NPs **Figure 1-4** while maintaining the abilities to transport across BBB.

Upon administration of NP-BSAx-Sia to AD mice, the region of interest-based quantitative measurement of T_2* values from the *in vivo* MRI showed significant reduction of T_2* values in both cortex and hippocampus areas of the brain attributed to NP binding to Aβ plaques **Figure 1-5**. The contrast changes lasted more than one day, which were not due to the presence of NPs in the blood as the contrast of the blood vessel lumen returned to pre-injection levels in about two hours **Figure 1-5a**. Histology studies also supported the retention of NPs in AD mouse brains **Figure 1-10**. In contrast to aforementioned PEGylated NPs, little NPs were found in normal mouse brains after administering with NP-BSAx-Sia **Figure 1-7**. Presumably in these mice, due to the absence of Aβ plaques, the NP-BSAx-Sia was not retained in brain tissues after BBB penetration.

1.7. Conclusion

Sialic acid coated BSA magnetic NPs were synthesized, which bound to Aβ deposit in brains with high selectivity. The NP-BSAx-Sia could penetrate through the BBB and enable detection of Aβ plaques using MRI in an AD mouse model without the need for mannitol to open up the BBB. This overcomes a significant hurdle in NP aided Aβ plaque imaging. Sialic acid functionalization of the NPs greatly improved the biocompatibility of the probe with enhanced Aβ binding avidity. With further development, such probes can aid in longitudinal monitoring of Aβ plaque development as well as the evaluation of potential novel therapeutic interventions to reduce Aβ plaque loads.

1.8. Experimental

1.8.1. Materials

Iron (III) acetylacetonate [$Fe(acac)_3$], oleyl amine, 1,2-hexadecanediol, oleic acid (OA), benzyl ether, BSA, ethyl-(3,3-dimethylaminopropyl) carbodiimide hydrochloride (EDCI), 2,2′-(ethylenedioxy)bis(ethylamine), tetramethylammonium hydroxide were purchased from Sigma-Aldrich and hydrogen peroxide (30%) was purchased from CCI. Amberlite IR 120 hydrogen form (Amberlite H^+) was purchased from Fluka. Buffered 10% formalin solution was purchased from Azer Scientific. Potassium ferrocyanide trihydrate ($K_4Fe(CN)_6.\ 3H_2O$) was purchased from Mallinckrodt. 3,3′,5,5′-tetramethylbenzidine (TMB) and 1,1,1,3,3,3-hexafluoro-2-propanol 99.9% were purchased from Acros Organics. Thioflavin T (ThT), UltraPure Grade was purchased from AnaSpec. Aβ(1-42) was purchased from GL Biochem. (Shanghai) Ltd. bEnd.3 endothelial cells were purchased from American Type Culture Collection (ATCC). Phosphate buffered saline (PBS), Dulbecco's modified Eagle medium (DMEM), sodium pyruvate (100 mM), glutamine,

penicillin−streptomycin (Pen Strep) mixture were purchased from Gibco. The anti-Aβ 1-16 (6E10) mAb, SIG-39320 was purchased from Covance, and goat anti-mouse HRP-conjugated secondary antibody was purchased from BioRad. Tween 20 was purchased from BioRad. CellTiter 96 Aqueous One solution containing MTS was purchased from Promega. Ultrathin-carbon type A, 400 mesh copper grids for TEM were purchased from Ted Pella, Inc. Ultrafiltration membranes and centrifugal filters were purchased from Millipore, while dialysis tubings were obtained from BioDesign Inc. bEnd.3 cells were cultured in DMEM. All cell culture media was supplemented with 10% inactivated FBS, 1% Pen-Strep mixture, and L-glutamine (2 mM).

1.8.2. Synthesis of Sia-BSAx-NP

The magnetic NPs were synthesized by conjugating the sialic acid moieties with the Fe_3O_4 magnetite magnetic NPs. The superparamagnetic nanocrystals were prepared via the thermal decomposition method[46]. Iron (III) acetylacetonate (2 mmol) were mixed with 1,2-hexadecanediol (10 mmol), oleic acid (6 mmol), and oleyl amine (6 mmol) in benzyl ether (40 mL), then heated for two hours at 200^{o}C following 1 hour reflux at 300^{o}C under argon flow. The oleic acid coated magnetic NPs were washed in ethanol (50 mL) three times then collected by centrifuge. The obtained NPs were dispersed in hexanes in the presence of oleic acid (50 μL) and oleylamine (50 μL) and centrifuged to precipitate large particles. Then, hexanes were removed by rotavap and NPs (10 mg) were dispersed in chloroform (5 mL) for ligand exchange with TMAOH 3% in water (10 mL). The reaction mixture was stirred for 8 hours and NPs migrated from the organic layer to the aqueous phase. The resulted water dispersed NPs were added to a BSA solution in water (10 mg in 15 mL water) and the reaction was stirred overnight to obtain BSA coated NPs. It is noteworthy that the stirring should be done in a medium speed and in room temperature to prevent

protein denaturing, usually observed as bubble formation. NP-BSA were washed using ultrafiltration (molecular weight cutoff MWCO: 100,000) to remove unbound BSA.

The cationization of NP-BSA was performed by treating the NPs (10 mg) with 2,2′-(ethylenedioxy)bis(ethylamine) in the presence of EDCI (100 mg) to yield positively charged NP-BSAx. The extent of cationization was greatly dependent on the pH of the reaction where pH = 6 was found to be optimal. Conjugation of sialic acid was achieved by EDCI (0.375 mmol) coupling of sialic acid **2** (0.125 mmol) to NP-BSAx (50 mg) dispersed in 15 mL pH=8.5 carbonate buffer and the reaction was stirred for 12 hours at room temperature. To hydrolyze methyl ester in the sialic acid conjugated, the NPs were treated with sodium hydroxide (0.01 M) and pH was carefully brought to 9. After 20 minute stirring, the pH value was dropped to 7.5 by adding hydrochloric acid solution (0.01 M). Finally, NP-BSAx-Sia were washed by ultrafiltration (MWCO 100,000) and dispersed in PBS buffer. For transcytosis and confocal microscopy experiments, NP-BSAx-Sia were labeled with the fluorophore FITC to yield NP-BSAx-Sia-FITC.

1.8.3. Characterization and Physicochemical Properties of NP-BSAx-Sia

The prepared NPs were imaged under transmission electron microscope (TEM) (JEM-2200FM) operating at 200 kV using Gatan multiscan CCD camera with Digital Micrograph imaging software. Following each step of NP synthesis, the size and charge of the NPs were measured by dynamic light scattering (DLS) using a Zetasizer Nano zs apparatus (Malvern, U.K.). Thermal Gravimetric Analysis (TGA) was performed to quantify the total amount of organic content of NPs.

To test the colloidal stability of the NPs, a solution of NP-BSAx-Sia in PBS was kept at 4 °C and the hydrodynamic sizes and surface charge of NPs were continuously monitored by DLS over

three weeks. As shown in **Figure 1-3c**, there were little changes of either hydrodynamic sizes or surface charges suggesting the high colloidal stability of the NPs.

To determine the magnetic relaxivitiy of the NP, serial dilutions of the NP were prepared, and T_2* weighted MRI was performed. ($1/T_2$*) value was plotted against Fe concentration, and r_2* was the slope of the best linear fit.

The number of sialic acid for each NP-BSAx-Sia was calculated as follows: based on TGA, 26% of NP-BSAx-Sia weight was Fe_3O_4 and TEM showed these nanoparticles are spherical and they are on average 5 nm in diameter. Since the lattice volume for magnetite is 592 Å3, on average, each NP-BSAx-Sia core contains 110.5 lattices based on the volume. From the crystal structure, each lattice contains 8 Fe_3O_4 molecules. Thus, the average number of Fe_3O_4 molecules in each NP-BSAx-Sia core is 884. Sialic acid accounted for 7% of NP-BSAx-Sia weight then the average number of sialic acid (MW:465 for sialic acid-linker) for each NP-BSAx-Sia is calculated to be 118.

1.8.4. Procedure for Quantifying the Amount of 2,2'-(ethylenedioxy)bis(ethylamine) on Cationized BSA

2,2'-(Ethylenedioxy)bis(ethylamine) (50.8 mg, 0.34 mmol) was dissolved in PBS (5 mL) and pH value of the solution was adjusted to 6 by dropwise addition of diluted HCl. BSA (10 mg) was dissolved in PBS (10 mL) and added to the diamine solution together with EDCI (131.3 mg, 0.68 mmol). The reaction was allowed to continue overnight. The resulting cationized BSA was purified using extensive steps of dialysis (MWCO 3.5 kDa) in water and PBS. MALDI MS analysis **Figure 1-2a** was used to determine molecular weight of BSA after cationization. The MS difference before and after diamine functionalization indicated that on average 33 molecules of 2,2'-(ethylenedioxy)bis(ethylamine) have been attached to each molecule of BSA.

1.8.5. Cytotoxicity Assay of NP-BSAx-Sia

bEnd.3 cells were plated into 96-well plates at a density of 4 $x10^4$ cells per well in 10% DMEM cell culture media for 24 hours at 37 °C and 5% CO_2. The culture medium was replaced with non-serum solution of different concentrations of NPs (0.0625, 0.125, 0.25, 0.5, 1 mg mL^{-1}/well). After 4 hours incubation at 37 °C, the medium was replaced with MTS solution (20 μL in 200 μL) in culture medium and incubated for 1 hour at 37 °C. The developed brown color in the wells was an indication of live cells. The absorption of the plate was measured at 490 nm in an iMark microplate reader (BioRad). Wells without cells (blanks) were subtracted as background from each sample.

1.8.6. Histological studies

Following soaking in sucrose solution, mouse brains were covered with optimum cutting temperature (OCT) formulation and frozen on a dry ice-methanol bath. Brains were sectioned at 10 μm using cryostat and tissues were placed on glass slides for further staining. To localize iron oxide NPs, Prussian blue staining was used, and tissues were examined under bright field microscope. Thio-S staining was applied on prepared brain tissue samples to locate Aβ plaques and samples were viewed under a confocal microscope (Nikon, A1 CLSM).

1.8.7. Animal

39 to 42 weeks old B6C3-Tg (APPswe/PS1dE9) mice and age matched wild type C57BL/6 mice were used for this study. Animal were purchased from Jackson Laboratories and were kept in the University Laboratory Animal Resources Facility of Michigan State University. All the experimental procedures for animal study were performed with approval of Institutional Animal Care and Use Committee (IACUC) of Michigan State University.

1.8.8. In Vivo Imaging

NP-BSAx-Sia was dispersed in PBS (100 µL) and administered to mice via retro-orbital injection at a dose of 0.14 mmol Fe/kg body weight. Isoflurane (2.5% in oxygen) was used for anesthesia induction for about 5 minutes and isoflurane (1-1.5% in oxygen) was used to maintain the anesthesia. A circulatory water bath was used to keep the mouse body temperature consistent around 35 °C. The breathing rate was monitored during scans and it was controlled around 20 per minutes to minimize motion artifacts. MRI scans were performed on a Bruker 7 T BioSpec 70/30 USR MRI. Images were acquired with a dedicated mouse brain coil (4 channel array) at 100 µm isotropic resolution using a 3D_FLASH sequence, flip angle = 15°, echo time = 8 ms, time of repetition = 30 ms, receiver bandwidth = ± 16 kHz, field of view = 19.2x19.2x16 mm, number of averages = 2, and number of excitation = 2.

40 week old female Tg mice were scanned before injection and at different time intervals (0.5, 1, 1.5, 2, 24 and 72 hours) post injections. Images collected were analyzed using NIH ImageJ software. The signal intensities of spots undergoing changes following NP injection were measured and they were normalized by dividing the measured intensity by the average intensity of brain tissues with no dark spots and these normalized values were plotted against time. As a control for Tg mice model of AD, NP-BSAx-Sia was injected at the same iron concentration to wild type mice and images were collected and analyzed as described above. To further examine the ability of NP-BSAx-Sia for binding to amyloid plaques, commercially available dextran coated iron oxide NPs (Feridex®) was injected to Tg mice and the images were analyzed in a similar manner.

REFERENCES

REFERENCES

(1) Prince, M.; Comas-Herrera, A.; Knapp, M.; Guerchet, M.; Karagiannidou, M. *World Alzheimer Report 2016*; https://www.alz.co.uk/research/WorldAlzheimerReport2016.pdf: September 2016, 2016.

(2) *2016 Alzheimer's Disease facts and figures*; https://www.alz.org/documents_custom/2016-facts-and-figures.pdf: 2016.

(3) Blennow, K.; Zetterberg, H. The past and the future of Alzheimer's disease CSF biomarkers-a journey toward validated biochemical tests covering the whole spectrum of molecular events. *Frontiers in neuroscience* **2015,** *9*, 345.

(4) Mueller, S. G.; Weiner, M. W.; Thal, L. J.; Petersen, R. C.; Jack, C. R.; Jagust, W.; Trojanowski, J. Q.; Toga, A. W.; Beckett, L. Ways toward an early diagnosis in Alzheimer's disease: the Alzheimer's Disease Neuroimaging Initiative (ADNI). *Alzheimers Dement.* **2005,** *1*, 55-66.

(5) Graham, W. V.; Bonito-Oliva, A.; Sakmar, T. P. Update on Alzheimer's Disease Therapy and Prevention Strategies. *Annu. Rev. Med.* **2017,** *68*, 413-430.

(6) Hardy, J.; Selkoe, D. J. Medicine - The amyloid hypothesis of Alzheimer's disease: Progress and problems on the road to therapeutics. *Science* **2002,** *297* (5580), 353-356.

(7) Chetelat, G.; Villemagne, V. L.; Bourgeat, P.; Pike, K. E.; Jones, G.; Ames, D.; Ellis, K. A.; Szoeke, C.; Martins, R. N.; O'Keefe, G. J.; Salvado, O.; Masters, C. L.; Rowe, C. C. Relationship between atrophy and beta-amyloid deposition in Alzheimer disease. *Annals of neurology* **2010,** *67* (3), 317-324.

(8) Johnson, K. A.; Minoshima, S.; Bohnen, N. I.; Donohoe, K. J.; Foster, N. L.; Herscovitch, P.; Karlawish, J. H.; Rowe, C. C.; Carrillo, M. C.; Hartley, D. M.; Hedrick, S.; Pappas, V.; Thies, W. H. Appropriate use criteria for amyloid PET: A report of the Amyloid Imaging Task Force, the Society of Nuclear Medicine and Molecular Imaging, and the Alzheimer's Association. *Alzheimers Dement.* **2013,** *9*, E1-E16.

(9) Klunk, W. E.; Engler, H.; Nordberg, A.; Wang, Y. M.; Blomqvist, G.; Holt, D. P.; Bergstrom, M.; Savitcheva, I.; Huang, G. F.; Estrada, S.; Ausen, B.; Debnath, M. L.; Barletta, J.; Price, J. C.; Sandell, J.; Lopresti, B. J.; Wall, A.; Koivisto, P.; Antoni, G.; Mathis, C. A.;

Langstrom, B. Imaging brain amyloid in Alzheimer's disease with Pittsburgh compound-B. *Annals of neurology* **2004,** *55* (3), 306-319.

(10) Klunk, W. E.; Lopresti, B. J.; Ikonomovic, M. D.; Lefterov, I. M.; Koldamova, R. P.; Abrahamson, E. E.; Debnath, M. L.; Holt, D. P.; Huang, G. F.; Shao, L.; DeKosky, S. T.; Price, J. C.; Mathis, C. A. Binding of the positron emission tomography tracer Pittsburgh compound-B reflects the amount of amyloid-beta in Alzheimer's disease brain but not in transgenic mouse brain. *The Journal of neuroscience : the official journal of the Society for Neuroscience* **2005,** *25* (46), 10598-10606.

(11) Vanhoutte, G.; Dewachter, I.; Borghgraef, P.; Van Leuven, F.; Van der Linden, A. Noninvasive in vivo MRI detection of neuritic plaques associated with iron in APP[V717I] transgenic mice, a model for Alzheimer's disease. *Magn. Reson. Med.* **2005,** *53*, 607-613.

(12) Jack, C. R.; Wengenack, T. M.; Reyes, D. A.; Garwood, M.; Curran, G. L.; Borowski, B. J.; Lin, J.; Preboske, G. M.; Holasek, S. S.; Adriany, G.; Poduslo, J. F. *In vivo* magnetic resonance microimaging of individual amyloid plaques in Alzheimer's transgenic mice. *The Journal of neuroscience : the official journal of the Society for Neuroscience* **2005,** *25*, 10041-10048.

(13) Braakman, N.; Matysik, J.; van Duinen, S. G.; Verbeek, F.; Schliebs, R.; de Groot, H. J. M.; Alia, A. Longitudinal assessment of Alzheimer's beta-amyloid plaque development in transgenic mice monitored by *in vivo* magnetic resonance microimaging. *J. Magn. Reson. Imaging* **2006,** *24*, 530-536.

(14) Jack, C. R.; Garwood, M.; Wengenack, T. M.; Borowski, B.; Curran, G. L.; Lin, J.; Adriany, G.; Gröhn, O. H.; Grimm, R.; Poduslo, J. F. *In vivo* visualization of Alzheimer's amyloid plaques by magnetic resonance imaging in transgenic mice without a contrast agent. *Magn. Reson. Med.* **2004,** *52*, 1263-1271.

(15) Wadghiri, Y. Z.; Li, J.; Wang, J.; Hoang, D. M.; Sun, Y.; Xu, H.; Tsui, W.; Li, Y.; Boutajangout, A.; Wang, A.; de Leon, M.; Wisniewski, T. Detection of amyloid plaques targeted by bifunctional USPIO in Alzheimer's disease transgenic mice using magnetic resonance microimaging. *Plos One* **2013,** *8*, e57097 and references cited therein.

(16) Tanifum, E. A.; Ghaghada, K.; Vollert, C.; Head, E.; Eriksen, J. L.; Annapragada, A. A Novel Liposomal Nanoparticle for the Imaging of Amyloid Plaque by Magnetic Resonance Imaging. *J. Alzheimers Dis.* **2016,** *52* (2), 731-745.

(17) Viola, K. L.; Sbarboro, J.; Sureka, R.; De, M.; Bicca, M. A.; Wang, J.; Vasavada, S.; Satpathy, S.; Wu, S.; Joshi, H.; Velasco, P. T.; MacRenaris, K.; Waters, E. A.; Lu, C.; Phan, J.;

Lacor, P.; Prasad, P.; Dravid, V. P.; Klein, W. L. Towards non-invasive diagnostic imaging of early-stage Alzheimer's disease. *Nat. Nanotechnol.* **2015,** *10*, 91-98.

(18) Wadghiri, Y. Z.; Hoang, D. M.; Wisniewski, T.; Sigurdsson, E. M., In Vivo magnetic resonance imaging of amyloid-beta plaques in mice. In *Amyloid Proteins: Methods and Protocols, Second Edition*, Sigurdsson, E. M.; Calero, M.; Gasset, M., Eds. Springer: New York, USA, 2012; Vol. 849, pp 435-451.

(19) Poduslo, J. F.; Wengenack, T. M.; Curran, G. L.; Wisniewski, T.; Sigurdsson, E. M.; Macura, S. I.; Borowski, B. J.; Jack, C. R. Molecular targeting of Alzheimer's amyloid plaques for contrast-enhanced magnetic resonance imaging. *Neurobiol. Dis.* **2002,** *11* (2), 315-329.

(20) Petiet, A.; Santin, M.; Bertrand, A.; Wiggins, C. J.; Petit, F.; Houitte, D.; Hantraye, P.; Benavides, J.; Debeir, T.; Rooney, T.; Dhenain, M. Gadolinium-staining reveals amyloid plaques in the brain of Alzheimer's transgenic mice. *Neurobiol. Aging* **2012,** *33*, 1533-1544.

(21) Pardridge, W. M. The blood-brain barrier: bottleneck in brain drug development. *NeuroRx* **2005,** *2*, 3-14.

(22) Brightman, M. W. Morphology of blood-brain interfaces. *Exp. Eye Res.* **1977,** *25*, 1-25.

(23) Aparicio-Blanco, J.; Martin-Sabroso, C.; Torres-Suárez, A. I. In vitro screening of nanomedicines through the blood brain barrier: A critical review. *Biomaterials* **2016,** *103*, 229-255.

(24) Rapoport, S. I. Osmotic Opening of the Blood–Brain Barrier: Principles, Mechanism, and Therapeutic Applications. *Cell. Mol. Neurobiol.* **2000,** *20*, 217-230.

(25) Yang, J.; Wadghiri, Y. Z.; Hoang, D. M.; Tsui, W.; Sun, Y.; Chung, E.; Li, Y.; Wang, A.; de Leon, M.; Wisniewski, T. Detection of Amyloid Plaques Targeted by USPIO-Aβ1-42 in Alzheimer's Disease Transgenic Mice using Magnetic Resonance Microimaging. *NeuroImage* **2011,** *55* (4), 1600-1609.

(26) Wadghiri, Y. Z.; Sigurdsson, E. M.; Sadowski, M.; Elliott, J. I.; Li, Y.; Scholtzova, H.; Tang, C. Y.; Aguinaldo, G.; Pappolla, M.; Duff, K.; Wisniewski, T.; Turnbull, D. H. Detection of Alzheimer's amyloid in transgenic mice using magnetic resonance microimaging. *Magn. Reson. Med.* **2003,** *50* (2), 293-302.

(27) Sillerud, L. O.; Solberg, N. O.; Chamberlain, R.; Orlando, R. A.; Heidrich, J. E.; Brown, D. C.; Brady, C. I.; Vander Jagt, T. A.; Garwood, M.; Vander Jagt, D. L. SPION-Enhanced Magnetic Resonance Imaging of Alzheimer's Disease Plaques in AβPP/PS-1 Transgenic Mouse Brain. *J. Alzheimer's Dis.* **2013,** *34* (2), 349-365.

(28) Salloway, S.; Sperling, R.; Fox, N. C.; Blennow, K.; Klunk, W.; Raskind, M.; Sabbagh, M.; Honig, L. S.; Porsteinsson, A. P.; Ferris, S.; Reichert, M.; Ketter, N.; Nejadnik, B.; Guenzler, V.; Miloslavsky, M.; Wang, D.; Lu, Y.; Lull, J.; Tudor, I. C.; Liu, E.; Grundman, M.; Yuen, E.; Black, R.; Brashear, H. R. Two phase 3 trials of bapineuzumab in mild-to-moderate Alzheimer's disease. *The New England journal of medicine* **2014,** *370* (4), 322-333.

(29) Ostrowitzki, S.; Deptula, D.; Thurfjell, L.; Barkhof, F.; Bohrmann, B.; Brooks, D. J.; Klunk, W. E.; Ashford, E.; Yoo, K.; Xu, Z. X.; Loetscher, H.; Santarelli, L. Mechanism of amyloid removal in patients with Alzheimer disease treated with gantenerumab. *Archives of neurology* **2012,** *69* (2), 198-207.

(30) Sperling, R.; Salloway, S.; Brooks, D. J.; Tampieri, D.; Barakos, J.; Fox, N. C.; Raskind, M.; Sabbagh, M.; Honig, L. S.; Porsteinsson, A. P.; Lieberburg, I.; Arrighi, H. M.; Morris, K. A.; Lu, Y.; Liu, E.; Gregg, K. M.; Brashear, H. R.; Kinney, G. G.; Black, R.; Grundman, M. Amyloid-related imaging abnormalities in patients with Alzheimer's disease treated with bapineuzumab: a retrospective analysis. *The Lancet. Neurology* **2012,** *11* (3), 241-249.

(31) Cheng, K. K.; Chan, P. S.; Fan, S.; Kwan, S. M.; Yeung, K. L.; Wang, Y. X.; Chow, A. H.; Wu, E. X.; Baum, L. Curcumin-conjugated magnetic nanoparticles for detecting amyloid plaques in Alzheimer's disease mice using magnetic resonance imaging (MRI). *Biomaterials* **2015,** *44*, 155-172.

(32) Hu, B.; Dai, F.; Fan, Z.; Ma, G.; Tang, Q.; Zhang, X. Nanotheranostics: Congo Red/Rutin-MNPs with Enhanced Magnetic Resonance Imaging and H2O2-Responsive Therapy of Alzheimer's Disease in APPswe/PS1dE9 Transgenic Mice. *Advanced materials (Deerfield Beach, Fla.)* **2015,** *27* (37), 5499-5505.

(33) Kouyoumdjian, H.; Huang, X., Sialic acid-modified nanoparticles for β-amyloid studies. In *Carbohydrate Nanotechnology*, Stine, K. J., Ed. John Wiley & Sons, Inc.: Hoboken, New Jersey, USA, 2016; pp 309-333.

(34) Wang, B. Sialic acid is an essential nutrient for brain development and cognition. *Annual review of nutrition* **2009,** *29*, 177-222.

(35) Williamson, M. P.; Suzuki, Y.; Bourne, N. T.; Asakura, T. Binding of amyloid beta-peptide to ganglioside micelles is dependent on histidine-13. *Biochem. J.* **2006,** *397*, 483-490.

(36) Zha, Q.; Ruan, Y.; Hartmann, T.; Beyreuther, K.; Zhang, D. GM1 ganglioside regulates the proteolysis of amyloid precursor protein. *Mol. Psychiatry* **2004,** *9* (10), 946-952.

(37) Matsuzaki, K.; Horikiri, C. Interactions of amyloid beta-peptide (1-40) with ganglioside-containing membranes. *Biochemistry* **1999,** *38* (13), 4137-4142.

(38) Ariga, T.; Kobayashi, K.; Hasegawa, A.; Kiso, M.; Ishida, H.; Miyatake, T., Characterization of high-affinity binding between gangliosides and amyloid beta-protein. In *Arch. Biochem. Biophys.*, 2001; Vol. 388, pp 225-230.

(39) Ariga, T.; Yu, R. K. GM1 inhibits amyloid beta-protein-induced cytokine release. *Neurochem. Res.* **1999,** *24* (2), 219-226.

(40) Patel, D. A.; Henry, J. E.; Good, T. A. Attenuation of beta-amyloid-induced toxicity by sialic-acid-conjugated dendrimers: Role of sialic acid attachment. *Brain Res.* **2007,** *1161*, 95-105.

(41) Patel, D.; Henry, J.; Good, T. Attenuation of beta-amyloid induced toxicity by sialic acid-conjugated dendrimeric polymers. *Biochimica et biophysica acta* **2006,** *1760* (12), 1802-1809.

(42) Chikae, M.; Fukuda, T.; Kerman, K.; Idegami, K.; Miura, Y.; Tamiya, E. Amyloid-beta detection with saccharide immobilized gold nanoparticle on carbon electrode. *Bioelectrochemistry* **2008,** *74* (1), 118-123.

(43) Dhavale, D.; Henry, J. E. Evaluation of sialic acid-analogs for the attenuation of amyloid-beta toxicity. *Biochimica et biophysica acta* **2012,** *1820* (10), 1475-1480.

(44) Kouyoumdjian, H.; Zhu, D. C.; El-Dakdouki, M. H.; Lorenz, K.; Chen, J.; Li, W.; Huang, X. Glyconanoparticle aided detection of beta-amyloid by magnetic resonance imaging and attenuation of beta-amyloid induced cytotoxicity. *ACS chemical neuroscience* **2013,** *4* (4), 575-584.

(45) Krol, S. Challenges in drug delivery to the brain: nature is against us. *J. Control. Release* **2012,** *164* (2), 145-155.

(46) Xie, J.; Peng, S.; Brower, N.; Pourmand, N.; Wang, S. X.; Sun, S. One-pot synthesis of monodisperse iron oxide nanoparticles for potential biomedical applications. *Pure Appl. Chem.* **2006,** *78*, 1003-1014.

(47) Yim, Y. S.; Choi, J. S.; Kim, G. T.; Kim, C. H.; Shin, T. H.; Kim, D. G.; Cheon, J. A facile approach for the delivery of inorganic nanoparticles into the brain by passing through the blood-brain barrier (BBB). *Chemical communications (Cambridge, England)* **2012,** *48* (1), 61-63.

(48) Smith, K. R.; Borchardt, R. T. Permeability and mechanism of albumin, cationized albumin, and glycosylated albumin transcellular transport across monolayers of cultured bovine brain capillary endothelial cells. *Pharm. Res.* **1989,** *6*, 466-473.

(49) Warren, L. The Thiobarbituric Acid Assay of Sialic Acids. *J. Biol. Chem.* **1959,** *234* (8), 1971-1975.

(50) Li, G.; Simon, M. J.; Cancel, L. M.; Shi, Z. D.; Ji, X.; Tarbell, J. M.; Morrison III, B.; Fu, B. M. Permeability of endothelial and astrocyte cocultures: in vitro blood-brain barrier models for drug delivery studies. *Ann. Biomed. Eng.* **2010,** *38*, 2499-2511.

(51) Reiserer, R. S.; Harrison, F. E.; Syverud, D. C.; McDonald, M. P. Impaired spatial learning in the APPSwe + PSEN1DeltaE9 bigenic mouse model of Alzheimer's disease. *Genes Brain Behav.* **2007,** *6*, 54-65 and references cited therein.

(52) Chin, J. Selecting a mouse model of Alzheimer's disease. *Methods Mol. Biol.* **2011,** *670*, 169-189.

(53) O'Bryant, S. E.; Gupta, V.; Henriksen, K.; Edwards, M.; Jeromin, A.; Lista, S.; Bazenet, C.; Soares, H.; Lovestone, S.; Hampel, H.; Montine, T.; Blennow, K.; Foroud, T.; Carrillo, M.; Graff-Radford, N.; Laske, C.; Breteler, M.; Shaw, L.; Trojanowski, J. Q.; Schupf, N.; Rissman, R. A.; Fagan, A. M.; Oberoi, P.; Umek, R.; Weiner, M. W.; Grammas, P.; Posner, H.; Martins, R. Guidelines for the standardization of preanalytic variables for blood-based biomarker studies in Alzheimer's disease research. *Alzheimers Dement.* **2015,** *11* (5), 549-560.

(54) Irizarry, M. C. Biomarkers of Alzheimer disease in plasma. *NeuroRx* **2004,** *1* (2), 226-234.

(55) Blennow, K.; Hampel, H.; Weiner, M.; Zetterberg, H. Cerebrospinal fluid and plasma biomarkers in Alzheimer disease. *Nature reviews. Neurology* **2010,** *6* (3), 131-144.

(56) Zhou, J.; Fa, H.; Yin, W.; Zhang, J.; Hou, C.; Huo, D.; Zhang, D.; Zhang, H. Synthesis of superparamagnetic iron oxide nanoparticles coated with a DDNP-carboxyl derivative for in vitro magnetic resonance imaging of Alzheimer's disease. *Mater. Sci. Eng. C Mater. Biol. Appl.* **2014,** *37*, 348-355.

(57) Yang, C. C.; Yang, S. Y.; Chieh, J. J.; Horng, H. E.; Hong, C. Y.; Yang, H. C.; Chen, K. H.; Shih, B. Y.; Chen, T. F.; Chiu, M. J. Biofunctionalized magnetic nanoparticles for specifically detecting biomarkers of Alzheimer's disease in vitro. *ACS chemical neuroscience* **2011,** *2* (9), 500-505.

(58) Nance, E. A.; Woodworth, G. F.; Sailor, K. A.; Shih, T. Y.; Xu, Q.; Swaminathan, G.; Xiang, D.; Eberhart, C.; Hanes, J. A Dense Poly(Ethylene Glycol) Coating Improves Penetration of Large Polymeric Nanoparticles Within Brain Tissue. *Sci. Transl. Med.* **2012,** *4* (149), 149ra119.

(59) Jones, A. R.; Shusta, E. V. Blood-brain barrier transport of therapeutics via receptor-mediation. *Pharm. Res.* **2007,** *24* (9), 1759-1771.

(60) Fröhlich, E. The role of surface charge in cellular uptake and cytotoxicity of medical nanoparticles. *Int. J. Nanomed.* **2012,** *7*, 5577-5591.

(61) He, X.-P.; Zang, Y.; James, T. D.; Li, J.; Chen, G.-R.; Xie, J. Fluorescent glycoprobes: a sweet addition for improved sensing. *Chemical communications (Cambridge, England)* **2017,** *53*, 82-90.

Chapter 2: An Introduction to Nanomedicine for Imaging and Therapy of Inflammatory Atherosclerotic Plaques

2.1. Introduction:

Atherosclerosis is the thickening of artery vessel walls that can develop in arteries supplying blood to various end-organs such as heart, brain, kidneys, etc. It is a major cause of heart attack and stroke [1], with the majority of patients who experience cardiac arrests have atherosclerosis [2]. It has been estimated that by 2030, the global cost of cardiovascular diseases (CVD) would reach $ 1044 billion [3].

To better understand atherosclerosis pathology, it is important to know structures of arteries. Collectively, walls of arteries consist of three different parts including tunica intima, tunica media and tunica externa. Simple squamous endothelial cells line the tunica intima and internal elastic lamina separates it from the tunica media. The media is formed from elastic lamellae and elastic fibers alternating with layers of smooth muscle cells. Proteoglycans and reticular fibers are the other components of the media. Finally, connective tissues make the tunica externa consisting of collagen and elastic fibers **Figure 2-1** [4].

Atherosclerosis is known as a chronic inflammatory condition [1]. One important trigger for the formation of atherosclerotic plaques is hypercholesterolemia. Cholesterol is transported in the plasma through lipoproteins. Among them, apolipoprotein B is responsible for carrying cholesterol and fat molecule around the body and when are generally packed in particles known as low density lipoprotein (LDL). Increasing the cholesterol level of plasma results in accumulation of lipids into the arterial wall. This accrual is mediated mostly through LDL particles together with changes in endothelial cell permeabilities. Overexpression of receptors such as vascular adhesion molecule 1 (VCAM-1) and selectins enhance their interactions with LDL and mediate LDL entrance into the arterial wall [5]. In addition, oxidized LDL (oxLDL) favors the intracellular accumulation of

cholesterol esters [6]. Moreover, oxLDL is a potent inducer of inflammatory molecules and mediates monocyte binding to endothelial cells [7].

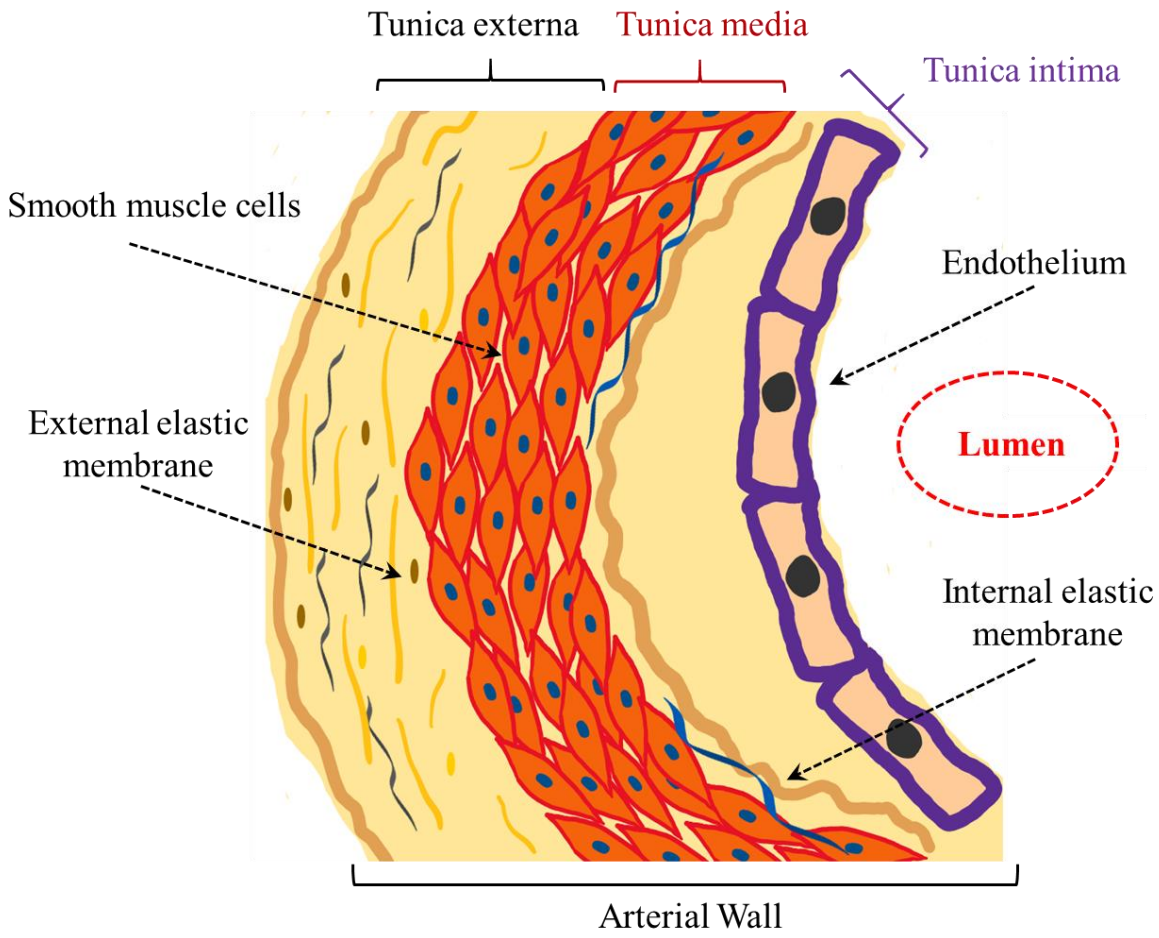

Figure 2-1. Schematic demonstration of the arterial wall.

2.2. Current Atherosclerotic Treatment Methods

Management of atherosclerotic plaques typically involves drugs and/or surgery. Surgical intervention includes procedures such as angioplasty and bypass grafting. In angioplasty, a blocked or narrowed artery can be opened and sometimes a physical device called stent is placed there to keep it open [8] while in bypass grafting a healthy blood vessel is used to bypass the area of atherosclerosis plaque [9].

For therapeutic molecules, statins are the most important class. Statins inhibit 3-hydroxy-3-methylglutaryl coenzyme A (HMG-CoA) reductase, which is a key enzyme for cholesterol biosynthesis [10]. Since high blood cholesterol is an important risk factor for cardiovascular diseases, statins can reduce possible CVD events through reduction of cholesterol levels [11].

In addition to their cholesterol modulating activities, statins can exert cardiovascular protecting effects through other pathways [12]. These pleiotropic effects are mostly the result of isoprenylation inhibition that reduces the function of isoprenoids such as Rho and Rac proteins. These proteins are involved in the expression of proinflammatory cytokines and transduction of signaling molecules. For instance, they can modulate reactive oxygen species (ROS) generation and their reduction can result in anti-inflammatory outcomes [13]. An important study that addressed anti-inflammatory effect of statins independent of their effect on LDL cholesterol level was conducted by Paul M Ridker in Harvard University. In this study, Pravastatin was shown to reduce C-reactive protein (CRP) levels in people when assessed 12 and 24 weeks after taking the drug [14]. CRP is known as a sensitive systemic marker for inflammation [15] and any acute inflammatory stimulus may cause a rapid rise of CRP level up to 1000-fold [16]. Besides CRP, statins can reduce expression of cyclooxygenase-2 (Cox-2) in human endothelial cells [17], murine macrophages (RAW264.7) [18] and atherosclerosis lesions in rabbits [19]. Cox-2 is an inducible pro-inflammatory enzyme, which is mainly present [20] in inflammatory macrophages in atherosclerotic plaques [21]. Pro-inflammatory macrophages or M1 are known as activated macrophages that propagate proinflammatory cytokines such as TNFα, IL-1 and IL-6[22]. Statins also can alleviate proinflammatory cytokines effects. For instance, reduction of TNFα, IL-1 and IL-6 have been observed in hypercholesterolemic patients that received atorvastatin for 2 months [23]. High dose statin therapy can lead to rapid reduction of atherosclerosis inflammation [24-25] indicating the potential of this

medicine for management of inflammatory atherosclerotic plaques. While statins have shown their beneficial effects, the therapeutic regimen should be carefully designed to prevent undesired outcomes. For example, discontinuation of statins results in rebound inflammation and increased short-term cardiovascular risks, even in the absence of changes in lipid levels [26-27].

Besides statins, there are other therapeutic molecules for management of atherosclerosis. Proprotein convertase subtilisin/kexin type 9 (PCSK9) is an enzyme involved LDL homeostasis. Agents that can block PCSK9 can enhance LDL degradation and lower cholesterol levels. Two PCSK9 inhibitors, alirocumab and evolocumab, were approved by the U.S. Food and Drug Administration to use in patients who are not tolerant of statins. In addition, anti-inflammatory agents are entering the clinic for atherosclerosis complications. For instance, canakinumab which targets human interleukin-1β has shown promising results when evaluated in patients with CVD complications and high levels of C-reactive protein [28]. In addition, immunosuppressants such as methotrexate and rapamycin have shown promising effects to reduce atherosclerotic plaque size when studied in ApoE knockout mice [29-30].

While anti-inflammatory approach seems the most popular drug therapy regimen for atherosclerosis complications, the choice of suitable anti-inflammatory molecule requires special consideration. Prednisolone, a corticosteroid drug, showed high accumulation in plaque macrophages when formulated in liposomal nanoparticle (LN-PLP) [31]. However, further studies ruled out this medicine for atherosclerosis management. In vitro experiments showed lipotoxic effects of LN-PLP when incubated with macrophages [32]. In vivo analysis indicated the drug accelerated atherosclerosis through necrotic size growth. Recently, a new study in a murine model of atherosclerosis has demonstrated the beneficial effects of IL-1β in the late stage of

atherosclerosis. Therefore, special caution should be considered for using monoclonal Ab against IL-1β such as canakinumab in high risk patient [33].

2.3. Active Targeting of Atherosclerosis

As mentioned earlier, macrophages and monocytes play important roles in the formation and progression of atherosclerosis. Not surprisingly, these cells have been considered extensively for imaging and/or therapeutic purposes of atherosclerosis. Although phagocytic activities of macrophages together with their trafficking properties into the inflammatory sites make them a good candidate for targeting atherosclerosis plaques [34], active targeting of inflammatory macrophages can be beneficial. For example, while 500-1000 μmol Fe/kg body weight is needed for magnetic resonance imaging (MRI) of atherosclerosis plaques in ApoE knockout mouse through non-targeted iron oxide nanoparticles [35], the amounts of agents needed can be reduced to 36 μmol Fe/kg when iron oxide nanoprobes were decorated with anti-CD163 mAbs for active targeting of macrophages residing in inflammatory atherosclerotic plaques **Figure 2-2b** [36]. Moreover, hyaluronic acid (HA) conjugated iron oxide nanoparticle (HA-NP) has been developed for active targeting of macrophage CD44 receptor enabling *in vivo* imaging of atherosclerotic plaques in a rabbit model of atherosclerosis following injection of 3.75 μmol Fe/kg **Figure 2-2c,d** [37] while other studies used at least 10 times higher amount of Fe/kg for imaging atherosclerosis plaques in this animal model without building in a receptor recognition element [38-39].

Active targeting of atherosclerotic plaques has been studied through various strategies. For instance, activated macrophages and foam cells residing in inflammatory atherosclerosis plaques overexpress myeloperoxidase (MPO) [40]. Gd based MPO sensor was designed to detect inflammation in a rabbit model of atherosclerosis [41]. Another strategy for active targeting of macrophages is the coating of nanocarrier with oxidized phosphatidylcholine (PC) [42]. Interaction

of macrophages with oxidized PC (e.g., 1-(palmitoyl)-2-(5-keto-6-octene-dioyl)) through CD36 receptor has been explored [43-44], due to its high affinity for binding with CD36 receptor (IC50: 3.9 μM) **Figure 2-3c** [45]. Another example is a cytokine known as osteopontin (OPN) expressed by foamy macrophages to recruit leukocytes and induce matrix metalloproteinase (MM) expression[46-47]. Anti-OPN mAb has been used for imaging vulnerable atherosclerotic plaques with various engineered nanoprobes **Figure 2-2a** [48].

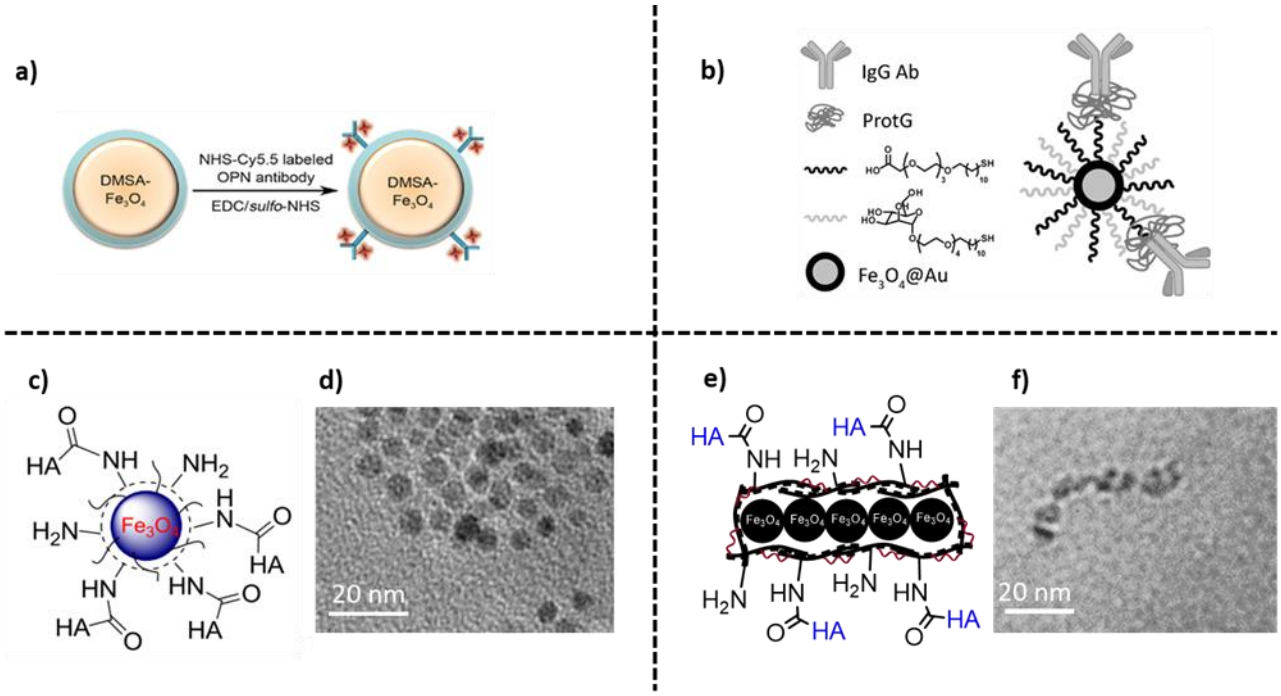

Figure 2-2. Iron oxide nanoparticles for active targeting of atherosclerotic plaques. (a,b) showing anti-body directed nanoparticles for atherosclerotic plaque imaging. (a) iron oxide nanoparticle has been conjugated with anti-osteopontin antibody labeled with Cy5.5 fluorescent dye for dual modality imaging of plaques. Copyright (2017) by Elsevier. (b) gold coated iron oxide nanoparticle first was covered with mannose and carboxylic acid ending ligand, then protG was immobilized on nanoparticle and finally it was decorated with anti CD-163 antibody. This nanoparticle can be used for MRI and CT imaging of plaques (Adopted from *Tarin. et. al.*) [36]. (c,d) are hyaluronan

Figure 2-2 (cont'd) conjugated iron oxide nanoparticles. These MRI probes are targeted towards CD44 receptor, can be prepared in different morphologies. Copyright (2013) by Springer Nature. (e) has worm like shape and induce lower inflammatory response comparing to the spherical morphology. Copyright (2018) American Chemical Society (c).

An additional molecule for targeting apoptotic macrophages in atherosclerotic plaque is annexin v [49]. Decoration of nanoprobes with annexin v protein can target phosphatidyl serine present on membrane of apoptotic macrophages in atherosclerotic plaques [50]. Interestingly, virus like particles have also been used for targeting macrophages. For instance, Simian virus 40 (SV40) has been loaded with imaging and therapeutic molecules and targeted to p32 protein on macrophage surface through insertion of CGNKRTRGC peptide known as LyP-1[51]. In addition, a therapeutic peptide, Hirulog, has been incorporated, which is a thrombin inhibitor and has anti-coagulant activities [52]. Elaborate protein engineering was applied to insert the targeting peptide pointing out to guide targeting with the Hirulog peptide pointing in after self-assembly of SV40 virus nanoparticles.

Angiogenesis targeting is another strategy for imaging atherosclerotic lesions. Since integrin molecules such as αvβ3 play critical roles in angiogenesis, they could be targeted by an integrin receptor antagonist [53]. In addition, endothelial cells over-express adhesion molecules such as vascular cell adhesion molecule-1 (VCAM-1), intracellular adhesion molecule-1 (ICAM-1) and selectins in atherosclerotic plaques [54]. Thus, various studies have targeted adhesion molecules to direct nanoprobes. For instance, VCAM-1 has been targeted by a short peptide (VHPKQHRAEEAK) [55] to image atherosclerotic plaques in ApoE knockout mice. Anti-ICAM-1 monoclonal antibody is another approach for targeting endothelial cell adhesion molecules and delivering their payload through cell adhesion molecule-mediated endocytosis into the plaque site

[56]. In other studies, microparticles containing atheroprotective microRNA (miR-146a/-181b) have been targeted to E-selectin through a thioaptamer molecule [57].

Collagen is an important target for atherosclerotic lesions specially since collagen IV forms the bases of blood vessels and it gets exposed during atherosclerosis progression [58]. Phage display has been used to discover short peptides enabling the targeting of collagen IV [59]. Theranostic nanoparticles have been engineered to deliver their payload into the atherosclerosis plaques through collagen IV binding peptide **Figure 2-3a** [60-61]. Another protein molecule for atherosclerosis targeting is profilin-1, which is an actin binding protein and its over-expression is associated with atherosclerosis and other cardiovascular complications [62]. Subsequently, nanoparticles have been conjugated with anti-profilin-1 molecule to deliver therapeutics such as profilin-1 siRNA into the plaque sites. Profilin-1 silencing exerts its therapeutic properties by reducing mouse aorta smooth muscle cell proliferation and migration [63].

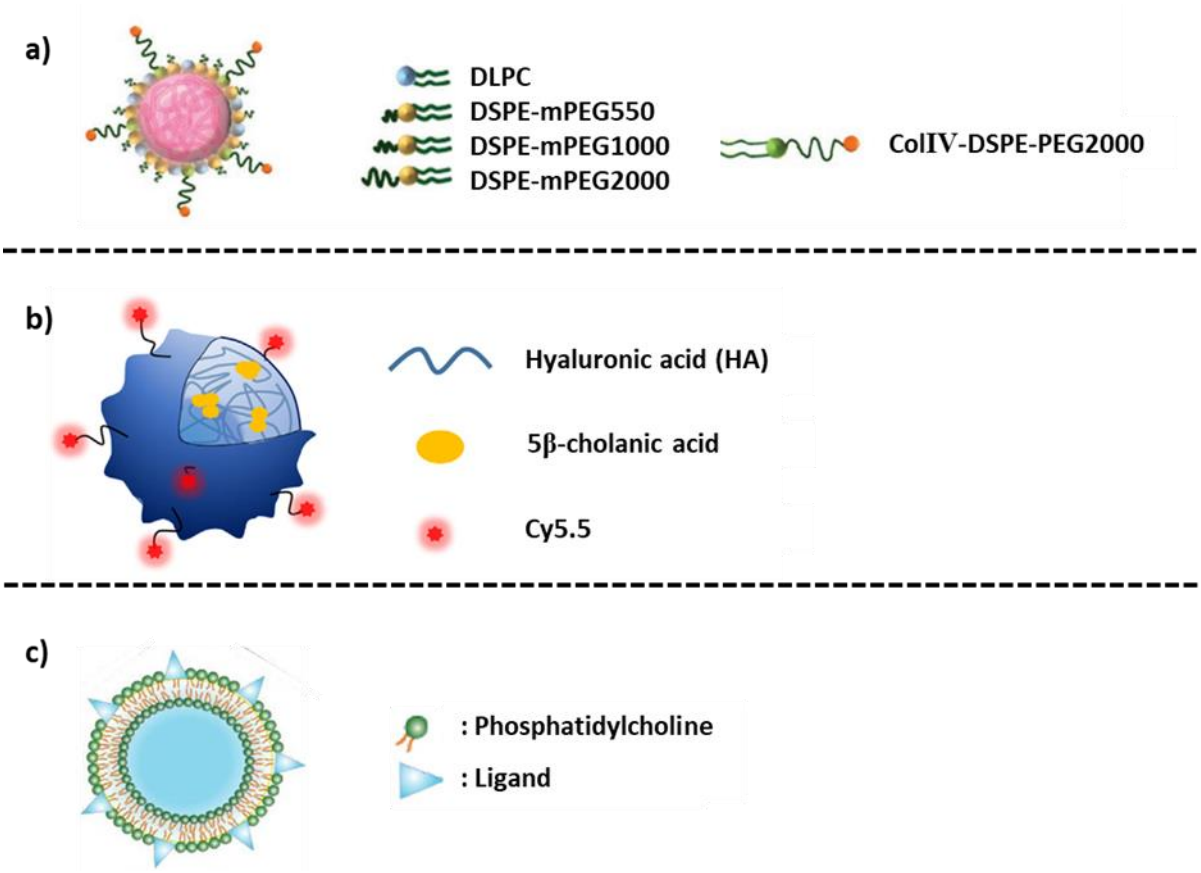

Figure 2-3. Polymeric nanoparticle and nanovesicle for targeting atherosclerotic plaques. (a) Lipid-polymer hybrid nanoparticle contains three components: a biodegradable hydrophobic polymeric core, a lipid layer and a peptide decoration for ColIV targeting. Copyright 2017 John Wiley & Sons. (b) Conjugation of hydrophobic 5-cholinic acid with hyaluronan resulted in self assembled nanoparticle formation. This formulation could be a drug carrier for atherosclerotic plaques imaging and/or therapy. Copyright (2015), with permission from Elsevier. (c) Liposome-like nanovesicle was prepared to target CD36 receptor through KOdiA-PC ligand. Copyright (2015), with permission from Elsevier.

2.3.1. HDL Like Nanoparticles for Statin Delivery

In human bodies, two endogenous nanoparticles known as high-density lipoprotein (HDL) and low-density lipoprotein (LDL), play important roles in managing cholesterol homeostasis. LDL are small carriers of fat molecules to the cells. They can penetrate to arterial walls, get oxidized and cause inflammation. However, HDL can interact with lipid-laden plaque macrophages, and mediate cholesterol removal from plaques by transporting them into the liver [64-65]. The diameter of HDL is about 8-12 nm and hydrophobic lipids are located in the core while phospholipids and apolipoproteins such as apolipoprotein A (ApoA)-1 or ApoA-II form the outer layer [66]. Therefore, scientists have investigated HDL and/or HDL mimetic nanoparticles to target atherosclerotic plaques. For instance, microfluidic technology has been used to build poly(lactic-co-glycolic acid) (PLGA)-HDL nanocarrier. This nanocarrier contains a PLGA core capable of loading hydrophobic drugs while it is decorated with ApoA-1 and phospholipids such as 1,2-distearoyl-sn-glycero-3-phosphocholine (DSPC) and 1-stearoyl-2-hydroxy-sn-glycero-3-phosphocholine (SHPC) **Figure 2-4c-e**. PLGA-HDL showed a slow drug release behavior with 60% release in 24 hours and up to 90% release after 5 days in PBS buffer. Moreover, animal study on Apo E knockout mice showed 12.8-hour half-life in blood circulation and their targeting property was confirmed by high accumulation of these particles in macrophages residing in atherosclerotic plaques [67]. Although using PLGA core in this system enables loading of different therapeutic and/or imaging molecules, it can impose limitations on ApoA-I conformational flexibility resulting in impaired cholesterol efflux [68-69]. Moreover, this artificial polymeric core induced changes in the shape of these nanoparticles to be more spherical rather than discoidal shape of native HDL, and their size increased significantly in comparison to the HDL, which are some of the limitations of the PLGA-HDL system.

In addition to nanoparticle size and shape, phospholipid core has been studied and 1-palmitoyl-2-oleoyl-sn-glycero-3-phosphocholine (POPC) based HDL nanoparticle showed the highest similarity to natural HDL [69]. Such HDL like nanoparticles have been used to deliver statins into inflammatory atherosclerotic plaques. For instance, reconstituted HDL (rHDL) nanoparticles loaded with simvastatin [S]-rHDL have been designed and successfully employed to deliver the payload into inflammatory plaques in ApoE knockout mice **Figure 2-4a,b** [70]. A comparison was made for low doses of [S]-rHDL(15 mg/kg simvastatin, 10 mg/kg ApoA-I) that was administered (i.v) biweekly for 12 weeks vs orally administered simvastatin (15 mg/kg per day) and the results showed lower plaque macrophage content for [S]-rHDL group. Interestingly, delivery of a high dose (60 mg/kg simvastatin, 40 mg/kg ApoA-I) by this nanoparticle to ApoE knockout mice in four intravenous (i.v) injections showed significant mitigation effects on plaque inflammation while rHDL alone could not decrease plaque area based on histological analysis. The stronger effect for short term high [S]-rHDL group indicates the importance of delivering higher amount of simvastatin for inhibiting atherosclerotic plaque inflammation.

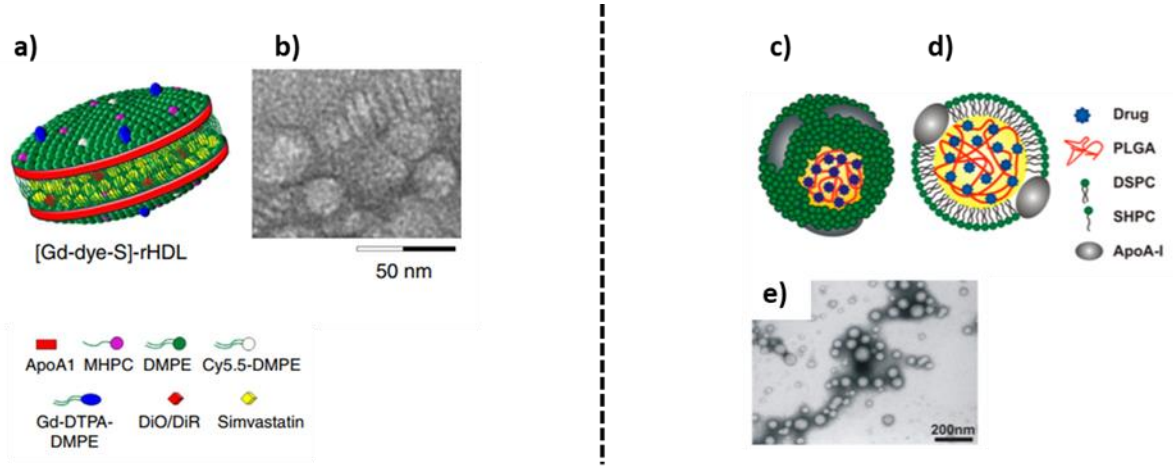

Figure 2-4. HDL like nanoparticle. (a) The schematic shows reconstituted HDL nanoparticle or rHDL, having discoidal morphology like native HDL and TEM image confirms it. Copyright

Figure 2-4 (cont'd) (2014) by Springer Nature (b). (c-e) PLGA-HDL nanoparticle has spherical morphology. As shown above in 2D image (d) PLGA forms the polymeric core of this nanoparticle and the size of these nanoparticles can be fine-tuned by adjusting PLGA/lipid ratio. Copyright (2015) American Chemical Society.

Although rHDL is an attractive drug delivery system for cardiovascular diseases, undesired drug leakage is a drawback of this system. One reason for this leakage is believed to be the interaction of drug loaded rHDL with lecithin cholesterol acyltransferase (LCAT) that impose remodeling behavior to this particle [71-72]. One approach to decrease r-HDL reactivity with LCAT is through the insertion of arachidonic acid (AA) into the phospholipid bilayers of rHDL [73]. Thus, adjustment of physicochemical properties of rHDL such as AA modification is another possibility that could enhance nanocarrier design for drug delivery to atherosclerotic plaques [74].

In order to improve drug delivery property of HDL like particles, dextran sulfate (DXS) has been used to coat rHDL surface as DXS can bind with scavenge receptor AI (SR-AI) highly expressed on activated macrophage and foam cells in inflammatory plaques through electrostatic interaction [75-76]. In this design, atorvastatin was loaded in a spherical PLGA core encapsulated in liposomes. Then, it was decorated by ApoA-I and finally coated with DXS (AT-DXS-LP-rHDL) [77]. Cellular study showed the ability of these particles to facilitate cholesterol efflux from macrophages (RAW264.7 and THP-1 cells). Moreover, these particles were able to reduce TNF-α and IL-6 production in macrophages due to atorvastatin release. It is noteworthy that ApoA-I and DXS coating both helped retard atorvastatin release. In addition, ox-LDL uptake by macrophages was significantly reduced because high affinity DXS competes with ox-LDL for SR-AI binding.

2.3.2. HA Based Nanoparticles Targeting CD44 for Atherosclerosis Treatment

Overexpressed CD44 in atherosclerotic plaques is an important target for drug delivery. Hyaluronic acid (HA) is a high affinity ligand for this receptor and has been used to decorate rHDL for targeting inflammatory atherosclerotic plaques [78]. Simvastatin loaded PLGA nanoparticle is encapsulated into liposomes and decorated with ApoA-I and HA (ST-HA-PLGA-rHDL). HA immobilization was carried out by two different strategies. The first strategy includes covalent conjugation of HA onto available amine groups of ApoA-I through 1-ethyl-3-(3-dimethylaminopropyl) carbodiimide (EDC) and N-hydroxy-succinimide (NHS) coupling agents (ST-HA-(C)-PLGA-rHDL). The second strategy was electrostatic absorption of HA by cationic ST-PLGA-rHDL (ST-HA-(E)-PLGA-rHDL). Testing these nanostructures *in vivo* on a rabbit model of atherosclerosis indicated better atheroprotective activity for ST-HA-(C)-PLGA-rHDL. This observation has been explained through better shielding effect of covalent HA coating that decreases their liver uptake [79]. In addition to the liver uptake reduction, HA coating enhanced nanoparticle accumulation in atherosclerotic plaques due to its interaction with CD44 receptors. This effect has been shown in the rabbit model of atherosclerosis through quantification of DiR labeled HA-(C)-PLGA-rHDL in the aortic tree.

HA has also being utilized to reduce rHDL uptake by liver's scavenger receptor class B type I (SR-BI). Lovastatin loaded r-HDL (LT-rHDL) has been decorated with HA which facilitated their interactions with up-regulated CD44 receptors in inflammatory plaques while reducing their liver uptake [80]. Decorating the Apo proteins with HA polymer helped LT-rHDL escape from the reticuloendothelial system (RES) and improved lovastatin circulation time *in vivo*.

In addition to HA-rHDL, another type of HA nanoparticle has been prepared by conjugation of hydrophobic 5β-cholanic acid to carboxylic acid of HA through NHS, EDC chemistry via a

diamine linker. The resulting conjugate can self-assemble to nanoparticles in water due to the hydrophilic nature of HA backbone and hydrophobic property of 5β-cholanic acid **Figure 2-3b**. Labeling this NP system with fluorescent molecules such as Cy5.5 and FITC demonstrated that this HA-NP could be selectively uptaken by CD44 expressing cells in vitro through receptor mediated endocytosis. Moreover, injection of this nanoparticle to ApoE knockout mice showed its accumulation in atherosclerotic plaques and further immunohistochemistry studies confirmed co-localization of HA-NPs with CD44 and another HA receptor, i.e., hyaluronic acid receptor for endocytosis (HARE) in atherosclerotic lesions [81].

The molecular weight of HA can play an important role in dictating its biological activities. For example, high molecular weight HA (megadaltons, MDa) can suppress inflammation and angiogenesis while low molecular HA oligomers are inflammatory and angiogenic [82-83]. Subsequently, in addition to their CD44 targeting property, HA atheroprotective effect has been investigated through PET/MRI. For instance, HA (MW 66-99 kDa) has been used to prepare radiolabeled HA-NP (89Zr-HA-NP) and further *in vivo* studies have been done in ApoE knockout mouse and rabbit models of atherosclerosis. HA-NP inhibited production of TNFα, IL-2, IL-6 and nitric oxide (NO) by macrophages in vitro. Furthermore, HA-NP treatment stabilized plaques *in vivo*, which increased collagen content of plaques increased up to 30-40% while reducing macrophage content by 30% in comparison with control groups. One hypothesis to explain these observations is that aggregation of HA polymer to form HA-NPs might imitate anti-inflammatory effect of high molecular weight (MDa) HA [84].

2.3.3. Solid Lipid Nanoparticles for Methotrexate Delivery

Methotrexate (MTX) is an immunomodulatory drug that is often used for chronic inflammatory disease [85] and its atheroprotective effect in the presence of systemic inflammation has been the

subject of several studies [86-87]. MTX can decrease inflammatory cytokine production and downregulate expression of adhesion molecule although the specific mechanism has not been fully explained [85, 88]. MTX has been formulated in solid lipid nanoparticle (MTX SPN) for targeted delivery to atherosclerotic plaques. In this formulation MTX has been loaded into the hydrophobic PLGA core and decorated with phospholipids, which were found to decrease inflammatory cytokines production (IL-6 and TNFα) following in vitro incubation with J774.A1 macrophages. Moreover, prepared MTX SPN has been labeled with DiD and rhodamine for fluorescent imaging and has been radiolabeled with 64Cu for further *in vivo* studies. These particles were taken up by macrophages releasing their cargo inside macrophages. In addition, circulating monocytes can uptake them and infiltrate into atherosclerotic plaques. In vivo evaluation of MTX SPN on ApoE knockout mice showed 50% reduction of plaque burden following biweekly administration of 1 mg/kg MTX in one month [29].

Macrophage targeting is a known strategy for atherosclerosis therapy and/or imaging. For example, lipid-latex (LiLa) hybrid nanoparticles have been designed for targeting inflammatory macrophages. In this design, a hydrophobic polymer latex can be a drug reservoir, while lipids bring colloidal stability to the system as well as targeting properties. Phosphatidylserine (PtdSer) and cholesterol-9-carboxynonanoate (9-CCN) have been used as lipid coating. These molecules served as "eat me" signal for macrophages enhancing macrophage uptake [89]. In addition, over-expression of phospholipase A2 (PLA2) [90] in inflammatory macrophages could disrupt lipid coating and trigger drug release inside the macrophages [91]. Testing LiLa NP for imaging atherosclerotic plaques in ApoE knockout mice showed their accumulation in plaques while control bare latex nanoparticle mostly accumulated in the liver. However, LiLa NP may not be a

good candidate for clinical translation to humans due to the poor biodegradability properties of polystyrene latex.

2.4. Oral Delivery of Nanoparticles

Route of nanoparticle administration is another important consideration. While intravenous administration of nanoparticles is commonly utilized, formulation for oral delivery of nanoparticles has been investigated. For example, rosuvastatin has been incorporated into solid lipid nanoparticle (SLN) for oral administration and it led to not only better bioavailability of drug, but also higher decrease of plasma cholesterol and LDL levels compared with free drug [92]. However, these rosuvastatin loaded SLNs have only been investigated under hyperlipidemia-like condition, not in atherosclerotic models.

In another study for oral delivery, rapamycin (Rap) loaded nanoparticles have been prepared through self-assembly of cationic polymer polyethyleneimine (PEI). Rapamycin is an immunosuppressant molecule with antiatherogenic effect [93-94]. These positive charged nanoparticles have been packed into microcapsule obtained from yeast Saccharomyces cerevisiae to form complex yeast-derived microcapsule (YC) [30]. Through the transcytosis mechanism, the YC could be absorbed by M cells in Peyer's patches, which are aggregated lymphoid follicles in the gut [95]. Following the absorption, monocyte and/or macrophages are able to uptake them by endocytosis and relocate them in inflammatory atherosclerotic plaques. In addition to RAP, this nanoparticle system has been tuned to deliver various drugs to atherosclerotic plaques such as ursodeoxycholic acid (UDCA) and sulindac (SUL). Using an oral formulation that can target inflammatory atherosclerotic plaques efficiently is much more convenient than intravenous injections and is advantageous for future clinical translation.

2.5. Conclusion

In conclusion, active targeting of inflammatory atherosclerosis plaques is highly desired for imaging and/or delivering therapeutic molecules to the sites of action. To achieve this goal, a multi task nanocarrier should be designed with the capability of reaching atherosclerosis plaques selectively and releasing its payload. Therefore, this system needs at least two different modalities including the targeting ligand and a releasing trigger with an elaborated design. Although, HDL, the naturally occurring nanoparticle, has inspired scientists to fabricate HDL mimetic nanoparticles, the challenges have not been fully addressed due to high affinity of liver for these particles as well as the relative high cost of ApoA. In addition, physicochemical properties of these nanoparticles should be carefully tuned to get the highest HDL like activity. Loading these nanoparticles with therapeutics and/or diagnostics brings more restrictions in adjusting for desired physicochemical properties. Therefore, researchers are investigating new nanocarriers to deliver anti-inflammatory or anti-proliferative molecules. Among anti-inflammatory therapeutics, statins have been investigated the most due to their applications in the clinic for management of atherosclerosis. With suitably designed nanoparticle systems, significant therapeutic effects towards atherosclerotic plaques can be achieved to reduce the adverse impacts of atherosclerosis.

REFERENCES

REFERENCES

(1) Weber, C.; Noels, H. Atherosclerosis: current pathogenesis and therapeutic options. *Nat. Med.* **2011,** *17* (11), 1410-1422.

(2) Chelly, J.; Mongardon, N.; Dumas, F.; Varenne, O.; Spaulding, C.; Vignaux, O.; Carli, P.; Charpentier, J.; Pène, F.; Chiche, J. D.; Mira, J. P.; Cariou, A. Benefit of an early and systematic imaging procedure after cardiac arrest: insights from the PROCAT (Parisian Region Out of Hospital Cardiac Arrest) registry. *Resuscitation* **2012,** *83* (12), 1444-1450.

(3) Benjamin, E. J.; Blaha, M. J.; Chiuve, S. E.; Cushman, M.; Das, S. R.; Deo, R.; de Ferranti, S. D.; Floyd, J.; Fornage, M.; Gillespie, C.; Isasi, C. R.; Jiménez, M. C.; Jordan, L. C.; Judd, S. E.; Lackland, D.; Lichtman, J. H.; Lisabeth, L.; Liu, S.; Longenecker, C. T.; Mackey, R. H.; Matsushita, K.; Mozaffarian, D.; Mussolino, M. E.; Nasir, K.; Neumar, R. W.; Palaniappan, L.; Pandey, D. K.; Thiagarajan, R. R.; Reeves, M. J.; Ritchey, M.; Rodriguez, C. J.; Roth, G. A.; Rosamond, W. D.; Sasson, C.; Towfighi, A.; Tsao, C. W.; Turner, M. B.; Virani, S. S.; Voeks, J. H.; Willey, J. Z.; Wilkins, J. T.; Wu, J. H.; Alger, H. M.; Wong, S. S.; Muntner, P. Heart disease and stroke statistics—2017 update: a report from the american heart association. *Circulation* **2017,** *135*, https://doi.org/10.1161/CIR.0000000000000485.

(4) Mescher, A. L., The Circulatory System. In *Junqueira's Basic Histology, 14e*, McGraw-Hill Education: New York, NY, 2016.

(5) Sakakura, K.; Nakano, M.; Otsuka, F.; Ladich, E.; Kolodgie, F. D.; Virmani, R. Pathophysiology of atherosclerosis plaque progression. *Heart Lung Circ.* **2013,** *22* (6), 399-411.

(6) Maiolino, G.; Rossitto, G.; Caielli, P.; Bisogni, V.; Rossi, G. P.; Calo, L. A. The Role of Oxidized Low-Density Lipoproteins in Atherosclerosis: The Myths and the Facts. *Mediators of Inflammation* **2013,** *2013*, 13.

(7) Berliner, J. A.; Navab, M.; Fogelman, A. M.; Frank, J. S.; Demer, L. L.; Edwards, P. A.; Watson, A. D.; Lusis, A. J. Atherosclerosis: basic mechanisms. Oxidation, inflammation, and genetics. *Circulation* **1995,** *91* (9), 2488-96.

(8) Derdeyn, C. P.; Chimowitz, M. I. Angioplasty and Stenting for Atherosclerotic Intracranial Stenosis: Rationale for a Randomized Clinical Trial. *Neuroimaging Clin. N. Am.* **2007,** *17* (3), 355-363.

(9) Martínez-González, B.; Reyes-Hernández, C. G.; Quiroga-Garza, A.; Rodríguez-Rodríguez, V. E.; Esparza-Hernández, C. N.; Elizondo-Omaña, R. E.; Guzmán-López, S. Conduits Used in Coronary Artery Bypass Grafting: A Review of Morphological Studies. *Ann. Thorac. Surg.* **2017,** *23* (2), 55-65.

(10) Cerqueira, N. M. F. S. A.; Oliveira, E. F.; Gesto, D. S.; Santos-Martins, D.; Moreira, C.; Moorthy, H. N.; Ramos, M. J.; Fernandes, P. A. Cholesterol Biosynthesis: A Mechanistic Overview. *Biochemistry* **2016,** *55* (39), 5483-5506.

(11) Taylor, F.; Huffman, M. D.; Macedo, A. F.; Moore, T. H. M.; Burke, M.; Davey Smith, G.; Ward, K.; Ebrahim, S. Statins for the primary prevention of cardiovascular disease. *Cochrane Database of Systematic Reviews* **2013,** (1).

(12) Oesterle, A.; Laufs, U.; Liao, J. K. Pleiotropic Effects of Statins on the Cardiovascular System. *Circ. Res.* **2017,** *120* (1), 229-243.

(13) Wolfrum, S.; Jensen, K. S.; Liao, J. K. Endothelium-Dependent Effects of Statins. *Arter. Thromb. Vasc. Biol.* **2003,** *23* (5), 729-736.

(14) Albert, M. A.; Danielson, E.; Rifai, N.; Ridker, P. M. Effect of statin therapy on C-reactive protein levels: the pravastatin inflammation/CRP evaluation (PRINCE): a randomized trial and cohort study. *Jama* **2001,** *286* (1), 64-70.

(15) Pepys, M. B.; Baltz, M. L. Acute phase proteins with special reference to C-reactive protein and related proteins (pentaxins) and serum amyloid A protein. *Adv. Immunol.* **1983,** *34*, 141-212.

(16) Black, S.; Kushner, I.; Samols, D. C-reactive Protein. *J. Biol. Chem.* **2004,** *279* (47), 48487-48490.

(17) Massaro, M.; Zampolli, A.; Scoditti, E.; Carluccio, M. A.; Storelli, C.; Distante, A.; De Caterina, R. Statins inhibit cyclooxygenase-2 and matrix metalloproteinase-9 in human endothelial cells: anti-angiogenic actions possibly contributing to plaque stability. *Cardiovasc. Res.* **2010,** *86* (2), 311-320.

(18) Shao, Q.; Shen, L. H.; Hu, L. H.; Pu, J.; Jing, Q.; He, B. Atorvastatin suppresses inflammatory response induced by oxLDL through inhibition of ERK phosphorylation, IkappaBalpha degradation, and COX-2 expression in murine macrophages. *J. Cell. Biochem.* **2012,** *113* (2), 611-618.

(19) Hernandez-Presa, M. A.; Martin-Ventura, J. L.; Ortego, M.; Gomez-Hernandez, A.; Tunon, J.; Hernandez-Vargas, P.; Blanco-Colio, L. M.; Mas, S.; Aparicio, C.; Ortega, L.; Vivanco, F.; Gerique, J. G.; Diaz, C.; Hernandez, G.; Egido, J. Atorvastatin reduces the expression of cyclooxygenase-2 in a rabbit model of atherosclerosis and in cultured vascular smooth muscle cells. *Atherosclerosis* **2002,** *160* (1), 49-58.

(20) Gately, S.; Li, W. W. Multiple roles of COX-2 in tumor angiogenesis: a target for antiangiogenic therapy. *Semin. Oncol.* **2004,** *31* (2 Suppl 7), 2-11.

(21) Burleigh, M. E.; Babaev, V. R.; Yancey, P. G.; Major, A. S.; McCaleb, J. L.; Oates, J. A.; Morrow, J. D.; Fazio, S.; Linton, M. F. Cyclooxygenase-2 promotes early atherosclerotic lesion formation in ApoE-deficient and C57BL/6 mice. *J. Mol. Cell. Cardiol.* **2005,** *39* (3), 443-452.

(22) Autieri, M. V. Pro- and Anti-Inflammatory Cytokine Networks in Atherosclerosis. *ISRN Vascular Medicine* **2012,** *2012*, 17.

(23) Ascer, E.; Bertolami, M. C.; Venturinelli, M. L.; Buccheri, V.; Souza, J.; Nicolau, J. C.; Ramires, J. A.; Serrano, C. V., Jr. Atorvastatin reduces proinflammatory markers in hypercholesterolemic patients. *Atherosclerosis* **2004,** *177* (1), 161-6.

(24) Tawakol, A.; Fayad, Z. A.; Mogg, R.; Alon, A.; Klimas, M. T.; Dansky, H.; Subramanian, S. S.; Abdelbaky, A.; Rudd, J. H.; Farkouh, M. E.; Nunes, I. O.; Beals, C. R.; Shankar, S. S. Intensification of statin therapy results in a rapid reduction in atherosclerotic inflammation: results of a multicenter fluorodeoxyglucose-positron emission tomography/computed tomography feasibility study. *J. Am. Coll. Cardiol.* **2013,** *62* (10), 909-917.

(25) Nissen, S. E.; Nicholls, S. J.; Sipahi, I.; et al. Effect of very high-intensity statin therapy on regression of coronary atherosclerosis: The asteroid trial. *Jama* **2006,** *295* (13), 1556-1565.

(26) Spencer, F. A.; Fonarow, G. C.; Frederick, P. D.; Wright, R. S.; Every, N.; Goldberg, R. J.; Gore, J. M.; Dong, W.; Becker, R. C.; French, W. Early withdrawal of statin therapy in patients with non-ST-segment elevation myocardial infarction: national registry of myocardial infarction. *Arch. Intern. Med.* **2004,** *164* (19), 2162-2168.

(27) Heeschen, C.; Hamm, C. W.; Laufs, U.; Snapinn, S.; Bohm, M.; White, H. D. Withdrawal of statins increases event rates in patients with acute coronary syndromes. *Circulation* **2002,** *105* (12), 1446-52.

(28) Ridker, P. M.; Everett, B. M.; Thuren, T.; MacFadyen, J. G.; Chang, W. H.; Ballantyne, C.; Fonseca, F.; Nicolau, J.; Koenig, W.; Anker, S. D.; Kastelein, J. J. P.; Cornel, J. H.; Pais, P.; Pella, D.; Genest, J.; Cifkova, R.; Lorenzatti, A.; Forster, T.; Kobalava, Z.; Vida-Simiti, L.; Flather, M.; Shimokawa, H.; Ogawa, H.; Dellborg, M.; Rossi, P. R. F.; Troquay, R. P. T.; Libby, P.; Glynn, R. J. Antiinflammatory Therapy with Canakinumab for Atherosclerotic Disease. *The New England journal of medicine* **2017,** *377* (12), 1119-1131.

(29) Stigliano, C.; Ramirez, M. R.; Singh, J. V.; Aryal, S.; Key, J.; Blanco, E.; Decuzzi, P. Methotraxate-Loaded Hybrid Nanoconstructs Target Vascular Lesions and Inhibit Atherosclerosis Progression in ApoE−/− Mice. *Adv. Healthcare Mater.* **2017,** *6* (13), 1601286.

(30) Zhang, X.; Xu, X.; Chen, Y.; Dou, Y.; Zhou, X.; Li, L.; Li, C.; An, H.; Tao, H.; Hu, H.; Li, X.; Zhang, J. Bioinspired yeast microcapsules loaded with self-assembled nanotherapies for targeted treatment of cardiovascular disease. *Mater. Today* **2017,** *20* (6), 301-313.

(31) Lobatto, M. E.; Fayad, Z. A.; Silvera, S.; Vucic, E.; Calcagno, C.; Mani, V.; Dickson, S. D.; Nicolay, K.; Banciu, M.; Schiffelers, R. M.; Metselaar, J. M.; van Bloois, L.; Wu, H.-S.; Fallon, J. T.; Rudd, J. H.; Fuster, V.; Fisher, E. A.; Storm, G.; Mulder, W. J. M. Multimodal Clinical Imaging To Longitudinally Assess a Nanomedical Anti-Inflammatory Treatment in Experimental Atherosclerosis. *Mol. Pharm.* **2010,** *7* (6), 2020-2029.

(32) van der Valk, F. M.; Schulte, D. M.; Meiler, S.; Tang, J.; Zheng, K. H.; Van den Bossche, J.; Seijkens, T.; Laudes, M.; de Winther, M.; Lutgens, E.; Alaarg, A.; Metselaar, J. M.; Dallinga-Thie, G. M.; Mulder, W. J.; Stroes, E. S.; Hamers, A. A. Liposomal prednisolone promotes macrophage lipotoxicity in experimental atherosclerosis. *Nanomedicine : nanotechnology, biology, and medicine* **2016,** *12* (6), 1463-70.

(33) Gomez, D.; Baylis, R. A.; Durgin, B. G.; Newman, A. A. C.; Alencar, G. F.; Mahan, S.; St. Hilaire, C.; Müller, W.; Waisman, A.; Francis, S. E.; Pinteaux, E.; Randolph, G. J.; Gram, H.; Owens, G. K. Interleukin-1β has atheroprotective effects in advanced atherosclerotic lesions of mice. *Nat. Med.* **2018,** *24* (9), 1418-1429.

(34) Kircher, M. F.; Grimm, J.; Swirski, F. K.; Libby, P.; Gerszten, R. E.; Allport, J. R.; Weissleder, R. Noninvasive in vivo imaging of monocyte trafficking to atherosclerotic lesions. *Circulation* **2008,** *117* (3), 388-95.

(35) Klug, G.; Kampf, T.; Ziener, C.; Parczyk, M.; Bauer, E.; Herold, V.; Rommel, E.; Jakob, P. M.; Bauer, W. R. Murine atherosclerotic plaque imaging with the USPIO Ferumoxtran-10. *Front. Biosci. (Landmark Ed)* **2009,** *14*, 2546-2552.

(36) Tarin, C.; Carril, M.; Martin-Ventura, J. L.; Markuerkiaga, I.; Padro, D.; Llamas-Granda, P.; Moreno, J. A.; Garcia, I.; Genicio, N.; Plaza-Garcia, S.; Blanco-Colio, L. M.; Penades, S.; Egido, J. Targeted gold-coated iron oxide nanoparticles for CD163 detection in atherosclerosis by MRI. *Scientific reports* **2015,** *5*, 17135.

(37) El-Dakdouki, M. H.; El-Boubbou, K.; Kamat, M.; Huang, R.; Abela, G. S.; Kiupel, M.; Zhu, D. C.; Huang, X. CD44 targeting magnetic glyconanoparticles for atherosclerotic plaque imaging. *Pharm. Res.* **2014,** *31* (6), 1426-1437.

(38) Yu, Z.; Geng, J.; Tan, Y.; Wang, Q.; Zhu, J.; Zhang, M. Non-invasive assessment of acute vascular inflammation after PCI using USPIO enhanced MRI in vivo. *Int. J. Cardiol.* **2011,** *151* (1), 110-112.

(39) Tsuchiya, K.; Nitta, N.; Sonoda, A.; Otani, H.; Takahashi, M.; Murata, K.; Shiomi, M.; Tabata, Y.; Nohara, S. Atherosclerotic imaging using 4 types of superparamagnetic iron oxides: new possibilities for mannan-coated particles. *Eur. J. Radiol.* **2013,** *82* (11), 1919-1925.

(40) Daugherty, A.; Dunn, J. L.; Rateri, D. L.; Heinecke, J. W. Myeloperoxidase, a catalyst for lipoprotein oxidation, is expressed in human atherosclerotic lesions. *J. Clin. Invest.* **1994,** *94* (1), 437-444.

(41) Ronald, J. A.; Chen, J. W.; Chen, Y.; Hamilton, A. M.; Rodriguez, E.; Reynolds, F.; Hegele, R. A.; Rogers, K. A.; Querol, M.; Bogdanov, A.; Weissleder, R.; Rutt, B. K. Enzyme-sensitive magnetic resonance imaging targeting myeloperoxidase identifies active inflammation in experimental rabbit atherosclerotic plaques. *Circulation* **2009,** *120* (7), 592-9.

(42) Nie, S.; Zhang, J.; Martinez-Zaguilan, R.; Sennoune, S.; Hossen, M. N.; Lichtenstein, A. H.; Cao, J.; Meyerrose, G. E.; Paone, R.; Soontrapa, S.; Fan, Z.; Wang, S. Detection of atherosclerotic lesions and intimal macrophages using CD36-targeted nanovesicles. *J. Control. Release* **2015,** *220* (Pt A), 61-70.

(43) Seimon, T. A.; Nadolski, M. J.; Liao, X.; Magallon, J.; Nguyen, M.; Feric, N. T.; Koschinsky, M. L.; Harkewicz, R.; Witztum, J. L.; Tsimikas, S.; Golenbock, D.; Moore, K. J.; Tabas, I. Atherogenic lipids and lipoproteins trigger CD36-TLR2-dependent apoptosis in macrophages undergoing endoplasmic reticulum stress. *Cell Metab.* **2010,** *12* (5), 467-482.

(44) Collot-Teixeira, S.; Martin, J.; McDermott-Roe, C.; Poston, R.; McGregor, J. L. CD36 and macrophages in atherosclerosis. *Cardiovasc. Res.* **2007,** *75* (3), 468-477.

(45) Podrez, E. A.; Poliakov, E.; Shen, Z.; Zhang, R.; Deng, Y.; Sun, M.; Finton, P. J.; Shan, L.; Gugiu, B.; Fox, P. L.; Hoff, H. F.; Salomon, R. G.; Hazen, S. L. Identification of a novel family of oxidized phospholipids that serve as ligands for the macrophage scavenger receptor CD36. *J. Biol. Chem.* **2002,** *277* (41), 38503-38516.

(46) Matsui, Y.; Rittling, S. R.; Okamoto, H.; Inobe, M.; Jia, N.; Shimizu, T.; Akino, M.; Sugawara, T.; Morimoto, J.; Kimura, C.; Kon, S.; Denhardt, D.; Kitabatake, A.; Uede, T. Osteopontin Deficiency Attenuates Atherosclerosis in Female Apolipoprotein E–Deficient Mice. *Arter. Thromb. Vasc. Biol.* **2003,** *23* (6), 1029-1034.

(47) Scatena, M.; Liaw, L.; Giachelli, C. M. Osteopontin: a multifunctional molecule regulating chronic inflammation and vascular disease. *Arterioscler. Thromb. Vasc. Biol.* **2007,** *27* (11), 2302-2309.

(48) Qiao, R.; Qiao, H.; Zhang, Y.; Wang, Y.; Chi, C.; Tian, J.; Zhang, L.; Cao, F.; Gao, M. Molecular Imaging of Vulnerable Atherosclerotic Plaques in Vivo with Osteopontin-Specific Upconversion Nanoprobes. *ACS Nano* **2017,** *11* (2), 1816-1825.

(49) Sarai, M.; Hartung, D.; Petrov, A.; Zhou, J.; Narula, N.; Hofstra, L.; Kolodgie, F.; Isobe, S.; Fujimoto, S.; Vanderheyden, J. L.; Virmani, R.; Reutelingsperger, C.; Wong, N. D.; Gupta, S.; Narula, J. Broad and specific caspase inhibitor-induced acute repression of apoptosis in atherosclerotic lesions evaluated by radiolabeled annexin A5 imaging. *J. Am. Coll. Cardiol.* **2007,** *50* (24), 2305-2312.

(50) Li, X.; Wang, C.; Tan, H.; Cheng, L.; Liu, G.; Yang, Y.; Zhao, Y.; Zhang, Y.; Li, Y.; Zhang, C.; Xiu, Y.; Cheng, D.; Shi, H. Gold nanoparticles-based SPECT/CT imaging probe targeting for vulnerable atherosclerosis plaques. *Biomaterials* **2016,** *108*, 71-80.

(51) Hamzah, J.; Kotamraju, V. R.; Seo, J. W.; Agemy, L.; Fogal, V.; Mahakian, L. M.; Peters, D.; Roth, L.; Gagnon, M. K. J.; Ferrara, K. W.; Ruoslahti, E. Specific penetration and accumulation of a homing peptide within atherosclerotic plaques of apolipoprotein E-deficient mice. *Proc. Natl. Acad. Sci. U.S.A.* **2011,** *108* (17), 7154-7159.

(52) Sun, X.; Li, W.; Zhang, X.; Qi, M.; Zhang, Z.; Zhang, X.-E.; Cui, Z. In Vivo Targeting and Imaging of Atherosclerosis Using Multifunctional Virus-Like Particles of Simian Virus 40. *Nano Lett.* **2016,** *16* (10), 6164-6171.

(53) Winter, P. M.; Morawski, A. M.; Caruthers, S. D.; Fuhrhop, R. W.; Zhang, H.; Williams, T. A.; Allen, J. S.; Lacy, E. K.; Robertson, J. D.; Lanza, G. M.; Wickline, S. A. Molecular imaging of angiogenesis in early-stage atherosclerosis with alpha(v)beta3-integrin-targeted nanoparticles. *Circulation* **2003,** *108* (18), 2270-4.

(54) Khodabandehlou, K.; Masehi-Lano, J. J.; Poon, C.; Wang, J.; Chung, E. J. Targeting cell adhesion molecules with nanoparticles using in vivo and flow-based in vitro models of atherosclerosis. *Exp. Biol. Med. (Maywood)* **2017,** *242* (8), 799-812.

(55) Bruckman, M. A.; Jiang, K.; Simpson, E. J.; Randolph, L. N.; Luyt, L. G.; Yu, X.; Steinmetz, N. F. Dual-Modal Magnetic Resonance and Fluorescence Imaging of Atherosclerotic Plaques in Vivo Using VCAM-1 Targeted Tobacco Mosaic Virus. *Nano Letters* **2014,** *14* (3), 1551-1558.

(56) Serrano, D.; Bhowmick, T.; Chadha, R.; Garnacho, C.; Muro, S. Intercellular adhesion molecule 1 engagement modulates sphingomyelinase and ceramide, supporting uptake of drug carriers by the vascular endothelium. *Arterioscler. Thromb. Vasc. Biol.* **2012,** *32* (5), 1178-1185.

(57) Ma, S.; Tian, X. Y.; Zhang, Y.; Mu, C.; Shen, H.; Bismuth, J.; Pownall, H. J.; Huang, Y.; Wong, W. T. E-selectin-targeting delivery of microRNAs by microparticles ameliorates endothelial inflammation and atherosclerosis. *Sci. Rep.* **2016,** *6*, 22910.

(58) Murata, K.; Motayama, T.; Kotake, C. Collagen types in various layers of the human aorta and their changes with the atherosclerotic process. *Atherosclerosis* **1986,** *60* (3), 251-62.

(59) Chan, J. M.; Zhang, L.; Tong, R.; Ghosh, D.; Gao, W.; Liao, G.; Yuet, K. P.; Gray, D.; Rhee, J.-W.; Cheng, J.; Golomb, G.; Libby, P.; Langer, R.; Farokhzad, O. C. Spatiotemporal controlled delivery of nanoparticles to injured vasculature. *Proc. Natl. Acad. Sci. U.S.A.* **2010,** *107* (5), 2213-2218.

(60) Fredman, G.; Kamaly, N.; Spolitu, S.; Milton, J.; Ghorpade, D.; Chiasson, R.; Kuriakose, G.; Perretti, M.; Farokzhad, O.; Tabas, I. Targeted nanoparticles containing the proresolving peptide Ac2-26 protect against advanced atherosclerosis in hypercholesterolemic mice. *Sci. Transl. Med.* **2015,** *7* (275), 275ra20.

(61) Kamaly, N.; Fredman, G.; Fojas, J. J. R.; Subramanian, M.; Choi, W., II; Zepeda, K.; Vilos, C.; Yu, M.; Gadde, S.; Wu, J.; Milton, J.; Carvalho Leitao, R.; Rosa Fernandes, L.; Hasan, M.; Gao, H.; Nguyen, V.; Harris, J.; Tabas, I.; Farokhzad, O. C. Targeted Interleukin-10 Nanotherapeutics Developed with a Microfluidic Chip Enhance Resolution of Inflammation in Advanced Atherosclerosis. *ACS Nano* **2016,** *10* (5), 5280-5292.

(62) Romeo, G. R.; Moulton, K. S.; Kazlauskas, A. Attenuated expression of profilin-1 confers protection from atherosclerosis in the LDL receptor null mouse. *Circ. Res.* **2007,** *101* (4), 357-367.

(63) Wang, Y.; Chen, J.; Yang, B.; Qiao, H.; Gao, L.; Su, T.; Ma, S.; Zhang, X.; Li, X.; Liu, G.; Cao, J.; Chen, X.; Chen, Y.; Cao, F. In vivo MR and Fluorescence Dual-modality Imaging of Atherosclerosis Characteristics in Mice Using Profilin-1 Targeted Magnetic Nanoparticles. *Theranostics* **2016,** *6* (2), 272-86.

(64) Wang, N.; Lan, D.; Chen, W.; Matsuura, F.; Tall, A. R. ATP-binding cassette transporters G1 and G4 mediate cellular cholesterol efflux to high-density lipoproteins. *Proc. Natl. Acad. Sci. U.S.A.* **2004,** *101* (26), 9774-9779.

(65) Duong, M.; Collins, H. L.; Jin, W.; Zanotti, I.; Favari, E.; Rothblat, G. H. Relative contributions of ABCA1 and SR-BI to cholesterol efflux to serum from fibroblasts and macrophages. *Arterioscler. Thromb. Vasc. Biol.* **2006,** *26* (3), 541-547.

(66) Gordon, S. M.; Deng, J.; Lu, L. J.; Davidson, W. S. Proteomic characterization of human plasma high density lipoprotein fractionated by gel filtration chromatography. *J. Proteome. Res.* **2010,** *9* (10), 5239-5249.

(67) Sanchez-Gaytan, B. L.; Fay, F.; Lobatto, M. E.; Tang, J.; Ouimet, M.; Kim, Y.; van der Staay, S. E. M.; van Rijs, S. M.; Priem, B.; Zhang, L.; Fisher, E. A.; Moore, K. J.; Langer, R.; Fayad, Z. A.; Mulder, W. J. M. HDL-Mimetic PLGA Nanoparticle To Target Atherosclerosis Plaque Macrophages. *Bioconjug. Chem.* **2015,** *26* (3), 443-451.

(68) Tall, A. R.; Yvan-Charvet, L.; Terasaka, N.; Pagler, T.; Wang, N. HDL, ABC transporters, and cholesterol efflux: implications for the treatment of atherosclerosis. *Cell Metab.* **2008,** *7* (5), 365-375.

(69) Tang, J.; Baxter, S.; Menon, A.; Alaarg, A.; Sanchez-Gaytan, B. L.; Fay, F.; Zhao, Y.; Ouimet, M.; Braza, M. S.; Longo, V. A.; Abdel-Atti, D.; Duivenvoorden, R.; Calcagno, C.; Storm, G.; Tsimikas, S.; Moore, K. J.; Swirski, F. K.; Nahrendorf, M.; Fisher, E. A.; Perez-Medina, C.; Fayad, Z. A.; Reiner, T.; Mulder, W. J. Immune cell screening of a nanoparticle library improves atherosclerosis therapy. *Proceedings of the National Academy of Sciences of the United States of America* **2016,** *113* (44), E6731-e6740.

(70) Duivenvoorden, R.; Tang, J.; Cormode, D. P.; Mieszawska, A. J.; Izquierdo-Garcia, D.; Ozcan, C.; Otten, M. J.; Zaidi, N.; Lobatto, M. E.; van Rijs, S. M.; Priem, B.; Kuan, E. L.; Martel, C.; Hewing, B.; Sager, H.; Nahrendorf, M.; Randolph, G. J.; Stroes, E. S. G.; Fuster, V.; Fisher, E. A.; Fayad, Z. A.; Mulder, W. J. M. A Statin-Loaded Reconstituted High-Density Lipoprotein Nanoparticle Inhibits Atherosclerotic Plaque Inflammation. *Nat. Commun.* **2014,** *5*, 3065-3065.

(71) Zhang, W.; He, H.; Liu, J.; Wang, J.; Zhang, S.; Zhang, S.; Wu, Z. Pharmacokinetics and atherosclerotic lesions targeting effects of tanshinone IIA discoidal and spherical biomimetic high density lipoproteins. *Biomaterials* **2013,** *34* (1), 306-19.

(72) Zhang, M.; Jia, J.; Liu, J.; He, H.; Liu, L. A novel modified paclitaxel-loaded discoidal recombinant high-density lipoproteins: Preparation, characterizations and in vivo evaluation. *Asian J. Pharm.* **2013,** *8* (1), 11-18.

(73) He, H.; Liu, L.; Bai, H.; Wang, J.; Zhang, Y.; Zhang, W.; Zhang, M.; Wu, Z.; Liu, J. Arachidonic acid-modified lovastatin discoidal reconstituted high density lipoprotein markedly decreases the drug leakage during the remodeling behaviors induced by lecithin cholesterol acyltransferase. *Pharm. Res.* **2014,** *31* (7), 1689-1709.

(74) He, H.; Zhang, M.; Liu, L.; Zhang, S.; Liu, J.; Zhang, W. Suppression of Remodeling Behaviors with Arachidonic Acid Modification for Enhanced in vivo Antiatherogenic Efficacies of Lovastatin-loaded Discoidal Recombinant High Density Lipoprotein. *Pharm. Res.* **2015,** *32* (10), 3415-3431.

(75) de Winther, M. P.; van Dijk, K. W.; Havekes, L. M.; Hofker, M. H. Macrophage scavenger receptor class A: A multifunctional receptor in atherosclerosis. *Arterioscler. Thromb. Vasc. Biol.* **2000,** *20* (2), 290-297.

(76) Chao, Y.; Makale, M.; Karmali, P. P.; Sharikov, Y.; Tsigelny, I.; Merkulov, S.; Kesari, S.; Wrasidlo, W.; Ruoslahti, E.; Simberg, D. Recognition of dextran-superparamagnetic iron oxide nanoparticle conjugates (Feridex) via macrophage scavenger receptor charged domains. *Bioconjugate chem.* **2012,** *23* (5), 1003-1009.

(77) Zhao, Y.; Jiang, C.; He, J.; Guo, Q.; Lu, J.; Yang, Y.; Zhang, W.; Liu, J. Multifunctional Dextran Sulfate-Coated Reconstituted High Density Lipoproteins Target Macrophages and Promote Beneficial Antiatherosclerotic Mechanisms. *Bioconjug. Chem.* **2017,** *28* (2), 438-448.

(78) Slevin, M.; Krupinski, J.; Gaffney, J.; Matou, S.; West, D.; Delisser, H.; Savani, R. C.; Kumar, S. Hyaluronan-mediated angiogenesis in vascular disease: uncovering RHAMM and CD44 receptor signaling pathways. *Matrix Biol.* **2007,** *26* (1), 58-68.

(79) Zhang, M.; He, J.; Jiang, C.; Zhang, W.; Yang, Y.; Wang, Z.; Liu, J. Plaque-hyaluronidase-responsive high-density-lipoprotein-mimetic nanoparticles for multistage intimal-macrophage-targeted drug delivery and enhanced anti-atherosclerotic therapy. *Int. J. Nanomed.* **2017,** *12*, 533-558.

(80) Liu, L.; He, H.; Zhang, M.; Zhang, S.; Zhang, W.; Liu, J. Hyaluronic acid-decorated reconstituted high density lipoprotein targeting atherosclerotic lesions. *Biomaterials* **2014,** *35* (27), 8002-14.

(81) Lee, G. Y.; Kim, J. H.; Choi, K. Y.; Yoon, H. Y.; Kim, K.; Kwon, I. C.; Choi, K.; Lee, B. H.; Park, J. H.; Kim, I. S. Hyaluronic acid nanoparticles for active targeting atherosclerosis. *Biomaterials* **2015,** *53*, 341-8.

(82) Rooney, P.; Kumar, S.; Ponting, J.; Wang, M. The role of hyaluronan in tumour neovascularization (review). *Int. J. Cancer* **1995,** *60* (5), 632-636.

(83) Masuko, K.; Murata, M.; Yudoh, K.; Kato, T.; Nakamura, H. Anti-inflammatory effects of hyaluronan in arthritis therapy: Not just for viscosity. *Int. J. Gen. Med.* **2009,** *2*, 77-81.

(84) Beldman, T. J.; Senders, M. L.; Alaarg, A.; Pérez-Medina, C.; Tang, J.; Zhao, Y.; Fay, F.; Deichmöller, J.; Born, B.; Desclos, E.; van der Wel, N. N.; Hoebe, R. A.; Kohen, F.; Kartvelishvily, E.; Neeman, M.; Reiner, T.; Calcagno, C.; Fayad, Z. A.; de Winther, M. P. J.; Lutgens, E.; Mulder, W. J. M.; Kluza, E. Hyaluronan Nanoparticles Selectively Target Plaque-Associated Macrophages and Improve Plaque Stability in Atherosclerosis. *ACS Nano* **2017,** *11* (6), 5785-5799.

(85) Chan, E. S.; Cronstein, B. N. Molecular action of methotrexate in inflammatory diseases. *Arthritis Res. Ther.* **2002,** *4* (4), 266-273.

(86) Bulgarelli, A.; Martins Dias, A. A.; Caramelli, B.; Maranhao, R. C. Treatment with methotrexate inhibits atherogenesis in cholesterol-fed rabbits. *J. Cardiovasc. Pharmacol.* **2012,** *59* (4), 308-314.

(87) Ronda, N.; Greco, D.; Adorni, M. P.; Zimetti, F.; Favari, E.; Hjeltnes, G.; Mikkelsen, K.; Borghi, M. O.; Favalli, E. G.; Gatti, R.; Hollan, I.; Meroni, P. L.; Bernini, F. Newly identified antiatherosclerotic activity of methotrexate and adalimumab: complementary effects on lipoprotein function and macrophage cholesterol metabolism. *Arthritis Rheumatol.* **2015,** *67* (5), 1155-1164.

(88) Gerards, A. H.; de Lathouder, S.; de Groot, E. R.; Dijkmans, B. A. C.; Aarden, L. A. Inhibition of cytokine production by methotrexate. Studies in healthy volunteers and patients with rheumatoid arthritis. *Rheumatology* **2003,** *42* (10), 1189-1196.

(89) Poon, I. K. H.; Lucas, C. D.; Rossi, A. G.; Ravichandran, K. S. Apoptotic cell clearance: basic biology and therapeutic potential. *Nat. Rev. Immunol.* **2014,** *14*, 166-180.

(90) Goncalves, I.; Edsfeldt, A.; Ko, N. Y.; Grufman, H.; Berg, K.; Bjorkbacka, H.; Nitulescu, M.; Persson, A.; Nilsson, M.; Prehn, C.; Adamski, J.; Nilsson, J. Evidence supporting a key role of Lp-PLA2-generated lysophosphatidylcholine in human atherosclerotic plaque inflammation. *Arterioscler. Thromb. Vasc. Biol.* **2012,** *32* (6), 1505-1512.

(91) Bagalkot, V.; Badgeley, M. A.; Kampfrath, T.; Deiuliis, J. A.; Rajagopalan, S.; Maiseyeu, A. Hybrid nanoparticles improve targeting to inflammatory macrophages through phagocytic signals. *J. Control. Release* **2015,** *217*, 243-55.

(92) Beg, S.; Jain, S.; Kushwah, V.; Bhatti, G. K.; Sandhu, P. S.; Katare, O. P.; Singh, B. Novel surface-engineered solid lipid nanoparticles of rosuvastatin calcium for low-density lipoprotein-receptor targeting: a Quality by Design-driven perspective. *Nanomedicine (London, England)* **2017,** *12* (4), 333-356.

(93) Waksman, R.; Pakala, R.; Burnett, M. S.; Gulick, C. P.; Leborgne, L.; Fournadjiev, J.; Wolfram, R.; Hellinga, D. Oral rapamycin inhibits growth of atherosclerotic plaque in apoE knock-out mice. *Cardiovasc. Radiat. Med.* **2003,** *4* (1), 34-38.

(94) Castro, C.; Campistol, J. M.; Sancho, D.; Sánchez-Madrid, F.; Casals, E.; Andrés, V. Rapamycin attenuates atherosclerosis induced by dietary cholesterol in apolipoprotein-deficient mice through a p27^{Kip1}-independent pathway. *Atherosclerosis* **2004,** *172* (1), 31-38.

(95) Jung, C.; Hugot, J.-P.; Barreau, F. Peyer's Patches: The Immune Sensors of the Intestine. *International Journal of Inflammation* **2010,** *2010*, 823710.

Chapter 3: Hyaluronan Conjugated Nanoprobes for Imaging Inflammatory Atherosclerotic Plaques; Effects of Nanoprobe Shape on Cellular Binding and Inflammatory Responses

Adapted with permission from:

Effects of Nanoprobe Morphology on Cellular Binding and Inflammatory Responses: Hyaluronan Conjugated Magnetic Nanoworms for Magnetic Resonance Imaging of Atherosclerosis Plaques, Seyedmehdi Hossaini Nasr, Anne Tonson, Mohammad H. El-dakdouki, David C. Zhu, Dalen Agnew, Robert Wiseman, Chunqi Qian, and Xuefei Huang, *ACS Appl. Mater. Interfaces*, **2018**, 10 (14), 11495-11507. Copyright (2018). American Chemical Society.

3.1. Introduction

Atherosclerosis, the thickening of arterial vessel walls as a result of invasion and accumulation of inflammatory cells and lipids, is a major cause of heart attacks and strokes[1]. The majority of patients that experience cardiac arrests have atherosclerosis[2]. Early detection via non-invasive methods is highly attractive to guide the prevention and the treatment of this disease[3].

Imaging of atherosclerosis plaques is an active area of research[4-5]. Compared to techniques such as positron emission tomography (PET) and/or computed tomography (CT), magnetic resonance imaging (MRI) is advantageous as it does not use ionizing radiation while giving superior spatial resolution *in vivo*[6-7]. Furthermore, contrast agents can be developed to enhance the sensitivity of atherosclerotic plaque detection by MRI[8-9]. There are two general classes of contrast agents. The first are passive agents, which can diffuse into plaques or be taken up by macrophages capable of trafficking to plaques. The second are active agents designed to bind with receptors over-expressed by plaques, enabling selective accumulation in plaques and contrast changes from surrounding tissues.

To achieve active targeting, the selection of a suitable receptor target is important. CD44 is a cell surface receptor critical for recruitment of inflammatory cells to atherosclerotic plaques[10-11]. In histological analysis of atherosclerotic plaques in both humans and an atherosclerotic animal model, i.e., ApoE knockout mice, CD44 has been found to be expressed at much higher levels (> 10 fold) in plaque regions that are prone to rupture compared to those in healthy vascular tissues[10, 12-15]. Knocking down CD44 expression levels in ApoE knockout mice reduced aortic lesions for more than 50%[12].

The major endogenous ligand for CD44 is the polysaccharide hyaluronan (HA)[16-17]. CD44 is normally kept in a quiescent state with low HA affinity. However, in the presence of inflammatory signals such as TNF-α that are common in atherosclerotic plaques, post-translational modification of CD44 occurs, switching it to a high affinity state for strong HA binding[11, 18]. Thus, HA can be a useful ligand to target CD44 and sense inflammation in atherosclerotic plaques[19-22]. We synthesized HA coated super paramagnetic iron oxide nanoparticles (HA-SPIONs), which have been used to image atherosclerotic plaques in rabbits by MRI[20]. One potential concern of SPION based system is their inflammatory activities. Herein, we report that engineering the spherical shape of HA-SPIONs to worm like structures of HA-nanoworm (HA-NWs) can significantly reduce their inflammatory activities. Furthermore, HA-NWs have much higher binding avidity with CD44 expressing cells. This new nanoprobe enables successful non-invasive detection of atherosclerotic plaques by MRI in ApoE knockout mice, a suitable model of human atherosclerosis diseases. This work highlights the significant impacts morphology can have on biological functions of nanoprobes.

3.2. Synthesis and Characterization of HA-NWs

Synthesis of HA-NWs started from dextran coated superparamagnetic iron oxide nanoworms (NWs), which were prepared through the co-precipitation of Fe^{2+} and Fe^{3+} ions in the presence of dextran (40 kDa)[23]. Amine groups were introduced onto NWs by first crosslinking the surface dextran with epichlorohydrin followed by treatment with ammonia. HA was then conjugated onto aminated NWs through 2-chloro-4,6-dimethoxy-1,3,5-triazine (CDMT) mediated amide bond formation[19] leading to HA-NWs **Figure 3-1a**. The morphology of HA-NWs was characterized through TEM, which showed elongated shape of the HA-NWs with each NW containing multiple NP cores. Analysis of TEM images of HA-NWs revealed that the average length of HA-NW core

is 65±15 nm, corresponding to 10 – 20 NPs forming a single chain for each NW **Figure 3-1b**. For comparison, the spherical shaped SPIONs with dextran coating were synthesized following a previously established procedure using dextran with average molecular weight of 10 kDa[19]. Subsequent introduction of HA onto SPIONs produced HA-SPIONs. TEM showed the spherical shape of HA-SPION with the average diameter of iron oxide core of 6 nm **Figure 3-1c**. The key parameter in determining shape of the nano-construct is the molecular weight of dextran. Presumably, in the presence of higher molecular weight (40 kDa) of dextran during NW formation, the dextran coating on NPs linked multiple NPs together forming NWs.

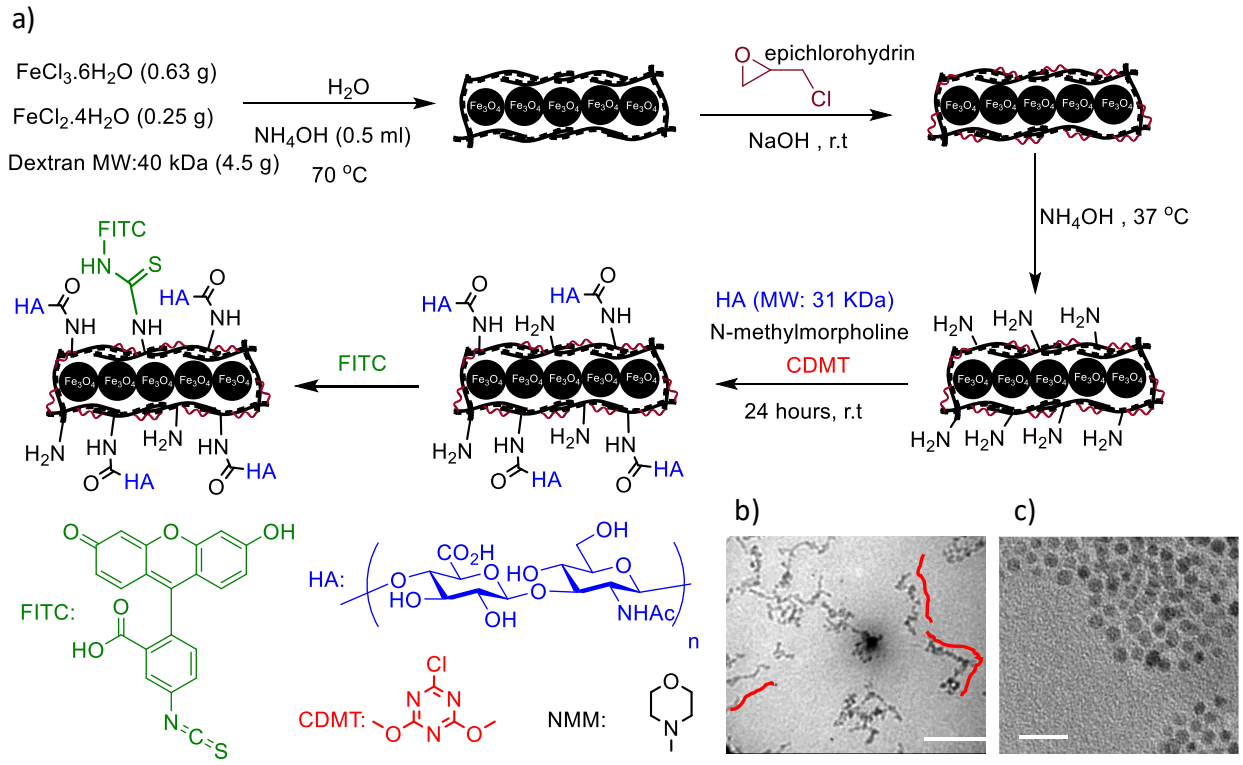

Figure 3-1. a) Synthesis of HA-NWs. b) TEM images for HA-NWs showed the elongated shape of HA-NWs. Three representative worms were traced with red lines. c) TEM image for HA-SPIONs showed spherical morphology. Scale bars are 50 nm and 20 nm for b and c respectively.

The NW surface modification processes leading to HA-NWs were conveniently monitored by zeta potential analysis. The zeta potential value of as synthesized NWs is -6.0 mV in PBS buffer. Upon amination, the zeta potential became +4.5 mV due to the introduction of positively charged ammonium ions on the surface. The introduction of negatively charged HA onto aminated NWs decreased the zeta potential to -16 mV suggesting the successful conjugation of HA. The zeta potential of the corresponding HA-SPIONs was -14 mV, similar to that of HA-NWs. The hydrodynamic diameter of the HA-NW was 127 nm, increased from 93 nm for unmodified NWs. To facilitate tracking of the nanoprobes, FITC was introduced onto HA-NWs and HA-SPIONs producing FITC-HA-NWs and FITC-HA-SPIONs. The r_2* magnetic relaxivity of HA-NWs was determined to be 110 (sec mMFe)$^{-1}$ at 7 T and while the r_2* value was 52 (sec mMFe)$^{-1}$ for the corresponding HA-SPIONs. The high r_2* value suggests HA-NWs are good MR contrast agents **Figure 3-2**.

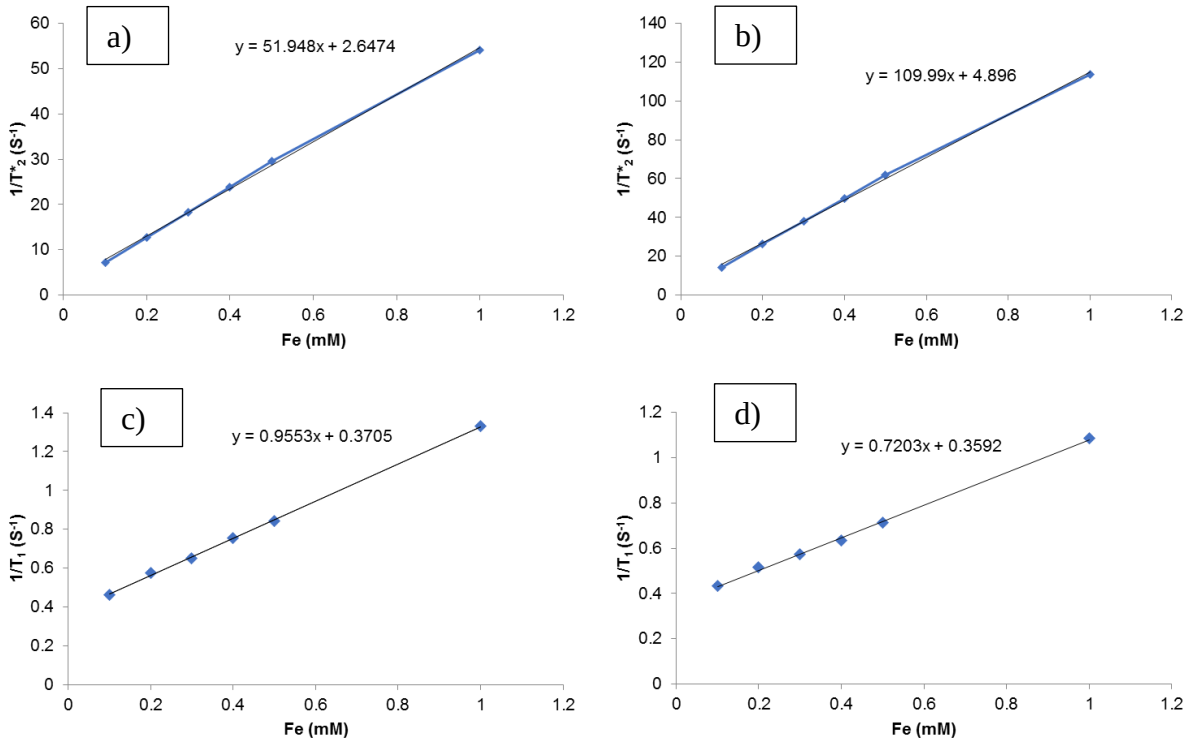

Figure 3-2. r_2* and r_1 measurements for prepared nanoparticles in a 7 T magnet. (a,c) are r_2* and r_1 for HA-SPIONs respectively. (b,d) are are r_2* and r_1 for HA-NWs respectively.

For biological applications of HA-NWs, it is important to ensure that all HA in a sample of HA-NWs is conjugated with NWs, as residual free HA can potentially compete with HA-NWs for binding with CD44. To test this, we developed a new gel electrophoresis assay. Free HA, HA-SPION and HA-NW were electrophoresed on an agarose gel (0.8%) and stained with the Stains-All dye to visualize HA. Despite extensive washing after reaction of HA with aminated SPION or NW, there were still significant amounts of free HA associated with the particles **Figure 3-3a**, presumably due to electrostatic interactions of HA with the particles. After investigating multiple methods, we found that washing the HA-SPION samples with 10% ammonium sulfate followed by ultrafiltration through centrifugal filters (MWCO 100 kDa), free HA can be successfully removed as confirmed by gel electrophoresis. HA-NWs required higher concentrations of

ammonium sulfate (35%) to completely remove free HA possibly because of the stronger attraction of free HA with the longer NWs **Figure 3-3b**.

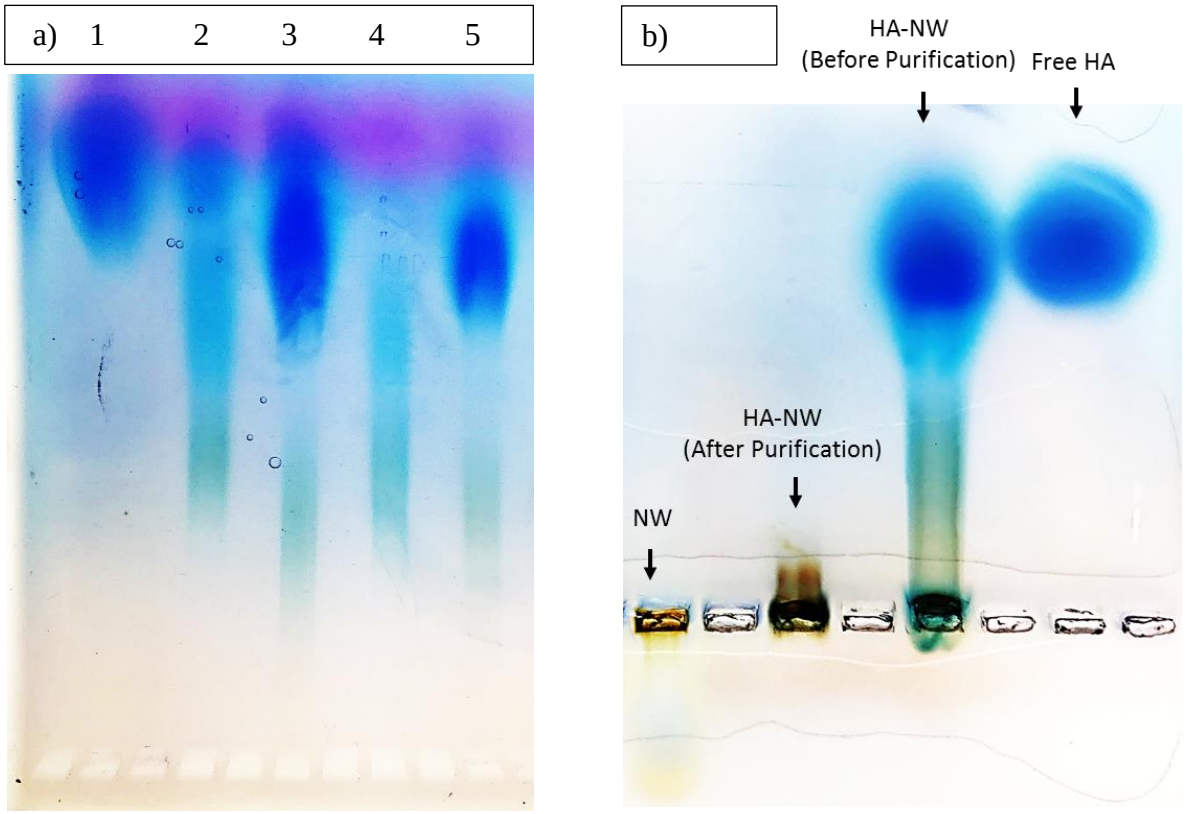

Figure 3-3. Removal of free HA from HA-SPIONs and HA-NWs. a) Lane 1 contains free HA. HA polymer showed blue color following staining with Stains-All dye. HA-SPION before and after washing with 10% $(NH_4)_2SO_4$ were placed in lanes 2 and 4 respectively. HA-NWs before and after washing with 10% $(NH_4)_2SO_4$ were in lanes 3and 5 respectively. b) Complete removal of free HA from HA-NWs by washing with 35% $(NH_4)_2SO_4$ was shown by gel electrophoresis. Purified HA-NW not only had no free HA but also moved towards the cathode on the gel while un-conjugated NWs did not move towards the cathode.

HA-NWs contaminated with free HA showed reduced binding with CD44 expressing cells, confirming the importance of completely removing free HA **Figure 3-4**. TGA analysis showed that for purified HA-NWs, the organic content accounted for 91% of the total weight, with 70% coming from HA **Figure 3-5**.

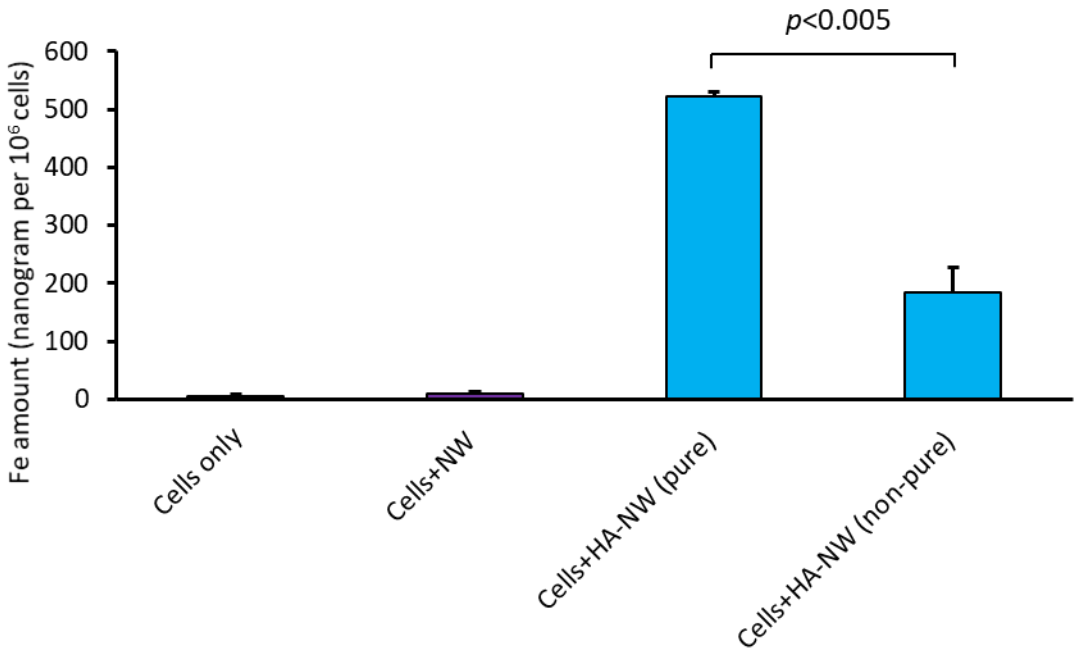

Figure 3-4. Free HA containing HA-NWs have reduced interactions with CD44 expressing cells compared to pure HA-NWs highlighting the importance of completely removing free HA following synthesis. CD44 expressing SKOV-3 cells were incubated with NWs, pure HA-NWs and non-pure HA-NWs. Intracellular Fe levels were quantified by ICP following removing unbound NWs.

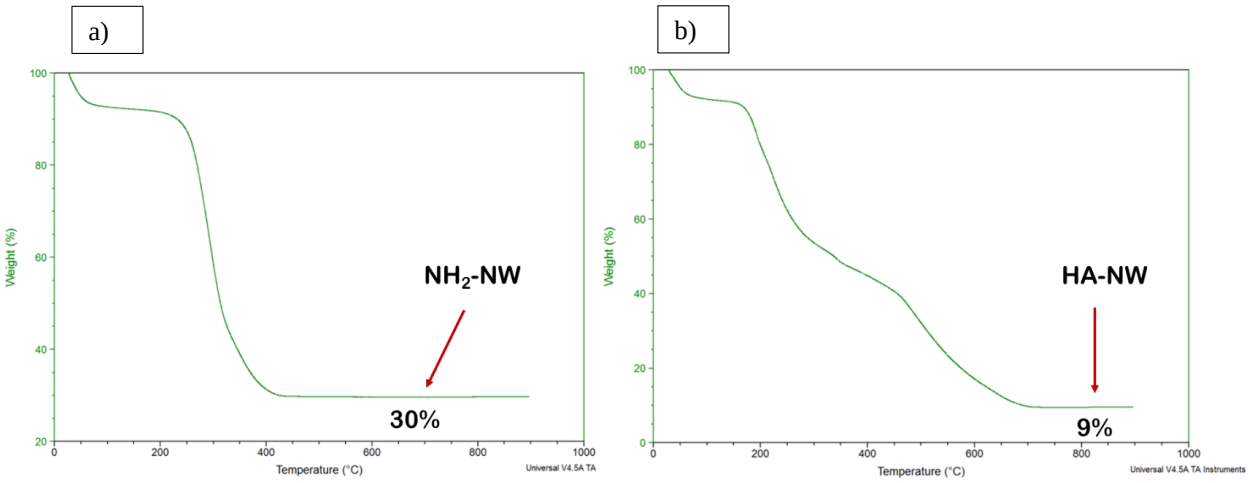

Figure 3-5. Thermogravimetric analysis (TGA) for (a) amine functionalized NWs and (b) HA conjugated NW.

3.3. Cellular Uptake of HA-NWs by CD44 Expressing Cells Is Much Higher than That of HA-SPIONs

With HA-SPIONs and HA-NWs in hand, their interactions with CD44 expressing vascular endothelial cells EA.hy926 **Figure 3-6**, macrophage RAW264.7 cells[24-25] and SKOV-3 cancer cells[26] were examined.

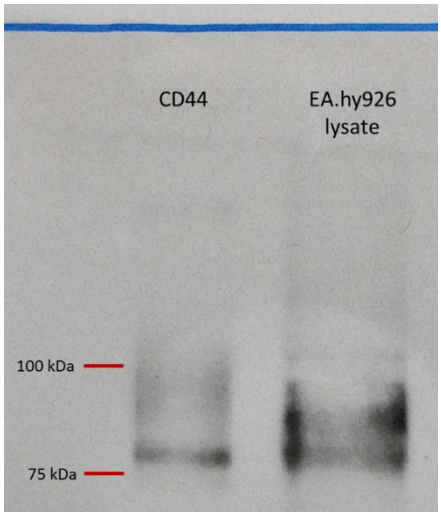

Figure 3-6. Western blotting showed the presence of CD44 in EA.hy926 cells.

FITC labeled HA-NWs and HA-SPIONs were incubated with cells at equal initial FITC emission intensities, which was followed by extensive wash to remove unbound particles. The cells were then imaged through confocal microscopy. As shown in **Figure 3-7b,f**, both HA-NWs and HA-SPIONs could be found inside cells as indicated by the intracellular green fluorescence upon incubation. There was extensive co-localization of the FITC green fluorescence with the red fluorescence color from lysotracker indicating the nanoprobes entered lysosomes of the cells **Figure 3-7d,h**. Cells treated with FITC-HA-NWs gave stronger FITC fluorescence intensities suggesting the uptake of HA-NWs was higher than that of HA-SPIONs **Figure 3-7b** vs **f**.

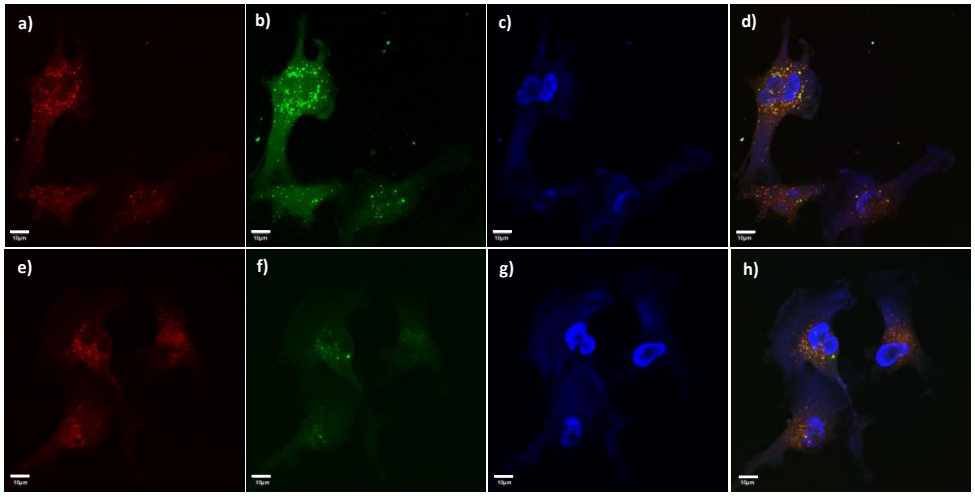

Figure 3-7. Confocal microscopy showed stronger interaction for HA-NWs (a-d) than the corresponding HA-SPIONs (e-h) with CD44 expressing cells such as vascular endothelial cells EA.hy926. (a,e) are red lysotracker channel showing locations of the lysosomes, (b,f) are FITC channel showing locations of the nanoprobes, (c,g) are DAPI channel showing location of nuclei, (d,h) are overlays of red lysotracker, green FITC and DAPI channels. Scale bars are 10 μm.

To better quantify cellular uptake, flow cytometry analysis was performed, which showed cells incubated with FITC-HA-NWs gave more than four times higher fluorescence than those treated

with FITC-HA-SPIONs **Figure 3-8a**. To further confirm higher cellular uptake of HA-NWs, the amounts of iron inside cells were quantified by inductively coupled plasma (ICP) analysis, which indicated significantly more iron in cells treated with HA-NWs than those with HA-SPIONs **Figure 3-8b**.

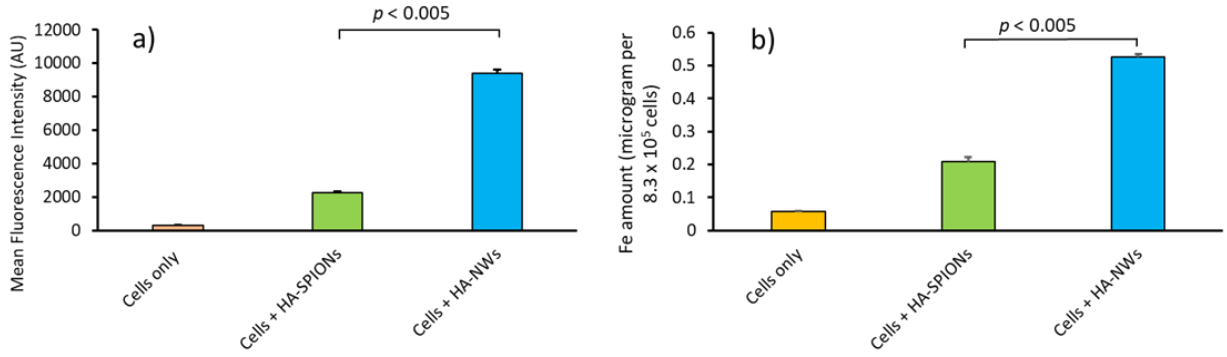

Figure 3-8. HA-NW uptake by CD44 expressing EA.hy926 cells is higher than the corresponding HA-SPIONs. a) Mean fluorescence intensities of EA.hy926 cells following incubations with HA-NWs and HA-SPIONs. b) Intracellular Fe content was quantified by ICP after incubations with HA-NWs and HA-SPIONs. The *p*-values were obtained from student's *t*-test.

3.4. Both CD44 and HA Are Important for HA-NW Interactions with Cells

To confirm CD44 dependence of cellular interactions with HA-NWs, anti-CD44 monoclonal antibody (mAb) MEM-85 (IgG2b subtype) was added during cellular incubation of HA-NWs. MEM-85 is known to bind with CD44 and competitively block its interactions with HA[27]. ICP quantification showed that MEM-85 led to 50% reduction of the intracellular level of iron, indicating that HA-NW uptake at least partially goes through CD44. A mouse IgG2b (PLPV219) not capable of binding CD44 was used as the isotype control mAb and intracellular iron quantification did not show reduction of HA-NW uptake when cells were co-incubated with PLPV219 and HA-NWs **Figure 3-9**.

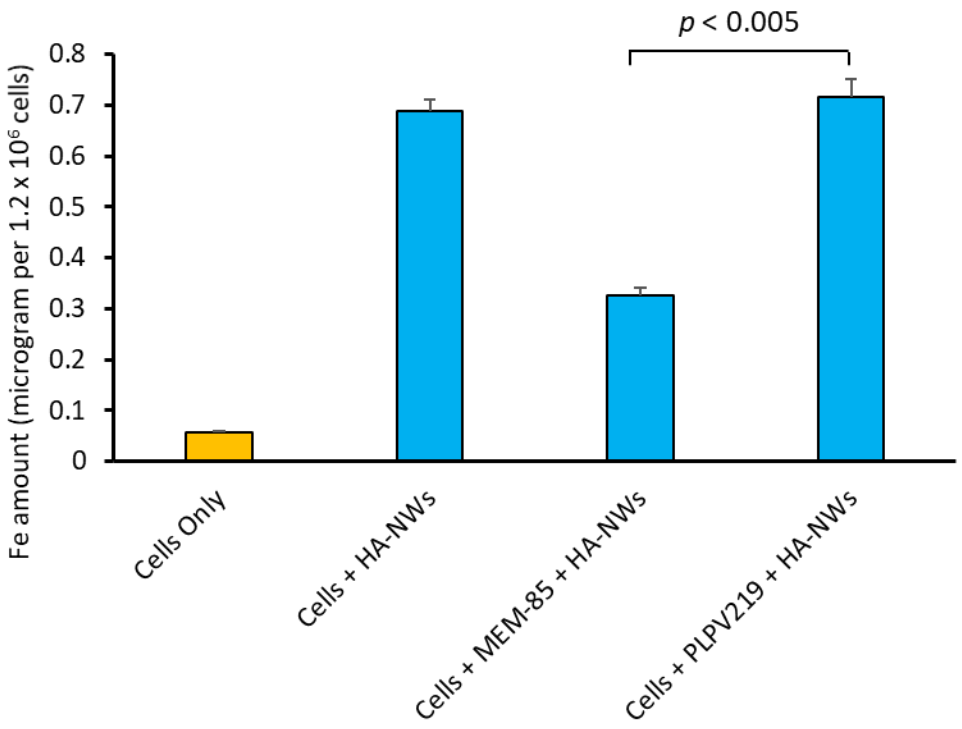

Figure 3-9. Pretreatment of cells with an anti-CD44 mAb MEM-85 resulted in 50% reduction of HA-NW cellular uptake, while the non-CD44 binding isotype control mAb PLPV219 did not have much effects on cellular uptake of HA-NWs. The *p*-value was obtained from student's *t*-test.

The cellular uptakes of HA-NWs were measured under variable conditions including changes in temperature, incubation time and incubation concentration. When cells were incubated with HA-NWs at 4 ºC, HA-NW uptakes were much lower than those at 37 ºC indicating the uptake process was energy dependent **Figure 3-10** [28-29].

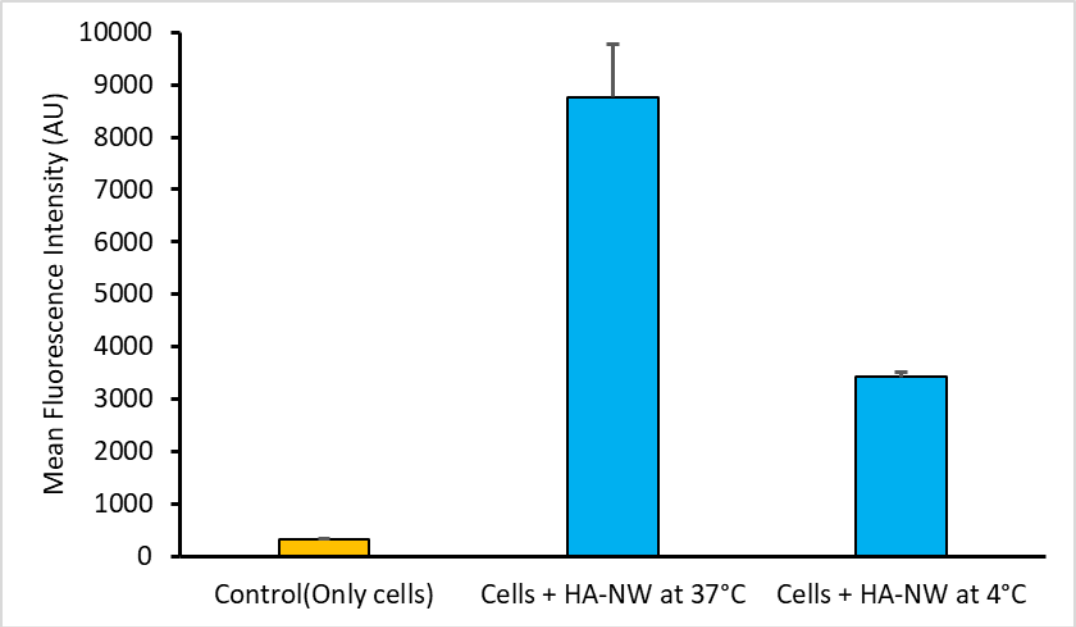

Figure 3-10. FACS study showed mean fluorescence intensities of SKOV-3 cells after incubation with HA-NWs in 37 ˚C and 4 ˚C respectively.

Incubation of HA-NWs with cells at various time intervals showed that the uptake reached the maximum levels after 2 hours of incubation **Figure 3-11**. Treatment of cells with varying amounts of HA-NWs revealed that cellular uptake of HA-NWs could be saturated above 200 µg Fe/mL **Figure 3-12**. These results are consistent with the idea that HA-NWs interact with cells through CD44 mediated endocytosis.

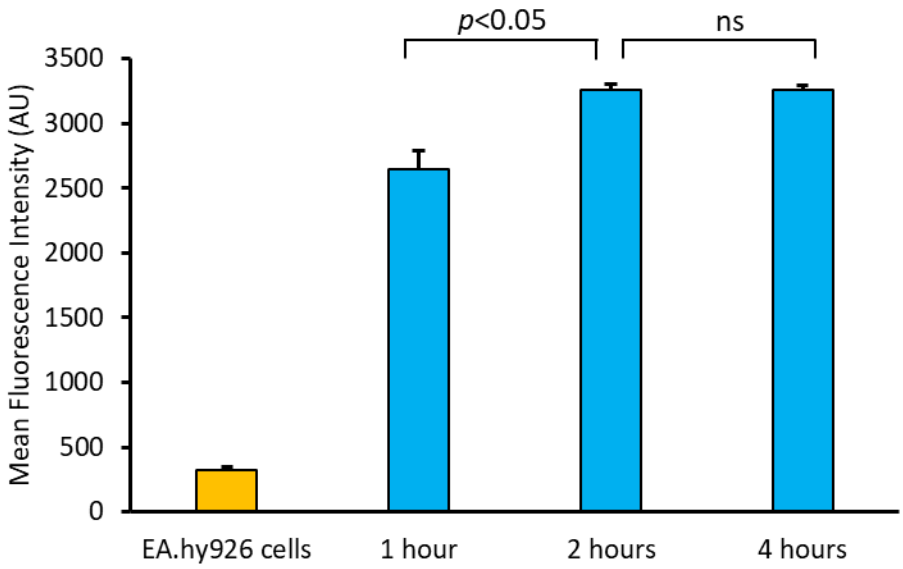

Figure 3-11. Monitoring EA.hy926 cellular uptake of HA-NW in different time intervals. 50 µg/mL HA-NWs were added to each well and MFI were measured by FACS. The *p*-values were obtained from student's *t*-test.

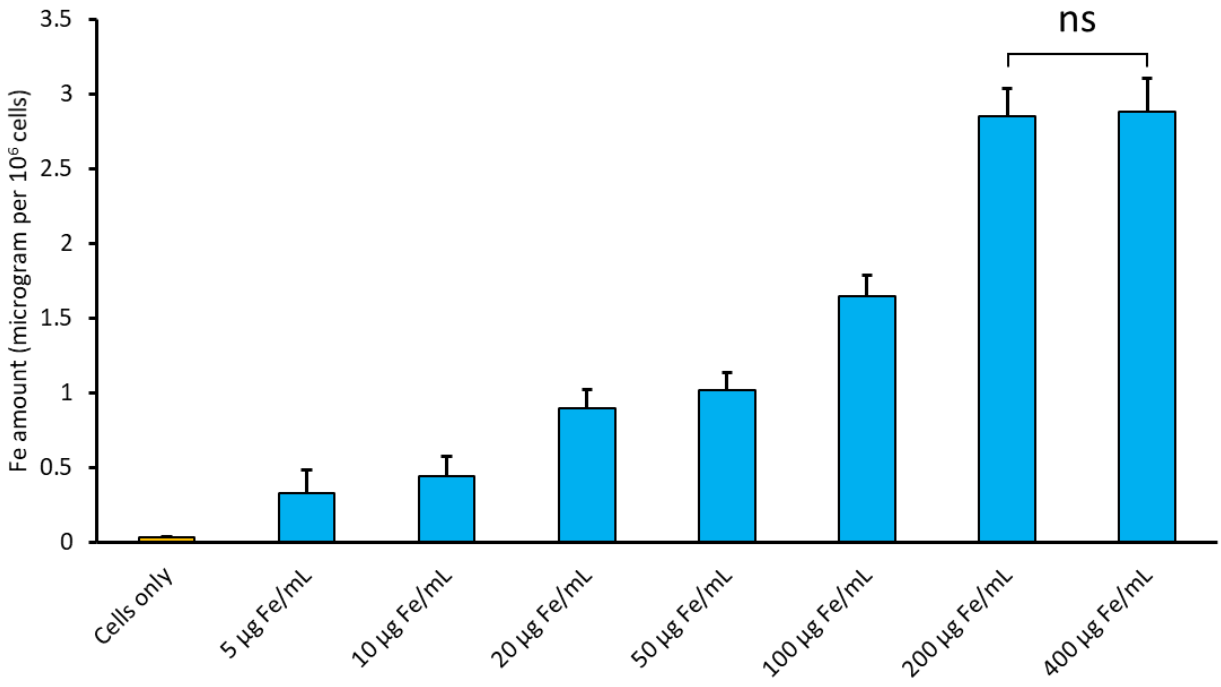

Figure 3-12. Incubation of SKOV-3 cells with different amounts of HA-NWs.

The importance of HA for cellular uptake was demonstrated by several experiments. Incubation of cells with FITC labeled NWs without HA (FITC-NWs) showed little cellular uptake or binding when analyzed by FACS **Figure 3-13a**. Treatment of cells with free HA (10 mg/mL) before addition of HA-NWs competitively inhibited cellular uptake of HA-NWs **Figure 3-13b**. Calculations showed that 140 times higher amount of free HA was needed to reduce the binding of HA-NW by 90% indicating the multivalent properties of HA-NWs leading to higher avidity binding between CD44 and HA.

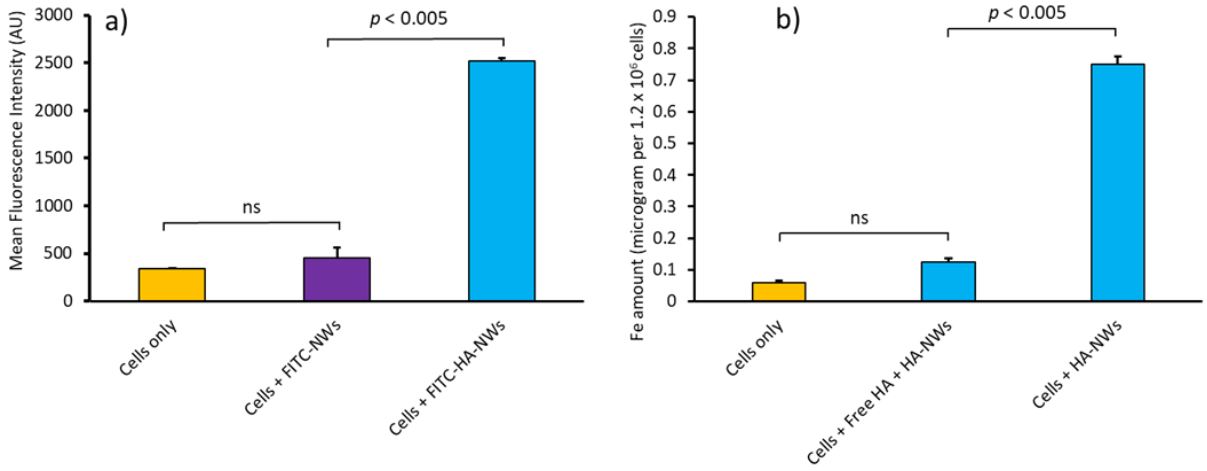

Figure 3-13. Presence of HA on HA-NWs was necessary for their cellular interactions with cells. a) cells were treated with equivalent amounts of NWs and HA-NWs and analyzed by FACS b) Pre-treatment of cells with free HA significantly reduced cellular interactions with HA-NWs. The *p*-values were obtained from student's *t*-test.

3.5. HA-NW Induced Much Lower Inflammatory Response than HA-SPIONs to Macrophages

For *in vivo* applications of nanoprobes, it is important that the probes are highly biocompatible. HA-NWs and HA-SPIONs were incubated with CD44 expressing mouse macrophage RAW264.7 cells[24-25] and the levels of proinflammatory cytokines induced were quantified by real-time

polymerase chain reaction (RT-PCR). Cytokines such as IL-1α, IL-1β,[30-31] TNFα,[32-35] and MCP-1 are inflammatory, which increase vascular permeability[36-37] and recruit inflammatory cells to plaques.[38] Spp can induce migration of macrophages to the sites of inflammation.[39] As shown in Figure 6, the levels of IL-1α expression in macrophages incubated with HA-NWs were less than 5% of those incubated with HA-SPIONs. In addition, cells treated with HA-NWs had significantly lower levels of other cytokines tested including IL-1β, MCP-1, TNF-α, and Spp **Figure 3-14a**. In addition, inflammatory responses to HA-NWs vs HA-SPIONS were evaluated *in vivo*, by examining TNFα and IL-1β levels in mouse blood 1 and 24 hours after injection. Although TNFα level was not detectable in the blood before injection of HA nanoparticles, it increased 1 hour following injection and the TNFα level was 10 times higher in mice receiving HA-SPIONs vs those administered with HA-NWs indicating higher inflammatory responses to HA-SPIONs **Figure 3-14b**. TNFα level was not detectable 24 hours after injection of both HA nanoparticles possibly due to feedback mechanisms that decrease TNFα production. IL-1β was not detectable in mice blood before injection, 1 and 24 hours after injection of HA nanoparticles (data not shown). Collectively, these results suggest the superior bio-compatibilities of HA-NWs compared to HA-SPIONs.

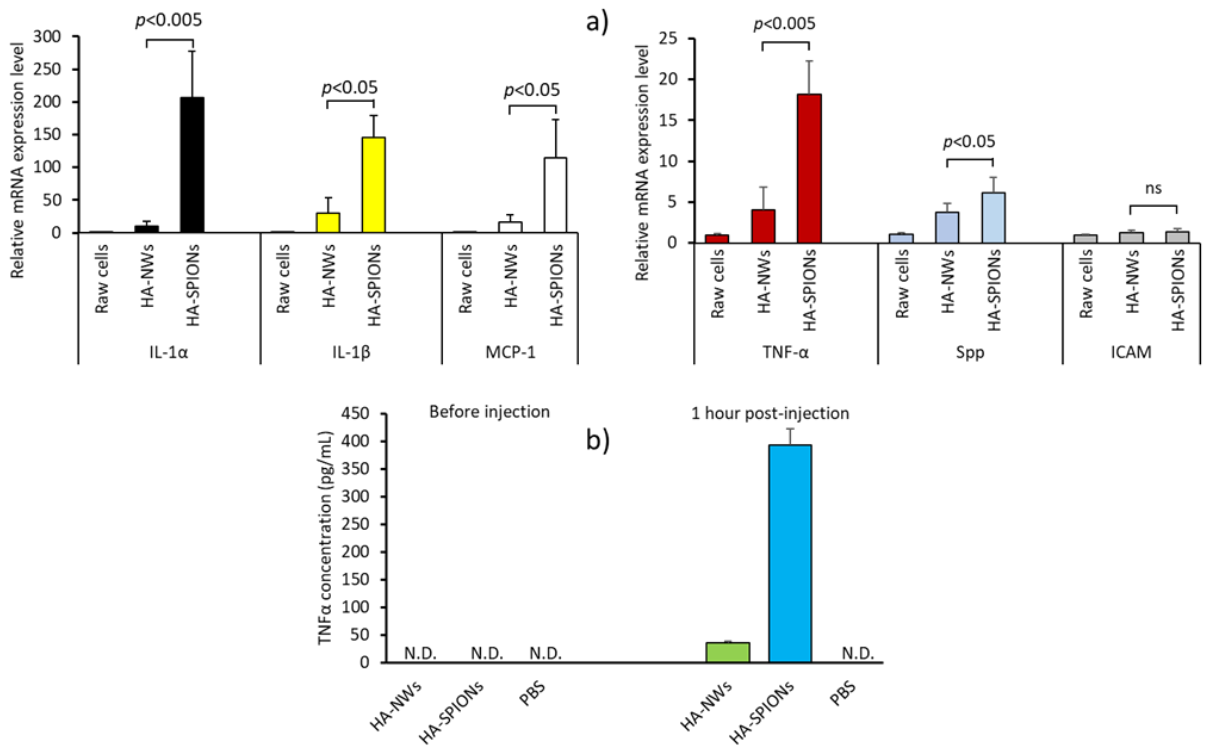

Figure 3-14. Inflammatory response to HA nanoparticles. a) Expression levels of inflammatory genes after interaction of RAW264.7 cells with equivalent amounts of HA-SPIONs and HA-NWs. HA-NWs induced significantly less inflammatory cytokines compared to HA-SPIONs. b) TNFα levels in blood from mice before and after injection of HA nanoparticles. HA-SPIONs induced higher level of TNFα 1 hour after injection compared to HA-NWs. N.D.: not detected.

3.6. HA-NWs Were Nontoxic to Cells and to Mice at the Concentrations Used for Imaging

To further test the biocompatibility of HA-NWs, cell viability assay was performed. Vascular endothelial EA.hy926 cells were incubated with HA-NWs and cell viabilities were determined by the MTS assay. No detrimental effects on cell viability were observed following incubation of HA-NWs up to 1 mg/mL **Figure 3-15**.

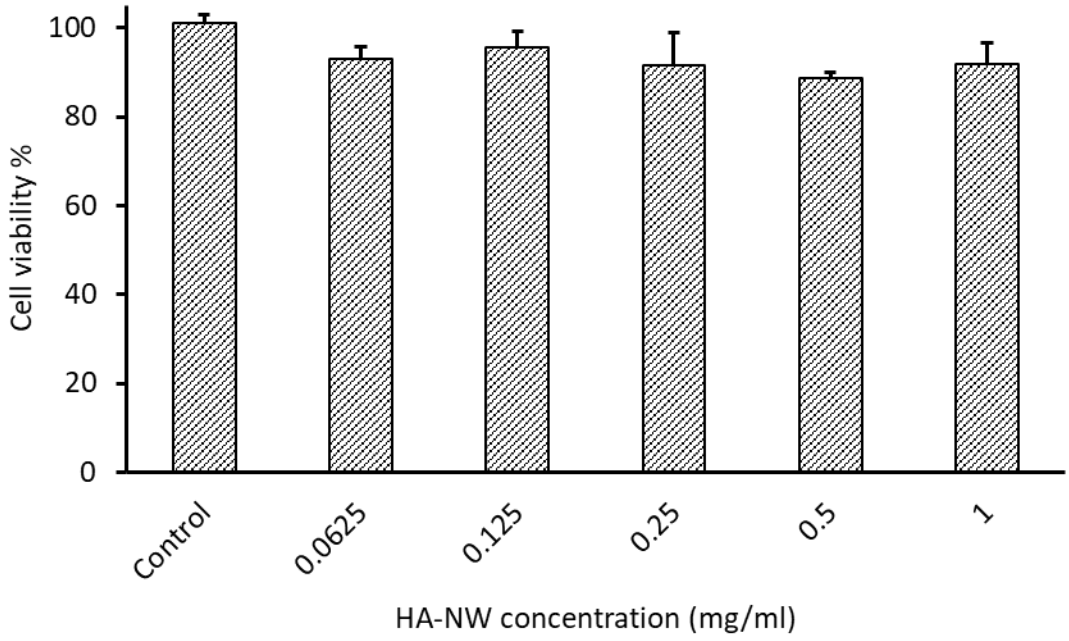

Figure 3-15. EA.hy926 cell viabilities following incubation with different concentrations of HA-NWs were measured by the MTS assay. No reductions of cell viability were observed.

To evaluate their biocompatibility *in vivo*, HA-NWs were injected into mice. One day after injection, blood was drawn from mice and a complete comprehensive blood chemistry panel analysis was performed. All the parameters evaluated were in normal range **Table 3-1**. Most noteworthy were the negligible changes in alkaline phosphatase, aspartate aminotransferase, alanine transaminase and gamma-glutamyl transferase levels (markers for liver function) and total protein concentration (globulin and albumin) together with bilirubin level suggesting negligible acute toxicities. In addition, histopathological analysis did not show any signs of toxicity on liver, lung or kidney after HA-NW administration **Figure 3-16**.

Table 3-1. Results for blood chemistry panel analysis 24 h after injection of HA-NWs.

	Values	Reference Values
Total Protein	5.6 g/dL	4.5-6.5 g/dL
Albumin	2.7 g/dL	2.4-3 g/dL
Globulin	2.9 g/dL	1.8-3 g/dL
Total bilirubin	0.9 mg/dL	0-1.0 mg/dL
Direct bilirubin	0.0 mg/dL	
Indirect bilirubin	0.9 mg/dL	
ALP U/L	27	15-45
GGT U/L	<3	0-9
ALT U/L	30	10-35
AST U/L	278	43-397

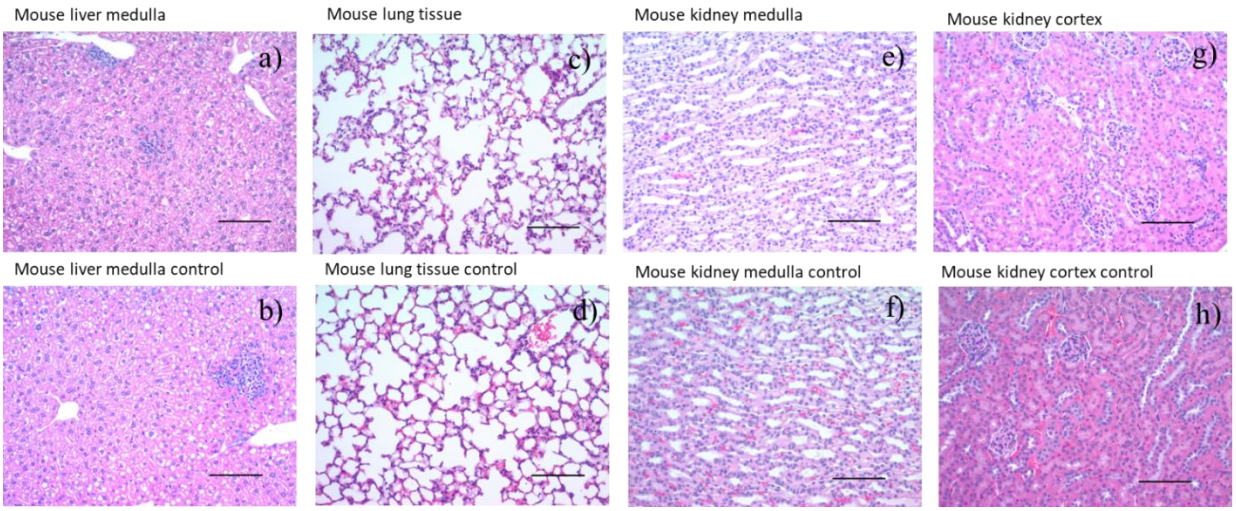

Figure 3-16. Histopathology images of extracted organs 24 hours after HA-NW administration. (a) is mouse liver medulla; (c) is mouse lung tissue; (e) is mouse kidney medulla and (g) is mouse kidney cortex 24 hours after HA-NW injection. (b) is mouse liver medulla; (d) is mouse lung tissue; (f) is mouse kidney medulla and (h) is mouse kidney cortex images for control mouse. Scale bar is 100 micrometers.

3.7. HA-NWs Enabled In Vivo Imaging of Atherosclerosis Plaques in ApoE Knockout Mice

With the strong binding of HA-NWs to CD44 expressing cells and their biocompatibility demonstrated, we next examined the utility of HA-NWs for atherosclerotic plaque detection in ApoE knockout mice. Compared to the rabbit model which utilizes balloon catheter de-endothelization surgical procedure of rabbit aorta to induce injury and initiate atherosclerosis development[40], ApoE knockout mice are attractive as they closely mimic human conditions by spontaneously developing human like atherosclerotic plaques without the need for surgery[41-43].

ApoE knockout mice were injected with HA-NWs retro-orbitally and the mice were subjected to serial MRI using a T_2* weighted imaging protocol focusing on the abdominal aorta area. Upon

administration of HA-NWs (8 mg Fe/Kg body weight), the image intensities of the lumen significantly decreased due to the loss of signals induced by HA-NWs **Figure 3-17**. The lumen signal levels returned to pre-injection levels within 80 minutes suggesting the majority of HA-NWs were cleared from the blood pool by that time. On aorta walls, the signal intensities of selective areas decreased to 20% of pre-injection levels 20 minutes after injection presumably due to binding of HA-NWs and these signal intensities remained at ~20% of pre-injection levels for more than 120 minutes **Figure 3-18**.

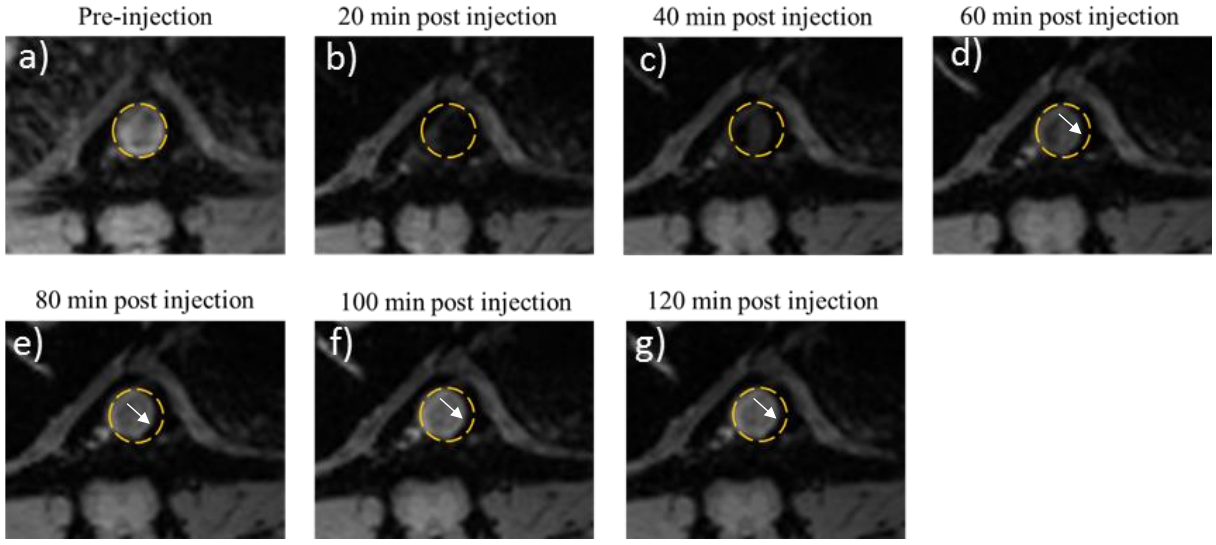

Figure 3-17. T_2* weighted MR images of ApoE knockout mice aorta (a) before injection of HA-NWs (8 mg Fe/Kg body weight) and different time intervals after injection of HA-NWs (b-g). Areas of the aorta walls undergone contrast changes are highlighted by white arrows.

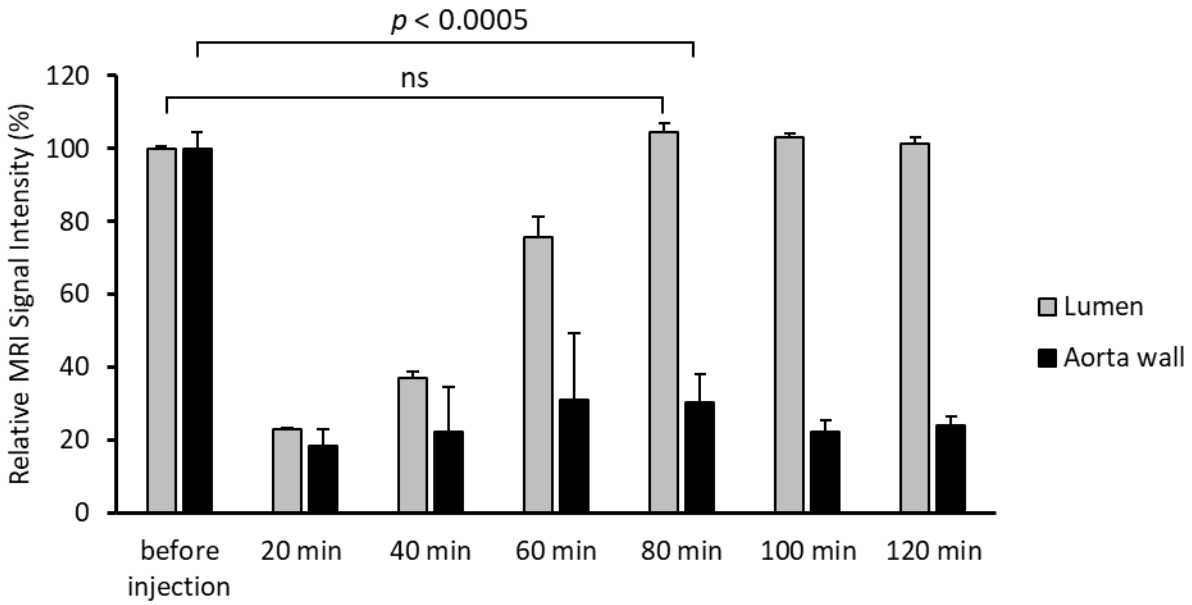

Figure 3-18. Quantification of signal intensity change for lumen and aorta wall before injection and at different time intervals after injection of HA-NWs. The *p*-value was obtained from student's *t*-test.

The signal changes could be observed in multiple locations of the aorta of ApoE knockout mice and the signals of the vessel walls fully recovered after one week **Figure 3-19**, **Figure 3-20**, **Figure 3-21** and **Figure 3-22**. Furthermore, even with a low dose of 2.8 mg Fe/Kg of HA-NWs, effective plaque imaging could still be achieved **Figure 3-20**.

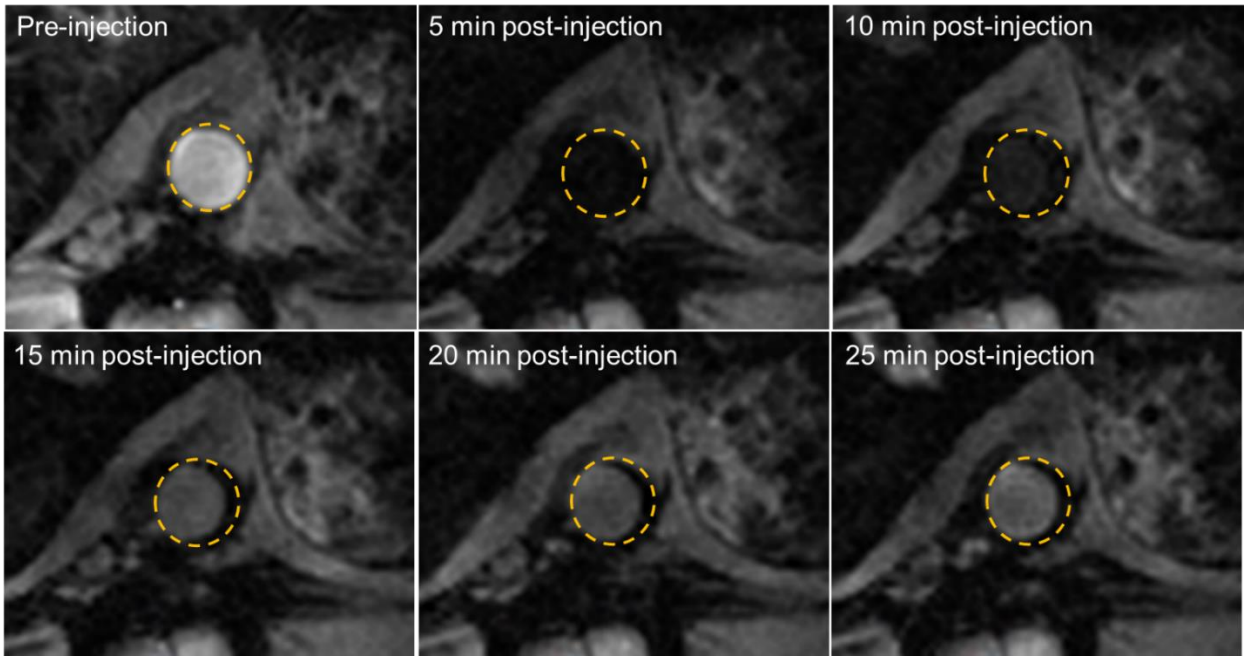

Figure 3-19. MRI contrast changes of the aorta of ApoE knockout mice upon injection of HA-NWs (4 mg/Kg).

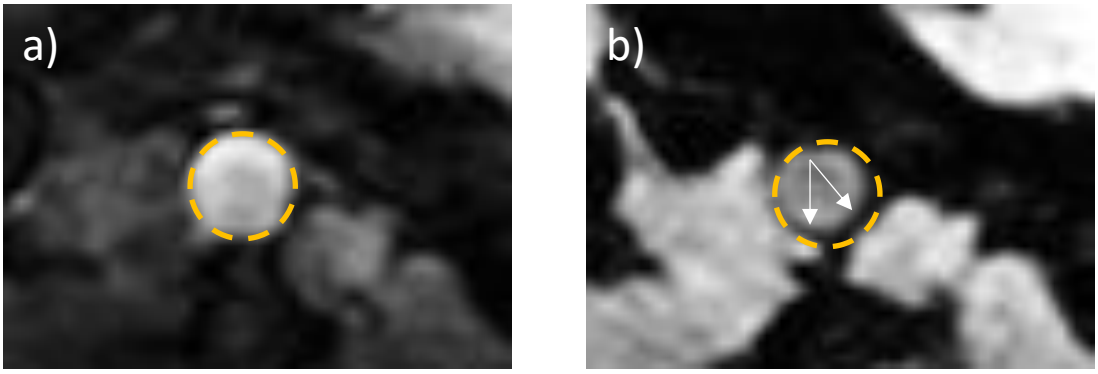

Figure 3-20. MRI contrast changes of the aorta of ApoE knockout mice a) before and b) 20 minutes after injection of HA-NWs (2.8 mg/Kg).

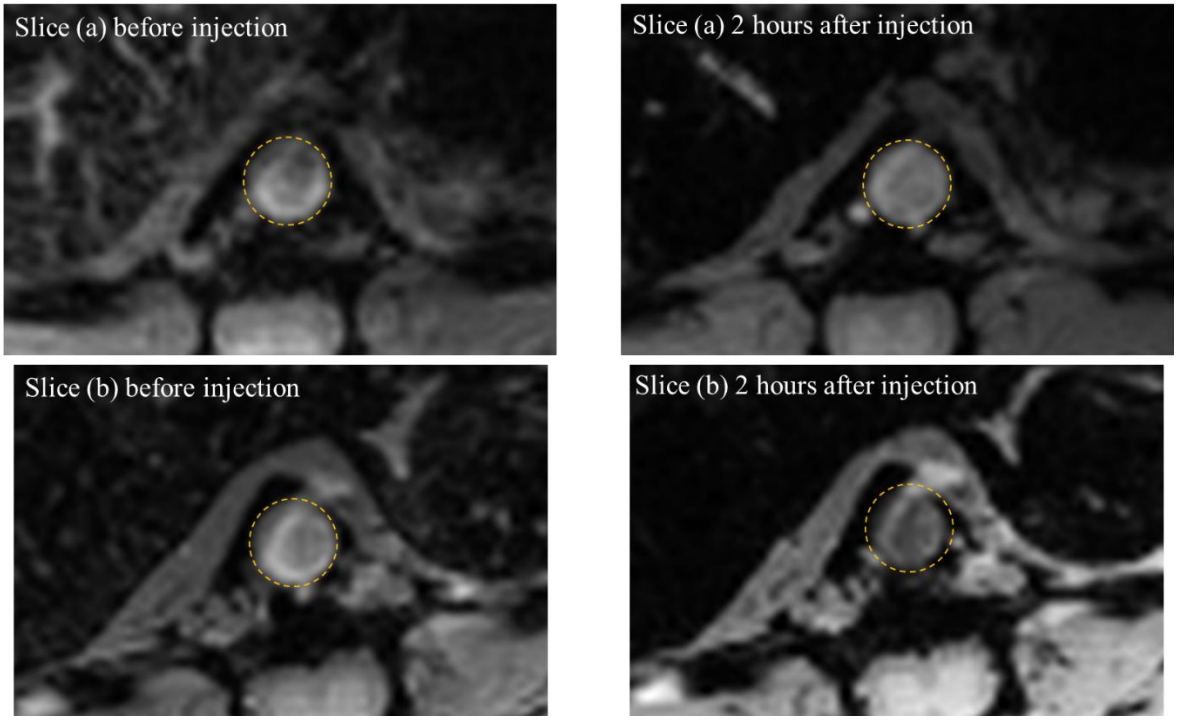

Figure 3-21. Analysis of MRI of different slices of the aorta of ApoE knockout mice showed signal loss on the aorta wall in some locations but not all of them; indicating HA-NWs only interacted with selective areas of aorta wall that were presumably atherosclerosis plaques.

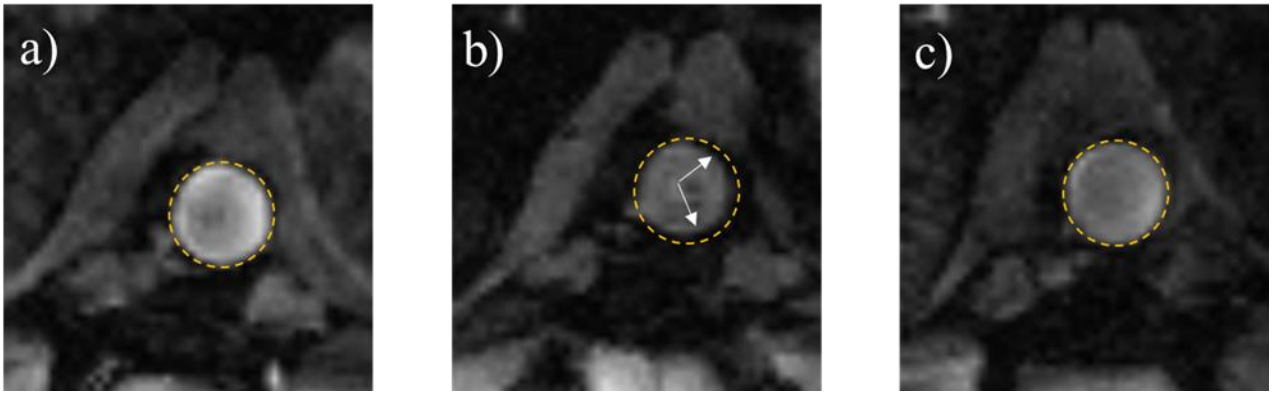

Figure 3-22. The signal intensity changes of the aorta lumen disappeared when ApoE knockout mouse was scanned one week after HA-NW administration. (a) ApoE knockout mouse aorta

Figure 3-22 (cont'd) before injection, (b) ApoE knockout mouse aorta 0.5 hour after injection and (c) ApoE mouse aorta image one week after injection of HA-NWs.

To ascertain signal changes were caused by HA-NW binding to atherosclerotic plaques in ApoE knockout mice, several control imaging experiments were performed. Following identical protocol as HA-NWs, NWs without HA were injected into ApoE knockout mice at the same Fe concentration and T_2* weighted MRI were performed. No signal losses were observed from aorta wall of these mice **Figure 3-23b**. In addition, when free HA was co-injected with HA-NWs to ApoE knockout mice, little signal changes were found from aorta walls possibly because free HA competed with HA-NWs for binding with CD44 rich plaques **Figure 3-23c**. These results confirmed the importance of HA for plaque detection *in vivo*.

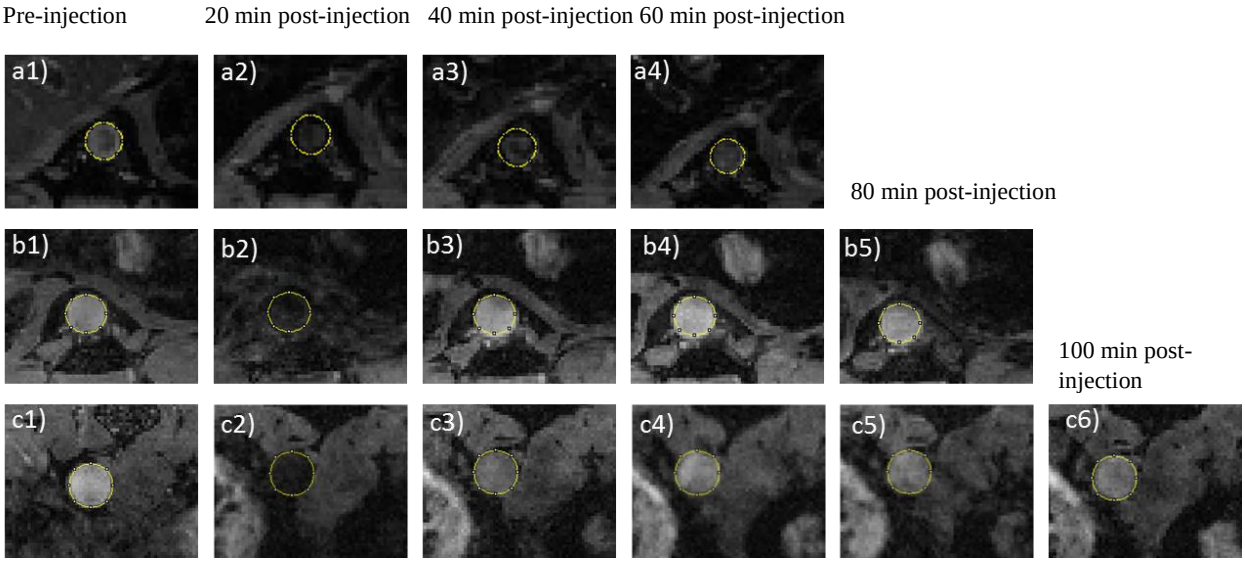

Figure 3-23. a) HA-NWs were injected to the wild type mouse and the abdominal aorta was scanned before (a1) and different time intervals after injection (a2-4). b) NWs were injected to the ApoE knockout mouse and the abdominal aorta was scanned before (b1) and different time intervals after injection (b2-5). c) HA-NWs were mixed with free HA and injected to ApoE

Figure 3-23 (cont'd) knockout mouse and the abdominal aorta was imaged before (c1) and different time intervals after injection (c2-6).

Another control experiment was performed by administering HA-NWs to wild type mice followed by MRI **Figure 3-23a**. These mice did not have atherosclerosis and their aorta walls did not exhibit significant changes in T_2* weighted MRI after HA-NW injection. This suggests signal changes found in ApoE knockout mice caused by HA-NWs were not due to non-specific binding of HA-NWs to mouse aorta walls.

While HA-SPIONs can induce higher levels of inflammatory cytokines such as TNF-α *in vivo*, their abilities to aid in plaque imaging were tested. HA-SPIONs (8 mg Fe/kg) were injected to ApoE knockout mice and their aortae were scanned following the identical T_2* weighted MRI protocols as those receiving HA-NWs discussed above. As expected, upon HA-SPION administration, the lumen of aorta turned black in T_2* weighted images suggesting HA-SPIONs entered the blood causing significant MR signal losses **Figure 3-24** and **Figure 3-25**. Interestingly, the signal intensities of lumen in these mice did not recover even 140 minutes after injection, which prevented the detection of plaques on aorta walls due to a lack of MR contrasts between the lumen and aorta walls. This was a stark difference from mice receiving HA-NWs **Figure 3-17** and **Figure 3-24**, where lumen signals returned to pre-injection levels within 80 minutes after injection presumably due to higher cellular uptake of HA-NWs compared to HA-SPIONs. These results indicate that HA-NWs are not only more biocompatible, but also more superior imaging agents.

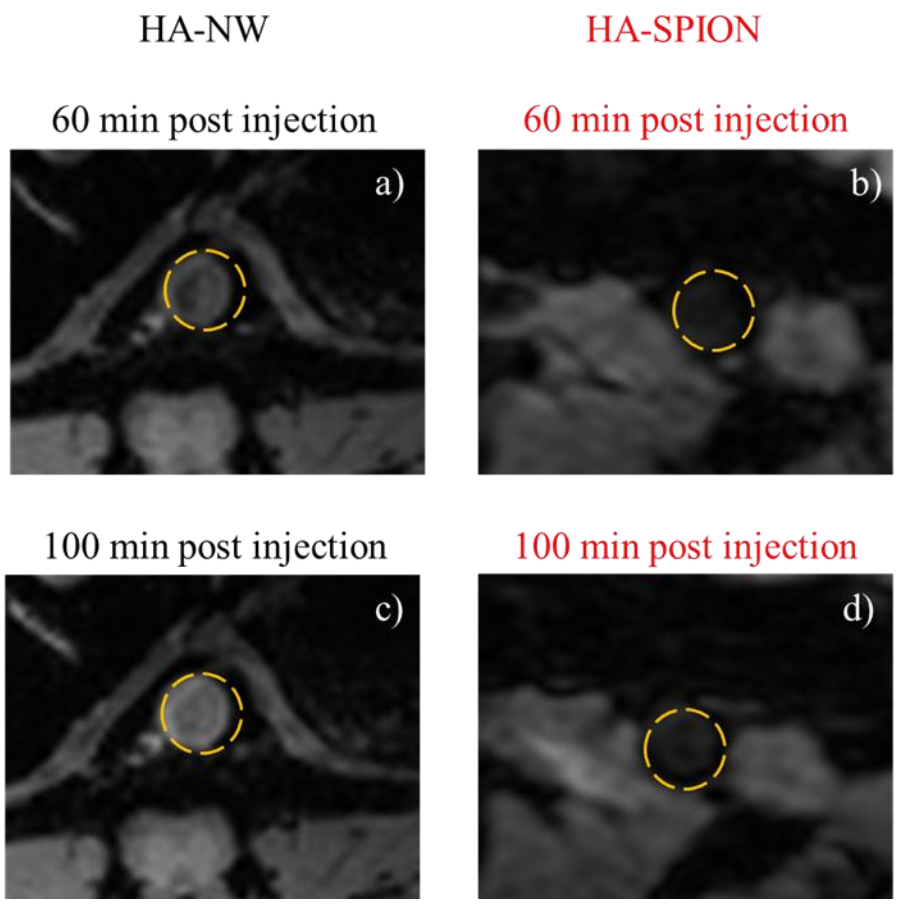

Figure 3-24. Comparison of HA-SPIONs (8 mg Fe/kg) and HA-NWs (8 mg Fe/kg) for MRI detection of atherosclerotic plaques in ApoE knockout mice. Aorta lumen MR signals recovered partially (panel a) and completely (panel c) 60 minutes and 100 minutes after injection of HA-NW enabling the detection of plaques on aorta walls. In contrast, aorta lumen signals did not recover 60 and 100 minutes after injection in mice receiving HA-SPIONs (panels b and d), preventing plaque detection at these time points.

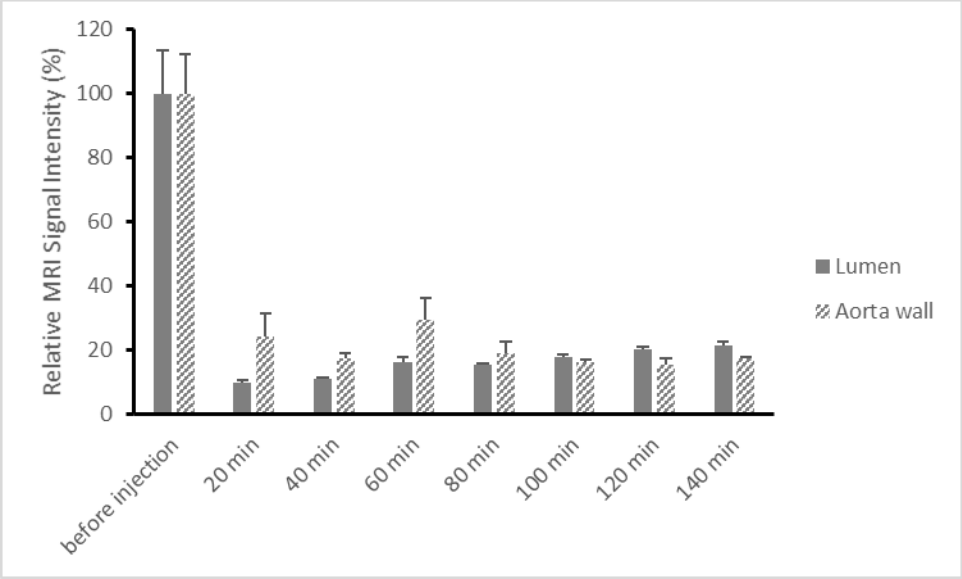

Figure 3-25. Quantification of signal intensity change for lumen and aorta wall before injection and at different time intervals after injection of HA-SPIONs (8 mg Fe/kg). Analysis was performed using ImageJ software. Lumen signals did not recover much 140 minutes after HA-SPION injection.

3.8. Histological Analysis

F4/80 staining of abdominal aorta in ApoE knockout mouse showed accumulation of macrophages in abdominal aorta wall at the same locations where MRI signal changes were observed **Figure 3-26a, b.** The same stain did not show macrophages accumulation in the wild type control mouse aorta **Figure 3-26c, d**. Prussian blue staining of ApoE knockout mouse aorta after incubation with HA-NWs showed the presence of iron in lumen wall indicating binding of HA-NWs with CD44 expressing cells present in lumen wall **Figure 3-26e** vs **f**. In addition, aorta tissues incubated with HA-NWs displayed more intense Prussian blue staining than those with HA-SPIONs **Figure 3-27**, which was consistent with in vitro cellular studies suggesting stronger binding of HA-NW with plaque residing cells.

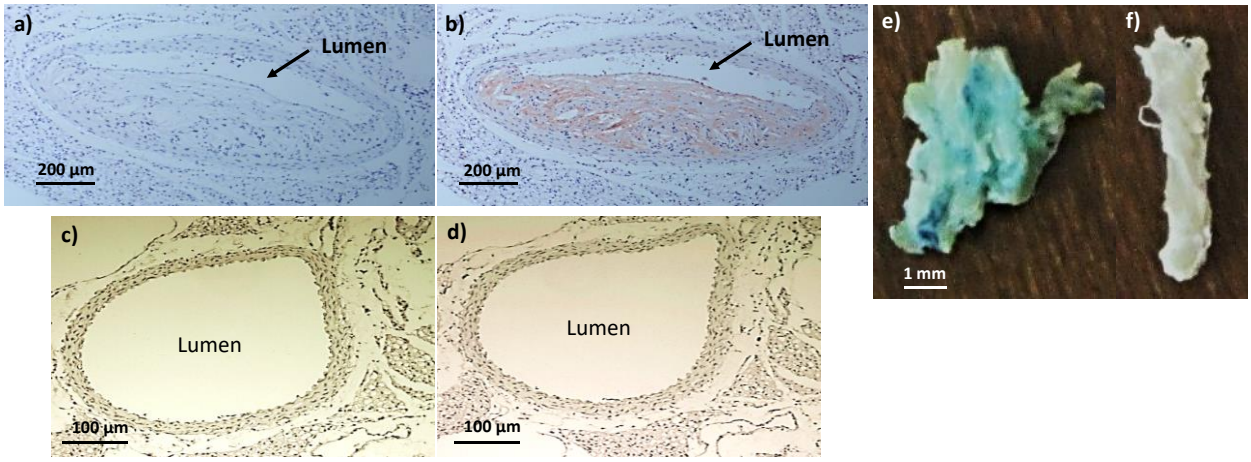

Figure 3-26. F4/80 staining showed macrophage accumulation in ApoE knockout mouse aorta. (a) and (b) are ApoE knockout mouse aorta slice before and after F4/80 staining. (c) and (d) are wild type mouse aorta slice before and after F4/80 staining. Prussian blue staining of (e) ApoE knockout mouse and (f) wild type aorta after incubation with HA-NWs. The staining (blue green color) was much more intense in panel e than f.

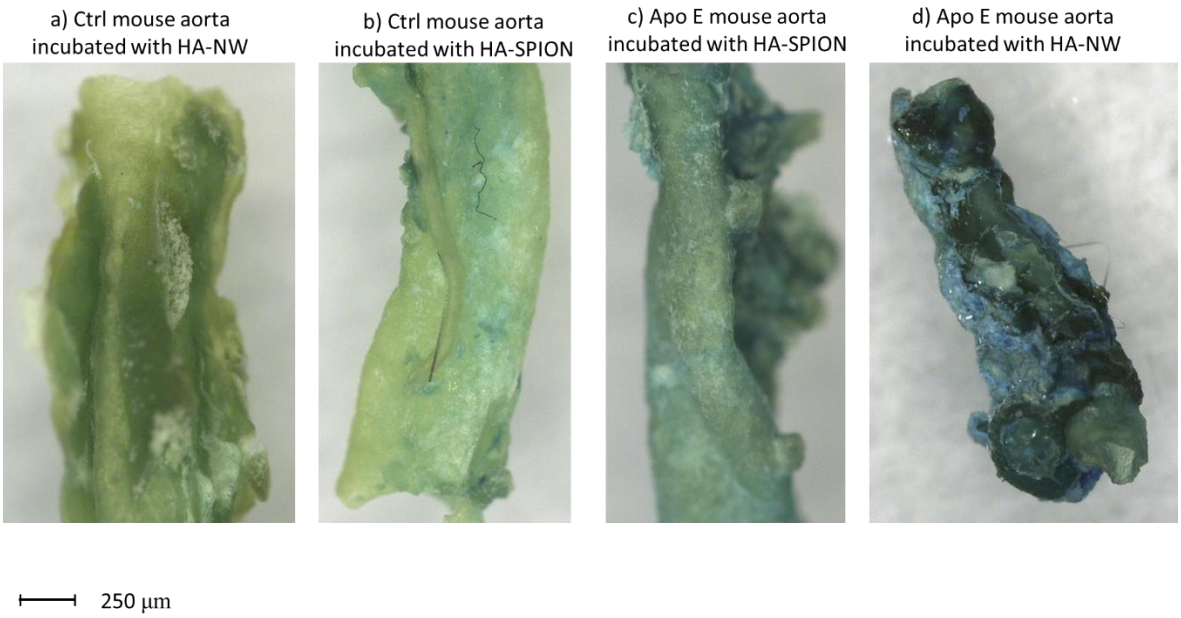

Figure 3-27. Comparison of Prussian blue staining of aortae after incubations with identical concentrations of HA-NWs or HA-SPIONs (0.4 mg Fe/kg) for 1 hour at 37 °C. a) aorta from wild

Figure 3-27 (cont'd) type control mice stained with HA-NWs; b) aorta from wild type control mice stained with HASPIONs; c) aorta from ApoE knockout atherosclerotic mice stained with HA-SPIONs; d) aorta from atherosclerotic mice stained with HA-NWs. The much higher intensities of Prussian blue staining in panel d) compared to all other panels suggest the stronger binding of plaque tissues by HA-NWs.

3.9. Discussion

SPIONs have been generally considered biocompatible[44-45]. However, they can impair iron homeostasis in cells, resulting in inflammation, or other adverse effects[46-47]. While HA can reduce inflammatory activities, to further enhance the biocompatibilities and cellular binding, we have synthesized HA-NWs, which have elongated shape vs the spherical HA-SPIONs.

The size and shape of nanomaterials can impact cellular uptake and inflammatory responses[48-50]. Chen and coworkers synthesized polymer nanoparticles with either spherical or cylindrical shapes, which were then functionalized with mannose to yield glyconanoparticles[51]. Cellular uptake experiments with RAW264.7 cells showed that spherical glyconanoparticles were taken up much more than cylindrical particles. The longer cylindrical glyconanoparticles induced higher inflammatory responses (IL-6) than shorter or spherical ones. The Chan group found that Hela cells internalized more spherical gold nanoparticles (AuNPs) than rod-shaped AuNPs[52]. Smaller spherical polymeric micelles were taken up by cells more than analogous cylindrical micelles[53]. Thiolated poly(methacrylic acid) capsules with different morphologies could influence cytokine secretion by macrophages: short rod-shaped capsules stimulated the generation of higher levels of TNF-α and IL-8 compared with spherical or long rod-shape capsules[54].

In contrast, a series of other studies showed higher uptake of rod like particles vs spherical ones. Sailor group demonstrated that NWs coated with tumor targeting peptide accumulated in tumor tissues *in vivo* twice as much as the spherical particles bearing the same ligand[23, 55]. When spherical Au-NPs and Au nanorods coated with West Nile virus envelope were incubated with cells, 6 times more nanorods were found internalized than the corresponding spherical Au NPs[56]. Yet, the Au-NPs induced higher amounts of inflammatory cytokines such as TNF-α compared to the nanorods. The divergent impact of size and shape on cellular interactions could be affected by factors including 1) pathways for endocytosis[51]; 2) shape dependent membrane wrapping time required to engulf the nanomaterials[53]; and 3) receptor density and rates of receptor endocytosis.

In our studies, despite similar surface charges, HA-NWs induced much lower inflammatory response compared to spherical HA-SPIONs, while the cellular uptake of HA-NWs was significantly higher **Figure 3-7**, **Figure 3-8** and **Figure 3-14**. HA-NWs interacted with CD44 expressing cells in a CD44 and HA dependent fashion as demonstrated in anti-CD44 mAb blocking and HA competition experiments **Figure 3-9** and **Figure 3-13**. The higher cellular uptake of HA-NWs can be explained by molecular weight dependence of HA-CD44 interactions. HA exists in nature as a homopolymer of disaccharides of D-glucuronic acid β-1,4 linked with D-glucosamine. While CD44 can bind with HA as short as a hexasaccharide, the binding affinity can significantly increase with higher molecular weight of HA[57-59]. The NWs can provide a multivalent platform to present a large number of HA molecules on the surface leading to high avidity with the CD44 receptor. This is supported by our observation that 140 times more free HA is needed to reduce the binding of HA-NW by 90% **Figure 3-13**. Compared to the corresponding HA-SPIONs, HA-NWs have elongated shapes. As a result, one HA-NW can possibly simultaneously engage a larger number of CD44 receptors on cell surface leading to stronger binding to cells.

The biological activities of HA are dependent upon its molecular weight[60]. Low molecular weight HAs can be inflammatory, while the high molecular weight HAs (million Daltons) are anti-inflammatory[60-61]. As one NW consists of multiple SPIONs and contains more HA per particle, it is possible that HA-NWs can better mimic high molecular weight HA, more effectively reducing the inflammatory activities resulting from the iron oxide core of the nanoprobes.

Due to the severe adverse effects of atherosclerosis on public health, there are high interests in developing imaging methods to detect the atherosclerotic plaques. MRI is a powerful technique for morphological imaging of blood vessels[6-7]. To better characterize plaques, contrast agents that can aid in the depiction of molecular process signatures other than plaque morphology are highly desired[8-9]. SPIONs are a popular class of contrast agents[39, 62-63] which lead to reduction of MR signals in T_2 and T_2* weighted images creating contrast from the surroundings. Earlier imaging studies using SPIONs take advantage of the non-specific uptake of the NPs by macrophages[64-67]. As a result, high concentrations of SPIONs (typical dose 56 mg Fe/Kg) need to be administered, which produce complete signal losses in lumen of the blood vessels[64-68]. In order to obtain sufficient contrast between plaques and lumen and allow sufficient clearance of NPs from the blood pool and the background, imaging was commonly performed at least one day and optimally 4 to 5 days after injection[64-67, 69]. In addition, longitudinal monitoring of plaque development will require regular administration of the nanoprobes. The need for prolonged delay of MRI after probe administration coupled with the possible inflammatory activities of SPIONs raise cautions for wide applications of these particles.

To improve on the performance of SPIONs and to provide information on the molecular composition and/or the state of the plaque, various targeting ligands have been immobilized onto SPIONs[70-76], which include peptide binders and mAbs for vascular cell adhesion molecule-1

(VCAM-1) and annexin V for apoptotic cells. Some of these probes have been employed to evaluate plaques *in vivo*. However, in many of these studies, high concentrations of NPs and/or prolonged delay after injection were still necessary for imaging.

In our work, we selectively target CD44, which is a receptor highly expressed in multiple plaque residing cells including endothelial cells, macrophages, and monocytes[10, 12-15, 77]. A significant advantage using HA-NWs is that plaque detection and imaging can be performed right after probe injection. This is probably due to two reasons: 1) with the strong binding to CD44 and the high magnetic relaxivities of HA-NWs, relatively small amounts of HA-NW (2.8 mg Fe/Kg) are needed to visualize the plaques in mice. As a result, the lumen of the blood vessels appeared grey rather than black in T_2* weighted MRI, allowing the distinction between lumen and the black plaque site even right after injection; 2) because CD44 is present on endothelial cells at the surface of the plaque tissues, HA-NW could rapidly bind with CD44 without the need to wait for particle penetrations into the tissues.

3.10. Conclusion

In conclusion, we have synthesized HA conjugated NWs for the first time. HA-NWs can interact more strongly than the corresponding spherical shaped HA-SPIONs with CD44 expressing cells in CD44- and HA- dependent manners. Furthermore, the inflammatory activities were significantly attenuated in HA-NWs suggesting engineering of nanomaterial shape and morphology can be a promising future direction to develop probes for plaque detection. The high avidity to CD44, good biocompatibility and high magnetic relaxivity of HA-NW render it an attractive probe for *in vivo* imaging and detection of atherosclerosis plaques as well as for longitudinal monitoring of plaques to aid in the development of novel therapeutic interventions.

3.11. Experimental

3.11.1. Materials

Iron (III) chloride hexahydrate ($FeCl_3.6H_2O$) was purchased from Honeywell Riedel-de Haën. Iron (II) chloride tetrahydrate ($FeCl_2.4H_2O$), dimethylsulfoxide (DMSO), dextran (MW: 10 and 40 kDa), formalin solution neutral buffered 10%, fetal bovine serum (FBS), Dulbecco's phosphate buffered saline (DPBS), Dulbecco's Modified Eagle Medium (DMEM), anti-CD44 antibody [MEM-85] and Amberlite® IR 120 hydrogen form (Amberlite H^+) were ordered from Sigma-Aldrich. Ultrafiltration disc (100 kDa) and centrifugal filter MWCO (100 kDa) were purchased from EMD Millipore. 2-Chloro-4,6-dimethoxy-1,3,5-triazine (CDMT) and N-methylmorpholine (NMM) were purchased form Acros Organics. Sodium hyaluronan (30 kDa) was obtained from Lifecore Biomedicals. Ammonium sulfate was purchased from Chempure® Chemicals. Fluorescein isothiocyanate (FITC), 4′,6-diamidino-2-phenylindole (DAPI), LysoTracker-594 DND and TURBO DNA-freeTM Kit were purchased from Invitrogen. Penicillin-Streptomycin (Pen Strep) mixture, trypsin-EDTA (0.5%), Power SYBR® Green PCR Master Mix and L-glutamine were obtained from Thermo-Fisher. EA.hy926 and SKOV-3 cells were ordered from American Tissue Culture Collection (ATCC). Goat anti-mouse HRP antibody was purchased from Biorad. HyGLOTM chemiluminescent HRP antibody detection reagent was purchased from Denville Scientific. Nitric acid TraceMetal grade and ammonium hydroxide were obtained from Fisher Scientific. Recombinant human (rh) CD44 was ordered from R&D Systems®. Mouse IgG2b antibody (PLPV219) was purchased from Abcam. RNeasy® Mini Kit was ordered from QIAGEN®. dNTP Mix, GoScriptTM Reverse Transcriptase, Random Primers and CellTiter 96 Aqueous One solution containing 3-(4,5-dimethylthiazol-2-yl)-5-(3-carboxy-methoxyphenyl)-2-

(4-sulfophenyl)-2H-tetrazolium (MTS) were purchased from Promega. TNF alpha mouse ELISA kit and IL-1 beta mouse ELISA kit were ordered from Thermo-Fisher.

3.11.2. Synthesis of HA-NWs

Nanoworms (NWs) were prepared using Fe^{2+} and Fe^{3+} salts in the presence of dextran[23]. Briefly, dextran (2.35 g, MW40 kDa), $FeCl_3.6H_2O$ (1.17 mmol) and $FeCl_2.4H_2O$ (0.63 mmol) were dissolved in MQ water (4.5 mL) under purge of Ar. Concentrated aqueous ammonia (0.5 mL) was then added dropwise to the reaction flask under vigorous stirring and a steady purge of Ar. It was then heated slowly up to 70 °C over 1 hour and held at this temperature for an additional hour. After being cooled to room temperature, the reaction mixture was diluted to 300 mL and washed using an ultrafiltration system (MWCO 100,000) 5 times to remove ammonium chloride salts and the excess amount of the base. The resulting NWs were concentrated to 30 mL then crosslinked by adding sodium hydroxide solution (5 M, 10 mL) and epichlorohydrin (ECH) (5 mL) under Ar flow and fast stirring for 24 hours. The reaction mixture was dialyzed against water followed by ultrafiltration 5 times to remove the excess amount of ECH. To functionalize crosslinked NWs by amine groups for further conjugation, cross-linked NWs were first concentrated to 30 mL then concentrated 30% ammonium hydroxide in water (10 mL) was added. The mixture was stirred vigorously for 36 hours at 37 °C. Finally, amine-functionalized NWs were washed by dialysis against distilled water for three times (12 hours each) to remove the excess base.

HA conjugation with NWs were performed through NMM and CDMT chemistry[19]. First, sodium hyaluronan (MW 31 kDa, 100 mg) was dissolved in MQ water (5 mL) then the pH was brought to 3 by adding Amberlite H^+ resin and it was stirred for 4 hours. The resin was removed by filtration and the mixture was freeze dried. The protonated HA (74 mg, 0.19 mmol carboxylic acid) was dissolved in MQ water (3 mL) followed by dropwise addition of acetonitrile (2 mL). Then, NMM

(22 μL, 0.2 mmol) and CDMT (18 mg, 0.10 mmol) were added to this HA solution. The reaction mixture was stirred at room temperature for 1 hour followed by addition of an aqueous dispersion of NWs (30 mg) and further stirring for 36 hours under nitrogen. HA-NWs were washed by ultrafiltration (MW 100,000) 5 times and stored for future experiments. HA-NWs were labeled with fluorescein isothiocyanate (FITC) by dissolving FITC (5 mg) in DMSO (2 mL) and adding this mixture to an aqueous solution of HA-NWs (70 mg in 10 mL water). The reaction mixture was stirred in dark for 48 hours then unreacted FITC was washed off through dialysis (5 times) in water and PBS buffer.

3.11.3. Characterization and Physicochemical Properties of HA-NWs

Following each step of NP synthesis, the size and charge of the NPs were measured by dynamic light scattering (DLS) using a Zetasizer Nano zs apparatus (Malvern, U.K.). The prepared NPs were imaged under transmission electron microscope (TEM) (JEM-2200FM) operating at 200 kV using Gatan multiscan CCD camera with Digital Micrograph imaging software. Thermal Gravimetric Analysis (TGA) was performed to quantify the total amount of organic content of NPs. Magnetic relaxivities (r_2* and r_1) were measured in a 7 T magnet.

3.11.4. Purification of HA-NWs

HA-NWs were washed with a concentrated ammonium sulfate solution (35%) through centrifugal filters (MWCO: 100 kDa). They were then transferred to a dialysis bag (MWCO: 3 kDa) to remove the excess salt through multiple exchanges (6 times) of distilled water. After purification, a modified electrophoresis gel staining method was used to enable visualization of HA in each sample[78]. Briefly, an agarose gel (0.8%) was prepared and samples containing HA-NWs both before and after purification containing the same amounts of Fe (40 μg) and free HA (70 μg) were

loaded on the gel. Before loading, each sample was mixed with 5 μL of sucrose solution (2 M) and 2 μL of bromophenol blue solution. The gel electrophoresis was run at 150 V for 70 minutes. Next, the gel was placed in a freshly prepared Stains-All dye solution (0.005%) in 50% ethanol for 24 hours in dark. Gels were destained in the dark using 10% ethanol solution and the ethanol mixture was exchanged every 12 hours until the purple color washed off from the gel.

3.11.5. Verifying CD44 Expression on Cells

Cells were grown in a 100 mm x 20 mm petri dish until 80% confluence was reached. The cell culture medium was removed, and cells were washed twice with PBS. Then lysis buffer, prepared by mixing 500 μL of RIPA buffer, protease inhibitor cocktail and 2.5 μL of phenyl methyl sulfonyl chloride (PMSF), was added to the cells while the petri dish was kept on ice for about 15 minutes until cell debris started to float around. Then cell lysates were collected by a cell scraper, transferred to an Eppendorf tube, and homogenized using a probe homogenizer. Protein content was quantified by a Bradford assay. Different concentrations of the lysates were loaded on a non-reducing gel (stacking gel:18%; resolving gel: 10%) with rhCD44 protein as the standard. The gel was subjected to electrophoresis (200 V) for 60 minutes, and the blots were then transferred to PVDF membrane (60 V) for 90 minutes. After blocking the membrane using 4% non-fat milk in TBS-tween (TBST) buffer, the membrane was first treated with mouse anti human CD44 mAb (MEM 85) diluted to 1:1000 in 4% non-fat milk in TBST at 4 °C overnight followed by goat anti-mouse HRP antibody (secondary Ab) for 1 hour. The membrane was sprayed with a chemiluminescent HRP detection reagent and developed onto autoradiography film.

3.11.6. HA-NW Uptake by CD44 Expressing Cells

Human vascular endothelial cells (EA.hy926) were used to evaluate the uptake of FITC-HA-NWs. Cells were suspended in a 6 well plate over a cover glass at a density of 105 cells per mL and incubated overnight at 37 °C and 5% CO_2 to adhere on cover glass and wells. After removing the medium and washing the cells with PBS buffer, a solution of FITC-HA-NWs (200 μg/mL) or FITC-HA-SPIONs (220 μg/mL) in DMEM without FBS was added to the cells. Both samples were adjusted to have the same fluorescence intensities. After 1 hour of incubation, Lysotracker Red (1 μM, 50μL/well) was added and the plate was incubated for another 1 hour. The supernatant was removed, and cells were washed 3 times with PBS buffer. The cells were fixed by adding 10% formalin (1 mL/well) and after 15 minutes, formalin was removed, and cells were washed with PBS buffer (3 times). DAPI solution (300 nM, 300 μL/well) plus 200 μL of PBS buffer were added to each well. After 4 minutes they were removed, and cells were washed 5 times by PBS buffer. The cover glass was placed on a microscope slide and images were obtained by Olympus FluoView 1000 LSM confocal microscope.

3.11.7. Dose Dependent Cellular Uptake of HA-NWs

To evaluate dose dependent uptake of HA-NWs by SKOV-3 cells, medium with different concentrations of HA-NWs were prepared (5, 10, 20, 50, 100, 200 and 400 μg Fe/mL) and incubated with cells for 1 hour. Then, the medium was removed, and cells were washed with PBS buffer 5 times to remove any unbound particles. Finally, cells were collected and treated with concentrated nitric acid for 2 hours at 60 ºC followed by addition of a diluted nitric acid (2%) solution. Fe content of each sample was analyzed by ICP-AES.

3.11.8. Time Dependent Cellular Uptake of HA-NWs

EA.hy926 cells were cultured in a 6 well plate at 37 ºC and 5% CO_2 until they became confluent. Then FITC-HA-NWs (50 μg/mL) were added to the cells and allowed to incubate for 1, 2 and 4 hours. Next, the medium was removed, and the cells were washed with PBS 3 times. Then, trypsin was used to detach the cells and it was neutralized by adding 5 volumes of serum-containing DMEM. Finally, cells were collected by centrifugation (1600 rpm, 5 minutes) and resuspended in DMEM and transferred to FACS tube and kept on ice until FACS analysis.

3.11.9. HA-NW Binding with CD44 Expressing Cells by FACS Analysis

To assess the binding of FITC-HA-NWs with CD44 expressing cells, human ovarian cancer cells (SKOV-3) were cultured in a 6 well plate (3×10^5 cells/well) and incubated at 37 °C and 5% CO_2 until the cells become confluent. Cells were washed with PBS then FITC-HA-NWs (100 μg/mL) and FITC-HA-SPIONs (110 μg/mL) at equivalent fluorescence amounts were dispersed in serum free DMEM and added to the cells and incubated for 1 hour at 37 °C and 5% CO_2. Medium was removed, and cells were washed with PBS 3 times. Cells were detached by adding trypsin, neutralized by adding 5 volumes of serum-containing DMEM, centrifuged (1600 rpm, 5 minutes), re-suspended in DMEM and transferred to FACS tubes kept on ice until FACS analysis.

3.11.10. HA-NW Binding with CD44 Expressing Cells by ICP Analysis

To evaluate the binding of HA-NWs with CD44 expressing cells by ICP, the amount of Fe was measured after 1-hour treatment of cells with HA-NWs and HA-SPIONs. Cells were cultured in a 6 well plate (3×10^5 cells/well) and incubated at 37 °C and 5% CO_2 until the cells became confluent. Then the medium was removed, and cells were washed with PBS buffer. HA-NWs (50 μg Fe/mL) and HA-SPIONs (50 μg Fe/mL) were dispersed in DMEM without FBS and added to

the cells for 1 hour. Next, medium was removed, and cells were washed with PBS buffer 3 times. Then cells were collected, 2 mL of concentrated HNO_3 was added and it was stored at 60 °C for 2 hours. Finally, each sample was diluted with HNO_3 solution (2%) and its Fe content was measured using ICP-AES.

3.11.11. Verifying the Role of HA in HA-NW Binding with CD44 Expressing Cells

To study the role of HA in binding of HA-NWs with CD44 expressing cells, FITC labeled NWs (FITC-NWs) were prepared and SKOV-3 cells were treated with equivalent fluorescence amounts of FITC-HA-NWs and FITC-NWs for 45 minutes. Then the medium was removed, and cells were washed with PBS buffer for 3 times. Next, cells were detached by adding trypsin and it was neutralized by adding 5 volumes of serum-containing DMEM. Finally, cells were collected by centrifugation (1600 rpm, 5 minutes) and re-suspended in DMEM and transferred to a FACS tube and kept on ice until FACS analysis.

3.11.12. Establishing the Role of CD44 and HA in HA-NW Binding with CD44 Expressing Cells

To investigate the role of CD44 for binding and uptake of HA-NWs, SKOV-3 cells were incubated with anti-CD44 antibody [MEM-85] (10 μL/mL) for 1 hour, then medium was removed, and cells were washed by PBS buffer. Next, the medium containing HA-NWs (100 μg/mL) was added and allowed to incubate for 45 minutes. Finally, cells were washed with PBS buffer 5 times and collected for ICP analysis. Mouse IgG2b [PLPV219] (20 μL/106 cells) was used as an isotype control Ab for this experiment.

To investigate the role of HA for binding of HA-NWs, SKOV-3 cells (1.2×10^6 cells per well) were incubated with free HA (10 mg/mL) for 0.5 hour, then the medium containing HA-NWs (100

μg/mL) was added and allowed to incubate for 1 hour. Finally, cells were washed with PBS buffer for 5 times and collected for ICP analysis to quantify Fe content.

3.11.13. Energy Dependent Uptake of HA-NWs

To investigate the dependency of HA-NW uptake on energy, binding experiments were performed at 4 ºC and 37 ºC respectively. SKOV-3 cells were cultured in a 6 well plate (3×10^5 cells/well) and incubated at 37 °C and 5% CO_2 until the cells became confluent. Cells were washed with PBS then FITC-HA-NWs (100 μg/mL) were dispersed in serum free DMEM and added to the cells and incubated for 1 hour at 37 °C or 4 °C. Then, the medium was removed, and the cells were washed with PBS 3 times. Next, the cells were detached by adding trypsin and they were neutralized by adding 5 volumes of serum-containing DMEM. Finally, the cells were collected by centrifugation (1600 rpm, 5 minutes) and resuspended in DMEM and transferred to a FACS tube and kept on ice until FACS analysis.

3.11.14. Analysis of RAW264.7 Cell Inflammatory Responses to HA-NWs

Real time PCR was used to measure inflammatory genes expression after treatment of mouse macrophage cells (RAW264.7) with nanoparticles. Cells (2×10^5/well) were cultured in a 6 well plate overnight until they reached to 70-80% confluence. HA-NWs and HA-SPIONs (6 μg Fe/mL) were dispersed in serum free medium and incubated with cells for 24 hours. The medium was then removed, and cells were washed with PBS buffer twice. Next, total RNA content of each well was extracted using RNA extraction kit (RNeasy® Mini Kit). Then, extracted RNA was purified using TURBO DNA-free™ Kit and the obtained RNA was quantified by NanoDrop™ and stored at -80 °C. cDNA was prepared from RNA and used for real time PCR. All the primers **Table 3-2** were ordered from IDT® company.

Table 3-2. Primer sequences of inflammatory genes used for RT-PCR study.

Gene	Forward primer (5′⟶ 3′)	Reverse primer (5′⟶ 3′)
IL-1a	CGAAGACTACAGTTCTGCCATT	GACGTTTCAGAGGTTCTCAGAG
IL-1b	TTCAGGCAGGCAGTATCACTC	GAAGGTCCACGGGAAAGACAC
MCP-1	TTAAAAACCTGGATCGGAACCAA	GCATTAGCTTCAGATTTACGGGT
TNF-a	CAGGCGGTGCCTATGTCTC	CGATCACCCCGAAGTTCAGTAG
Spp-1	ATCTCACCATTCGGATGAGTCT	TGTAGGGACGATTGGAGTGAAA
ICAM-1	GTGATGCTCAGGTATCCATCCA	CACAGTTCTCAAAGCACAGCG

3.11.15. Inflammatory Response to HA-NWs and HA-SPIONs In Vivo

The inflammatory responses to HA-NWs and HA-SPIONs *in vivo* were evaluated in wild type mice. First, blood (200 μL) was collected through saphenous vein to quantify the baseline levels of TNFα and IL-1β for each mouse. Then, HA-NWs or HA-SPIONs (8 mg Fe/kg) were administered to each group through retro-orbital injection and mice were sacrificed 1 and 24 hours after injection and blood was collected through cardiac puncture. The blood was centrifuged (4000 rpm, 30 minutes) and serum was collected and stored at -20 °C. For control study, PBS (100 μL) was administered. The amount of TNFα and IL-1β were quantified using TNFα mouse ELISA kit and IL-1β mouse ELISA kit according to manufacturer's instructions.

3.11.16. Cell Viability Assay of HA-NWs

EA.hy926 cells were cultured in a 96-well plate in DMEM cell culture media containing FBS (10%) for 24 h at 37 °C and 5% CO_2. The cells were then treated with different concentrations of NPs (0.0625, 0.125, 0.25, 0.5, 1 mg/mL) in serum free medium. After 4 h incubation at 37 °C, the medium was replaced with MTS solution (20 μL in 200 μL) in culture medium and incubated for 1 h at 37 °C. The developed brown color in the wells was an indication of live cells. The absorption

of the plate was measured at 490 nm in an iMark microplate reader (BioRad). Wells without cells (blanks) were subtracted as background from each sample.

3.11.17. Evaluation of the Biocompatibility of HA-NWs In Vivo

HA-NWs (8 mg Fe/kg) were administered to wild type mice via retro-orbital injection. After 24 hours, mouse blood was collected by cardiac puncture. Blood was stored in heparinized tube (BD Vacutainer^{TM}) at 4 ˚C and subsequently submitted for blood chemistry panel analysis. Moreover, liver, lung and kidney were extracted and fixed in 10% buffered formalin solution for histopathological analysis. In addition, another group of mice received PBS injection as control for blood chemistry panel and histopathological analysis.

3.11.18. In Vivo Imaging

Mice were purchased from Jackson Laboratories and were kept in the University Laboratory Animal Resources Facility of Michigan State University. All the experimental procedures and guidelines for animal study were performed under approval of Institutional Animal Care and Use Committee (IACUC) of Michigan State University.

Six-week old ApoE knockout mice were fed a high fat Western diet (TD.88137, Harlan Laboratories) for eight weeks. The mice were scanned on 7T MRI before and after retro-orbital injections of NPs. The abdominal aorta was serially scanned until the aortic lumen signal intensities returned to the pre-injection value. For control, HA-NWs were injected into age- and sex- matched wild type mice following an identical imaging protocol as performed on ApoE knockout mice. Moreover, to investigate the role of HA in mediating the selective binding of HA-NWs with CD44 on atherosclerotic plaques *in vivo*, bare NWs without HA were administered to ApoE knockout mice and MRI experiments were performed. For competition experiments, free

HA (33 mg/kg) were mixed with HA-NWs (8 mg Fe/kg) then injected to ApoE knockout mice and MRI images were collected.

Magnetic resonance experiments were performed on all mice anesthetized by 1.5% isoflurane following an induction using 4% isoflurane. Animals were secured in the supine position and restrained to reduce imaging artifacts due to motion. A Bruker 4-channel surface array was placed beneath the mouse to image the upper portion of abdominal aorta then placed in the isocenter of a Bruker 70/30 7 Tesla horizontal bore imaging spectrometer. Serial images were acquired using the following acquisition parameters: TE/TR=8/174 ms, in-plane resolution = 0.1 x 0.1 mm^2, slice thickness = 0.8 mm, Flip Angle = 50 deg, Number of Acquisition (NA) = 16. The TE and NA were selected to obtain good imaging contrast within a reasonable amount of time, i.e. around 5.9 minutes per acquisition.

3.11.19. Histological Studies

ApoE knockout and wild type control mice were sacrificed 2 hours after administration of HA-NWs and the aortas were harvested. The abdominal aorta was cut and placed in sucrose solution (30%) overnight, then fixed using a freshly prepared formalin solution. Specimens were processed, embedded in paraffin and sectioned on a rotary microtome at 4 μm. Sections were placed on slides and dried at 56 °C overnight. The slides were subsequently deparaffinized in xylene and hydrated through descending grades of ethyl alcohol to distilled water. Slides were placed in Tris Buffered Saline pH 7.4 (Scytek Labs – Logan, UT) for 5 minutes for pH adjustment. Slides then underwent enzyme induced epitope retrieval using 2% proteinase K in TE buffer, pH 8.0 for 3 minutes at room temperature (Table 2), followed by rinses in several changes of distilled water. Endogenous peroxidases were blocked utilizing 3% hydrogen peroxide / methanol bath for 30 minutes followed by running tap and distilled water rinses. Following pretreatments, standard micro-polymer

complex staining steps were performed at room temperature on the IntelliPath™ Flex Autostainer. All staining steps were followed by rinses in TBS Autowash buffer (Biocare Medical – Concord, CA). After blocking for non-specific protein with Mouse Block (Biocare) for 5 minutes, sections were incubated with specific primary antibodies **Table 3-3** in normal antibody diluent (NAD-Scytek) for 60 minutes. Micro-polymer (Biocare) reagents were subsequently applied for specified incubations followed by reaction with Romulin AEC™ (Biocare) and counterstained with Cat Hematoxylin **Table 3-3**.

Table 3-3. F4/80 staining protocol for macrophage staining in ApoE knockout mouse aorta.

Primary Ab	Ab Vendor:	Pretreatment:	Primary:	Staining System:
Rat anti – F4/80 Monoclonal	Biorad # *MCA497G* Hercules, CA	Proteinase K – room temperature – 3 min	1:100 in NAD – 60 minutes	ProMark Rat on Mouse HRP Polymer™: 15 minutes – Probe 15 minutes – Polymer AEC – 5 minutes CATHE Hematoxylin 1:10 – 1 minute

In addition, ApoE knockout mouse aorta was incubated with HA-NWs (0.2 mg Fe/mL) at 37 ºC for 1 hour. Aorta tissues were then washed with PBS buffer for 5 times and immersed in freshly prepared mixture (1:1) of 2% HCl and an aqueous 2% potassium ferrocyanide solution for 15 minutes. The solution was removed, and the tissues were washed with PBS buffer and stored in ethanol solution.

REFERENCES

REFERENCES

(1) Weber, C.; Noels, H. Atherosclerosis: current pathogenesis and therapeutic options. *Nat. Med.* **2011,** *17* (11), 1410-1422.

(2) Chelly, J.; Mongardon, N.; Dumas, F.; Varenne, O.; Spaulding, C.; Vignaux, O.; Carli, P.; Charpentier, J.; Pène, F.; Chiche, J. D.; Mira, J. P.; Cariou, A. Benefit of an early and systematic imaging procedure after cardiac arrest: insights from the PROCAT (Parisian Region Out of Hospital Cardiac Arrest) registry. *Resuscitation* **2012,** *83* (12), 1444-1450.

(3) Benjamin, E. J.; Blaha, M. J.; Chiuve, S. E.; Cushman, M.; Das, S. R.; Deo, R.; de Ferranti, S. D.; Floyd, J.; Fornage, M.; Gillespie, C.; Isasi, C. R.; Jiménez, M. C.; Jordan, L. C.; Judd, S. E.; Lackland, D.; Lichtman, J. H.; Lisabeth, L.; Liu, S.; Longenecker, C. T.; Mackey, R. H.; Matsushita, K.; Mozaffarian, D.; Mussolino, M. E.; Nasir, K.; Neumar, R. W.; Palaniappan, L.; Pandey, D. K.; Thiagarajan, R. R.; Reeves, M. J.; Ritchey, M.; Rodriguez, C. J.; Roth, G. A.; Rosamond, W. D.; Sasson, C.; Towfighi, A.; Tsao, C. W.; Turner, M. B.; Virani, S. S.; Voeks, J. H.; Willey, J. Z.; Wilkins, J. T.; Wu, J. H.; Alger, H. M.; Wong, S. S.; Muntner, P. Heart disease and stroke statistics—2017 update: a report from the american heart association. *Circulation* **2017,** *135*, https://doi.org/10.1161/CIR.0000000000000485.

(4) Tarkin, J. M.; Dewck, M. R.; Evans, N. R.; Takx, R. A. P.; Brown, A. J.; Tawakol, A.; Fayad, Z. A.; Rudd, J. H. F. Imaging atherosclerosis. *Circ. Res.* **2016,** *118*, 750-769.

(5) Mulder, W. J. M.; Jaffer, F. A.; Fayad, Z. A.; Nahrendorf, M. Imaging and nanomedicine in inflammatory atherosclerosis. *Sci. Transl. Med.* **2014,** *6* (239), 239sr1.

(6) Moonen, R. P. M.; Strijkers, G. J.; Fayad, Z. A.; Daemen, M. J. A. P.; Nicolay, K., Molecular MR Imaging of Atherosclerosis. In *Cardiovascular imaging: arterial and aortic valve inflammation and calcification*, Aikawa, E., Ed. Springer International Publishing: Cham, 2015; pp 269-296.

(7) Corti, R.; Fuster, V. Imaging of atherosclerosis: magnetic resonance imaging. *Eur. Heart J.* **2011,** *32* (14), 1709–1719.

(8) Hyafil, F.; Feldman, L.; Fayad, Z. A.; Le Guludec, D. Imaging atherosclerotic plaques with MRI: role of contrast agents. *Curr. Cardiovasc. Imaging Rep.* **2013,** *6* (1), 76-88.

(9) Gao, Z.; Ma, T.; Zhao, E.; Docter, D.; Yang, W.; Stauber, R. H.; Gao, M. Small is smarter: nano MRI contrast agents – advantages and recent achievements. *Small* **2016,** *12* (5), 556-576.

(10) Zhao, L.; Lee, E.; Zukas, A. M.; Middleton, M. K.; Kinder, M.; Acharya, P. S.; Hall, J. A.; Rader, D. J.; Puré, E. CD44 expressed on both bone marrow–derived and non–bone marrow–derived cells promotes atherogenesis in ApoE-deficient mice. *Arterioscler. Thromb. Vasc. Biol.* **2008,** *28* (7), 1283-1289.

(11) Puré, E.; Cuff, C. A. A crucial role for CD44 in inflammation. *Trends Mol. Med.* **2001,** *7* (5), 213-221.

(12) Cuff, C. A.; Kothapalli, D.; Azonobi, I.; Chun, S.; Zhang, Y.; Belkin, R.; Yeh, C.; Secreto, A.; Assoian, R. K.; Rader, D. J.; Puré, E. The adhesion receptor CD44 promotes atherosclerosis by mediating inflammatory cell recruitment and vascular cell activation. *J. Clin. Investig.* **2001,** *108* (7), 1031-1040.

(13) Krettek, A.; Sukhova, G. K.; Schönbeck, U.; Libby, P. Enhanced expression of CD44 variants in human atheroma and abdominal aortic aneurysm: possible role for a feedback loop in endothelial cells. *Am. J. Pathol.* **2004,** *165* (5), 1571-1581.

(14) Hägg, D.; Sjöberg, S.; Hultén, L. M.; Fagerberg, B.; Wiklund, O.; Rosengren, A.; Carlsson, L. M. S.; Borén, J.; Svensson, P.-A.; Krettek, A. Augmented levels of CD44 in macrophages from atherosclerotic subjects: a possible IL-6–CD44 feedback loop? *Atherosclerosis* **2007,** *190* (2), 291-297.

(15) Kolodgie, F. D.; Burke, A. P.; Farb, A.; Weber, D. K.; Kutys, R.; Wight, T. N.; Virmani, R. Differential accumulation of proteoglycans and hyaluronan in culprit lesions: insights into plaque erosion. *Arterioscler. Thromb. Vasc. Biol.* **2002,** *22* (10), 1642-1648.

(16) Misra, S.; Hascall, V. C.; Markwald, R. R.; Ghatak, S. Interactions between hyaluronan and its Receptors (CD44, RHAMM) regulate the activities of inflammation and cancer. *Front. Immunol.* **2015,** *6*, Article 201.

(17) Toole, B. P. Hyaluronan: from extracellular glue to pericellular cue. *Nat. Rev. Cancer* **2004,** *4* (7), 528-539.

(18) Maiti, A.; Maki, G.; Johnson, P. TNF-alpha induction of CD44-mediated leukocyte adhesion by sulfation. *Science (New York, N.Y.)* **1998,** *282* (5390), 941-3.

(19) Kamat, M.; El-boubbou, K.; Zhu, D. C.; Lansdell, T.; Lu, X.; Li, W.; Huang, X. Hyaluronic acid immobilized magnetic nanoparticles for active targeting and imaging of macrophages. *Bioconjugate Chem.* **2010,** *21* (11), 2128-2135.

(20) El-Dakdouki, M. H.; El-Boubbou, K.; Kamat, M.; Huang, R.; Abela, G. S.; Kiupel, M.; Zhu, D. C.; Huang, X. CD44 targeting magnetic glyconanoparticles for atherosclerotic plaque imaging. *Pharm. Res.* **2014,** *31* (6), 1426-1437.

(21) Lee, G. Y.; Kim, J.-H.; Choi, K. Y.; Yoon, H. Y.; Kim, K.; Kwon, I. C.; Choi, K.; Lee, B.-H.; Park, J. H.; Kim, I.-S. Hyaluronic acid nanoparticles for active targeting atherosclerosis. *Biomaterials* **2015,** *53*, 341-348.

(22) Beldman, T. J.; Senders, M. L.; Alaarg, A.; Pérez-Medina, C.; Tang, J.; Zhao, Y.; Fay, F.; Deichmöller, J.; Born, B.; Desclos, E.; van der Wel, N. N.; Hoebe, R. A.; Kohen, F.; Kartvelishvily, E.; Neeman, M.; Reiner, T.; Calcagno, C.; Fayad, Z. A.; de Winther, M. P. J.; Lutgens, E.; Mulder, W. J. M.; Kluza, E. Hyaluronan nanoparticles selectively target plaque-associated macrophages and improve plaque stability in atherosclerosis. *ACS Nano* **2017,** *11* (6), 5785-5799.

(23) Park, J. H.; von Maltzahn, G.; Zhang, L.; Schwartz, M. P.; Ruoslahti, E.; Bhatia, S. N.; Sailor, M. J. Magnetic iron oxide nanoworms for tumor targeting and imaging. *Advanced materials (Deerfield Beach, Fla.)* **2008,** *20* (9), 1630-1635.

(24) Marroquin, C. E.; Downey, L.; Guo, H.; Kuo, P. C. Osteopontin increases CD44 expression and cell adhesion in RAW 264.7 murine leukemia cells. *Immunol. Lett.* **2004,** *95*, 109-112.

(25) Amash, A.; Wang, L.; wang, Y.; Bhakta, V.; Fairn, G. D.; Hou, M.; Peng, J.; Sheffield, W. P.; Lazarus, A. H. CD44 antibody inhibition of macrophage phagocytosis targets Fcγ receptor– and complement receptor 3–dependent mechanisms. *J. Immunol.* **2016,** *196* (8), 3331-3340.

(26) El-Dakdouki, M. H.; Zhu, D. C.; El-boubbou, K.; Kamat, M.; Chen, J.; Li, W.; Huang, X. Development of multifunctional hyaluronan-coated nanoparticles for imaging and drug delivery to cancer cells. *Biomacromolecules* **2012,** *13*, 1144-1151.

(27) Ahrens, T.; Assmann, V.; Fieber, C.; Termeer, C. C.; Herrlich, P.; Hofmann, M.; Simon, J. C. CD44 is the principal mediator of hyaluronic-acid-induced melanoma cell proliferation. *J. Investig. Dermatol.* **2001,** *116* (1), 93-101.

(28) Qhattal, H. S. S.; Liu, X. Characterization of CD44-mediated cancer cell uptake and intracellular distribution of hyaluronan-grafted liposomes. *Mol. Pharm.* **2011,** *8* (4), 1233-1246.

(29) Thankamony, S. P.; Knudson, W. Acylation of CD44 and its association with lipid rafts are required for receptor and hyaluronan endocytosis. *J. Biol. Chem.* **2006,** *281* (45), 34601-34609.

(30) Garlanda, C.; Dinarello, C. A.; Mantovani, A. The Interleukin-1 family: back to the future. *Immunity* **2013,** *39* (6), 1003-1018.

(31) Radhakrishnan, G.; Suzuki, R.; Maeda, H.; Yamamoto, M.; Hirose, N.; Gopalrao, R. K.; Lee, G. H.; Hayashi, Y.; Rao, P.; Sasaguri, S. Inhibition of neointimal hyperplasia development by MCI-186 is correlated with downregulation of nuclear factor-kappaB pathway. *Circulation journal : official journal of the Japanese Circulation Society* **2008,** *72* (5), 800-806.

(32) Wolfs, I. M.; Donners, M. M.; de Winther, M. P. Differentiation factors and cytokines in the atherosclerotic plaque micro-environment as a trigger for macrophage polarisation. *Thrombosis and haemostasis* **2011,** *106* (5), 763-771.

(33) Petrache, I.; Birukova, A.; Ramirez, S. I.; Garcia, J. G.; Verin, A. D. The role of the microtubules in tumor necrosis factor-alpha-induced endothelial cell permeability. *American journal of respiratory cell and molecular biology* **2003,** *28* (5), 574-581.

(34) Maziere, C.; Auclair, M.; Maziere, J. C. Tumor necrosis factor enhances low density lipoprotein oxidative modification by monocytes and endothelial cells. *FEBS letters* **1994,** *338* (1), 43-46.

(35) Ohta, H.; Wada, H.; Niwa, T.; Kirii, H.; Iwamoto, N.; Fujii, H.; Saito, K.; Sekikawa, K.; Seishima, M. Disruption of tumor necrosis factor-alpha gene diminishes the development of atherosclerosis in ApoE-deficient mice. *Atherosclerosis* **2005,** *180* (1), 11-17.

(36) Bai, L.; Li, Z.; Li, Q.; Guan, H.; Zhao, S.; Liu, R.; Wang, R.; Zhang, J.; Jia, Y.; Fan, J.; Wang, N.; Reddy, J. K.; Shyy, J. Y.-J.; Liu, E. Mediator 1 is atherosclerosis protective by regulating macrophage polarization. *Arterioscler. Thromb. Vasc. Biol.* **2017,** *37*, 1470-1481.

(37) Kuwahara, F.; Kai, H.; Tokuda, K.; Shibata, R.; Kusaba, K.; Tahara, N.; Niiyama, H.; Nagata, T.; Imaizumi, T. Hypoxia-inducible factor-1alpha/vascular endothelial growth factor pathway for adventitial vasa vasorum formation in hypertensive rat aorta. *Hypertension (Dallas, Tex. : 1979)* **2002,** *39* (1), 46-50.

(38) Jaipersad, A. S.; Lip, G. Y.; Silverman, S.; Shantsila, E. The role of monocytes in angiogenesis and atherosclerosis. *J. Am. Coll. Cardiol.* **2014,** *63* (1), 1-11.

(39) Corot, C.; Robert, P.; Idée, J.-M.; Port, M. Recent advances in iron oxide nanocrystal technology for medical imaging. *Adv. Drug Deliv. Rev.* **2006,** *58* (14), 1471-1504.

(40) Abela, G. S.; Picon, P. D.; Friedl, S. E.; Gebara, O. C.; Miyamoto, A.; Federman, M.; Tofler, G. H.; Muller, J. E. Triggering of plaque disruption and arterial thrombosis in an atherosclerotic rabbit model. *Circulation* **1995,** *91*, 776-784.

(41) Rosenfeld, M. E.; Polinsky, P.; Virmani, R.; Kauser, K.; Rubanyi, G.; Schwartz, S. M. Advanced atherosclerotic lesions in the innominate artery of the ApoE knockout mouse. *Arterioscler. Thromb. Vasc. Biol.* **2000,** *20* (12), 2587-2592.

(42) Wouters, K.; Shiri-Sverdlov, R.; van Gorp, P. J.; van Bilsen, M.; Hofker, M. H. Understanding hyperlipidemia and atherosclerosis: lessons from genetically modified apoe and ldlr mice. *Clin. Chem. Lab Med.* **2005,** *43* (5), 470-479.

(43) Jackson, C. L.; Bennett, M. R.; Biessen, E. A. L.; Johnson, J. L.; Krams, R. Assessment of unstable atherosclerosis in mice. *Arterioscler. Thromb. Vasc. Biol.* **2007,** *27*, 714-720.

(44) Yu, M.; Huang, S.; Yu, K. J.; Clyne, A. M. Dextran and polymer polyethylene glycol (PEG) coating reduce both 5 and 30 nm iron oxide nanoparticle cytotoxicity in 2D and 3D cell culture. *Int. J. Mol. Sci.* **2012,** *13* (5), 5554-5570.

(45) Weissleder, R.; Stark, D. D.; Engelstad, B. L.; Bacon, B. R.; Compton, C. C.; White, D. L.; Jacobs, P.; Lewis, J. Superparamagnetic iron oxide: pharmacokinetics and toxicity. *Am. J. Roentgenol.* **1989,** *152* (1), 167-173.

(46) Singh, N.; Jenkins, G. J. S.; Asadi, R.; Doak, S. H. Potential toxicity of superparamagnetic iron oxide nanoparticles (SPION). *Nano Rev.* **2010,** *1*, 5358.

(47) Berry, C. C.; Wells, S.; Charles, S.; Aitchison, G.; Curtis, A. S. G. Cell response to dextran-derivatised iron oxide nanoparticles post internalisation. *Biomaterials* **2004,** *25* (23), 5405-5413.

(48) Benne, N.; van Duijn, J.; Kuiper, J.; Jiskoot, W.; Slütter, B. Orchestrating immune responses: how size, shape and rigidity affect the immunogenicity of particulate vaccines. *J. Control. Release* **2016,** *234*, 124-134.

(49) Truong, N. P.; Whittaker, M. R.; Mak, C. W.; Davis, T. P. The importance of nanoparticle shape in cancer drug delivery. *Expert Opin. Drug Deliv.* **2015,** *12* (1), 129-142.

(50) Verma, A.; Stellacci, F. Effect of surface properties on nanoparticle-cell interactions. *Small* **2010,** *6* (1), 12-21.

(51) Li, Z.; Sun, L.; Zhang, Y.; Dove, A. P.; O'Reilly, R. K.; Chen, G. Shape effect of glyco-nanoparticles on macrophage cellular uptake and immune response. *ACS Macro Lett.* **2016,** *5* (9), 1059-1064.

(52) Chithrani, B. D.; Ghazani, A. A.; Chan, W. C. W. Determining the size and shape dependence of gold nanoparticle uptake into mammalian cells. *Nano Lett.* **2006,** *6* (4), 662-668.

(53) Zhang, K.; Fang, H.; Chen, Z.; Taylor, J.-S. A.; Wooley, K. L. Shape effects of nanoparticles conjugated with cell-penetrating peptides (HIV Tat PTD) on CHO cell uptake. *Bioconjugate Chem.* **2008,** *19* (9), 1880-1887.

(54) Chen, X.; Yan, Y.; Müllner, M.; Ping, Y.; Cui, J.; Kempe, K.; Cortez-Jugo, C.; Caruso, F. Shape-dependent activation of cytokine secretion by polymer capsules in human monocyte-derived macrophages. *Biomacromolecules* **2016,** *17* (3), 1205-1212.

(55) Park, J. H.; von Maltzahn, G.; Zhang, L.; Derfus, A. M.; Simberg, D.; Harris, T. J.; Ruoslahti, E.; Bhatia, S. N.; Sailor, M. J. Systematic surface engineering of magnetic nanoworms for in vivo tumor targeting. *Small* **2009,** *5* (6), 694-700.

(56) Niikura, K.; Matsunaga, T.; Suzuki, T.; Kobayashi, S.; Yamaguchi, H.; Orba, Y.; Kawaguchi, A.; Hasegawa, H.; Kajino, K.; Ninomiya, T.; Ijiro, K.; Sawa, H. Gold nanoparticles as a vaccine platform: influence of size and shape on immunological responses *in vitro* and *in vivo*. *ACS Nano* **2013,** *7* (5), 3926-3938.

(57) Tammi, R.; MacCallum, D.; Hascall, V. C.; Pienimäki, J.-P.; Hyttinen, M.; Tammi, M. Hyaluronan bound to CD44 on keratinocytes is displaced by hyaluronan decasaccharides and not hexasaccharides. *J. Biol. Chem.* **1998,** *273* (44), 28878-28888.

(58) Benerji, S.; Wright, A. J.; Noble, M.; Mahoney, D. J.; Campbell, I. D.; Day, A. J.; Jackson, D. G. Structures of the CD44–hyaluronan complex provide insight into a fundamental carbohydrate protein interaction. *Nat. Struct. Mol. Biol.* **2007,** *14*, 234-239.

(59) Mizrahy, S.; Raz, S. R.; Hasgaard, M.; Liu, H.; Soffer-Tsur, N.; Cohen, K.; Dvash, R.; Landsman-Milo, D.; Bremer, M. G. E. G.; Moghimi, S. M.; Peer, D. Hyaluronan-coated nanoparticles: the influence of the molecular weight on CD44-hyaluronan interactions and on the immune response. *J. Control. Release* **2011,** *156* (2), 231-238.

(60) Jiang, D.; Liang, J.; Noble, P. W. Hyaluronan as an immune regulator in human diseases. *Physiol. Rev.* **2011,** *91* (1), 221-264

(61) Stern, R.; Asari, A. A.; Sugahara, K. N. Hyaluronan fragments: an information-rich system. *Eur. J. Cell Biol.* **2006,** *85* (8), 699-715.

(62) Thorek, D. L. J.; Chen, A. K.; Czupryna, J.; Tsourkas, A. Superparamagnetic iron oxide nanoparticle probes for molecular imaging. *Ann. Biomed. Eng.* **2006,** *34* (1), 23-38.

(63) Wang, Y.-X. J.; Hussain, S. M.; Krestin, G. P. Superparamagnetic iron oxide contrast agents: physicochemical characteristics and applications in MR imaging. *Eur. Radiol.* **2001,** *11* (11), 2319-2331.

(64) Sigovan, M.; Boussel, L.; Sulaiman, A.; Sappey-Marinier, D.; Alsaid, H.; Desbleds-Mansard, C.; Ibarrola, D.; Gamondès, D.; Corot, C.; Lancelot, E.; Raynaud, J.-S.; Vives, V.; Laclédère, C.; Violas, X.; Douek, P. C.; Canet-Soulas, E. Rapid-clearance iron nanoparticles for inflammation imaging of atherosclerotic plaque: initial experience in animal model. *Radiology* **2009,** *252* (2), 401-409.

(65) Morris, J. B.; Olzinski, A. R.; Bernard, R. E.; Aravindhan, K.; Mirabile, R. C.; Boyce, R.; Willette, R. N.; Jucker, B. M. p38 MAPK inhibition reduces aortic ultrasmall superparamagnetic iron oxide uptake in a mouse model of atherosclerosis MRI assessment. *Arterioscler. Thromb. Vasc. Biol.* **2008,** *28* (2), 265-271.

(66) Durand, E.; Raynaud, J. S.; Bruneval, P.; Brigger, I.; Al Haj Zen, A.; Mandet, C.; Lancelot, E.; Lafont, A. Magnetic resonance imaging of ruptured plaques in the rabbit with ultrasmall superparamagnetic particles of iron oxide. *J. Vasc. Res.* **2007,** *44*, 119-128.

(67) Ruehm, S. G.; Corot, C.; Vogt, P.; Kolb, S.; Debatin, J. F. Magnetic resonance imaging of atherosclerotic plaque with ultrasmall superparamagnetic particles of iron oxide in hyperlipidemic rabbits. *Circulation* **2001,** *103* (3), 415-422.

(68) Morishige, K.; Kacher, D. F.; Libby, P.; Josephson, L.; Ganz, P.; Weissleder, R.; Aikawa, M. High-resolution magnetic resonance imaging enhanced with superparamagnetic nanoparticles measures macrophage burden in atherosclerosis. *Circulation* **2010,** *122* (17), 1707-1715.

(69) Hyafil, F.; Laissy, J.-P.; Mazighi, M.; Tchétché, D.; Louedec, L.; Adle-Biassette, H.; Chillon, S.; Henin, D.; Jacob, M.-P.; Letourneur, D.; Feldman, L. J. Ferumoxtran-10–enhanced MRI of the hypercholesterolemic rabbit aorta relationship between signal loss and macrophage infiltration. *Arterioscler. Thromb. Vasc. Biol.* **2006,** *26* (1), 176-181.

(70) McAteer, M. A.; Schneider, J. E.; Ali, Z. A.; Warrick, N.; Bursill, C. A.; von zur Muhlen, C.; Greaves, D. R.; Neubauer, S.; Channon, K. M.; Choudhury, R. P. Magnetic resonance imaging of endothelial adhesion molecules in mouse atherosclerosis using dual-targeted microparticles of iron oxide. *Arterioscler. Thromb. Vasc. Biol.* **2008,** *28* (1), 77-83.

(71) Smith, B. R.; Heverhagen, J.; Knopp, M.; Schmalbrock, P.; Shapiro, J.; Shiomi, M.; Moldovan, N. I.; Ferrari, M.; Lee, S. C. Localization to atherosclerotic plaque and biodistribution of biochemically derivatized superparamagnetic iron oxide nanoparticles (SPIONs) contrast particles for magnetic resonance imaging (MRI). *Biomed. Microdevices* **2007,** *9* (5), 719-727.

(72) Sosnovik, D. E.; Schellenberger, E. A.; Nahrendorf, M.; Novikov, M. S.; Matsui, T.; Dai, G.; Reynolds, F.; Grazette, L.; Rosenzweig, A.; Weissleder, R.; Josephson, L. Magnetic resonance imaging of cardiomyocyte apoptosis with a novel magneto-optical nanoparticle. *Magn. Reson. Med.* **2005,** *54* (3), 718-724.

(73) Nahrendorf, M.; Jaffer, F. A.; Kelly, K. A.; Sosnovik, D. E.; Aikawa, E.; Libby, P.; Weissleder, R. Noninvasive vascular cell adhesion molecule-1 imaging identifies inflammatory activation of cells in atherosclerosis. *Circulation* **2006,** *114* (14), 1504-1511.

(74) Kelly, K. A.; Allport, J. R.; Tsourkas, A.; Shinde-Patil, V. R.; Josephson, L.; Weissleder, R. Detection of vascular adhesion molecule-1 expression using a novel multimodal nanoparticle. *Circ. Res.* **2005,** *96* (3), 327-336.

(75) Tu, C.; Ng, T. S. C.; Sohi, H. K.; Palko, H. A.; House, A.; Jacobs, R. E.; Louie, A. Y. Receptor-targeted iron oxide nanoparticles for molecular MR imaging of inflamed atherosclerotic plaques. *Biomaterials* **2011,** *32* (29), 7209-7216.

(76) Meding, J.; Urich, M.; Licha, K.; Reinhardt, M.; Misselwitz, B.; Fayad, Z. A.; Weinmann, H.-J. Magnetic resonance imaging of atherosclerosis by targeting extracellular matrix deposition with gadofluorine M. *Contrast Media Mol. Imaging* **2007,** *2* (3), 120-129.

(77) Sadowitz, B.; Seymour, K.; Gahtan, V.; Maier, K. G. The role of hyaluronic acid in atherosclerosis and intimal hyperplasia. *The Journal of surgical research* **2012,** *173* (2), e63-e72.

(78) Lee, H. G.; Cowman, M. K. An agarose gel electrophoretic method for analysis of hyaluronan molecular weight distribution. *Analytical biochemistry* **1994,** *219* (2), 278-287.

Chapter 4: Effective Atherosclerotic Plaque Inflammation Inhibition with Hyaluronan Conjugated Atorvastatin Nanoparticles

4.1. Introduction

Atherosclerosis is a chronic inflammatory condition in the artery. The rupture of atherosclerotic plaques is a major cause of heart attack and stroke[1], which threatens the lives of more than 1.2 million Americans per year[2]. As local inflammation is a significant risk factor for plaque rupture[3], reducing plaque inflammation is an attractive therapeutic strategy to prevent atherothrombotic events[1].

3-Hydroxy-3-methylglutaryl coenzyme A (HMG-CoA) reductase inhibitors known as statins are widely prescribed medicines that can decrease adverse cardiac events by 30%. While a major mode of action of statins is believed to be the reduction of serum levels of cholesterol, statins can inhibit the activities of inflammatory cells[4]. In apolipoprotein E (ApoE)-knockout mouse, a common model for human atherosclerosis development, while statins did not affect serum lipid levels even at a very high dose (100 mg/kg body weight), reduced plaque formation was observed in these mice suggesting anti-atherosclerotic activity of statins beyond its plasma cholesterol-lowering functions[5]. However, in humans, such high doses are not feasible due to the low bioavailability of statins entering the systemic circulation resulting from an extensive first pass effect at the liver as well as the adverse side effects such as musculoskeletal and liver toxicity at high doses[6-9]. Therefore, strategies to deliver statins to inflammatory atherosclerotic plaques can be a potential strategy for atherosclerosis treatment.

Recently, high-density lipoprotein nanoparticles (HDL-NPs) loaded with a statin (simvastatin) have been developed using human apolipoprotein A-I (ApoA-I), which can mimic the native HDL particles in the body, accumulate in plaque tissues and deliver the statin. In an intensive treatment regimen (HDL-NPs containing 60 mg/kg body weight simvastatin and 40 mg/kg ApoA-I, four injections per week) of ApoE knockout mice, inflammation in atherosclerotic plaques was

markedly reduced, highlighting the potential of this approach. However, ApoA-I is expensive ($309/0.5 mg from Sigma) possibly hindering the wide applications of HDL-NPs. As an alternative, we investigate the utility of the readily available hyaluronan (HA) as the scaffold to deliver statins by targeting the CD44 receptor.

CD44 is a cell adhesion receptor expressed on the surface of major cell types present in the atherosclerotic plaques, including vascular endothelial cells, smooth muscle cells, macrophages and T cells[10-13]. Multiple studies have suggested that CD44 promotes atherosclerosis by mediating inflammatory cell recruitment and vascular cell activation[11, 14-15]. In both ApoE knockout mice[11, 15] and humans[10, 16-17], the levels of CD44 expression present in rupture-prone macrophage-rich regions of human atherosclerotic plaques were over 10 times higher than that in healthy vascular tissues. The elevated CD44 expression in rupture prone plaque sites render it an appealing target for targeted delivery.

4.2. Design and Synthesis of HA-ATV-NPs

For drug delivery, the ability to deliver high drug loading per particle is highly desirable. Previously, we synthesized HA coated NPs with iron oxide core for magnetic resonance imaging of atherosclerotic plaques and cancer[18-21]. Doxorubicin has been loaded on the surface of these magnetic NPs, which could be released in tumor tissues with enhanced abilities to kill cancer cells. However, as the cargo were only loaded on the surface of these magnetic NPs, the amount of drug per particle was relatively low (2.1% by weight). To enhance drug delivery capabilities of HA-NPs, the new design reported here took advantage of the hydrophobic nature of the statin cargo, i.e., atorvastatin (ATV). Upon conjugation of ATV with HA, the resulting amphiphilic polymer could assemble into NPs in aqueous solutions with ATV as the hydrophobic core.

In order to conjugate HA with ATV, ATV was first converted to isopropylidene protected carboxylic acid **2**, which was esterified by the *N*-protected ethanolamine **4** and subsequently hydrogenated to yield ATV amine **5 Figure 4-1**. The NMR spectra and ESI mass for amine **5** have been shown below in **Figure 4-2**, **Figure 4-3**, **Figure 4-4** and **Figure 4-5**. The calculated mass for ATV amine is m/z:641.33. The conjugation of amine **5** with HA (16 kDa) was mediated by 2-chloro-4,6-dimethoxy-1,3,5-triazine (CDMT) with *N*-methylmorpholine (NMM) as the base in a mixed solvent of water, acetonitrile and DMSO **Figure 4-6**. Upon removal of any free ATV through extensive dialysis, the successful conjugation of HA with ATV was confirmed by NMR analysis as signals from both ATV and HA were well resolved in its ^{1}H-NMR spectrum in D_6-DMSO **Figure 4-7**. By comparing the ratio of integration of aromatic signals (from ATV) and that of the *N*-acetyl group (from HA), the average number of ATV per HA disaccharide was determined to be 0.4, which corresponded to 35% w/w of the total mass of conjugate being ATV. The HA-ATV was subjected to agarose gel electrophoresis and stained with Stains-All dye. As shown in **Figure 4-8**, HA-ATV migrated markedly slower than pure HA on agarose gel. In addition, pure HA stained blue with the Stains-All dye, while HA-ATV appeared purple with the same stain, confirming the successful conjugation of HA with ATV.

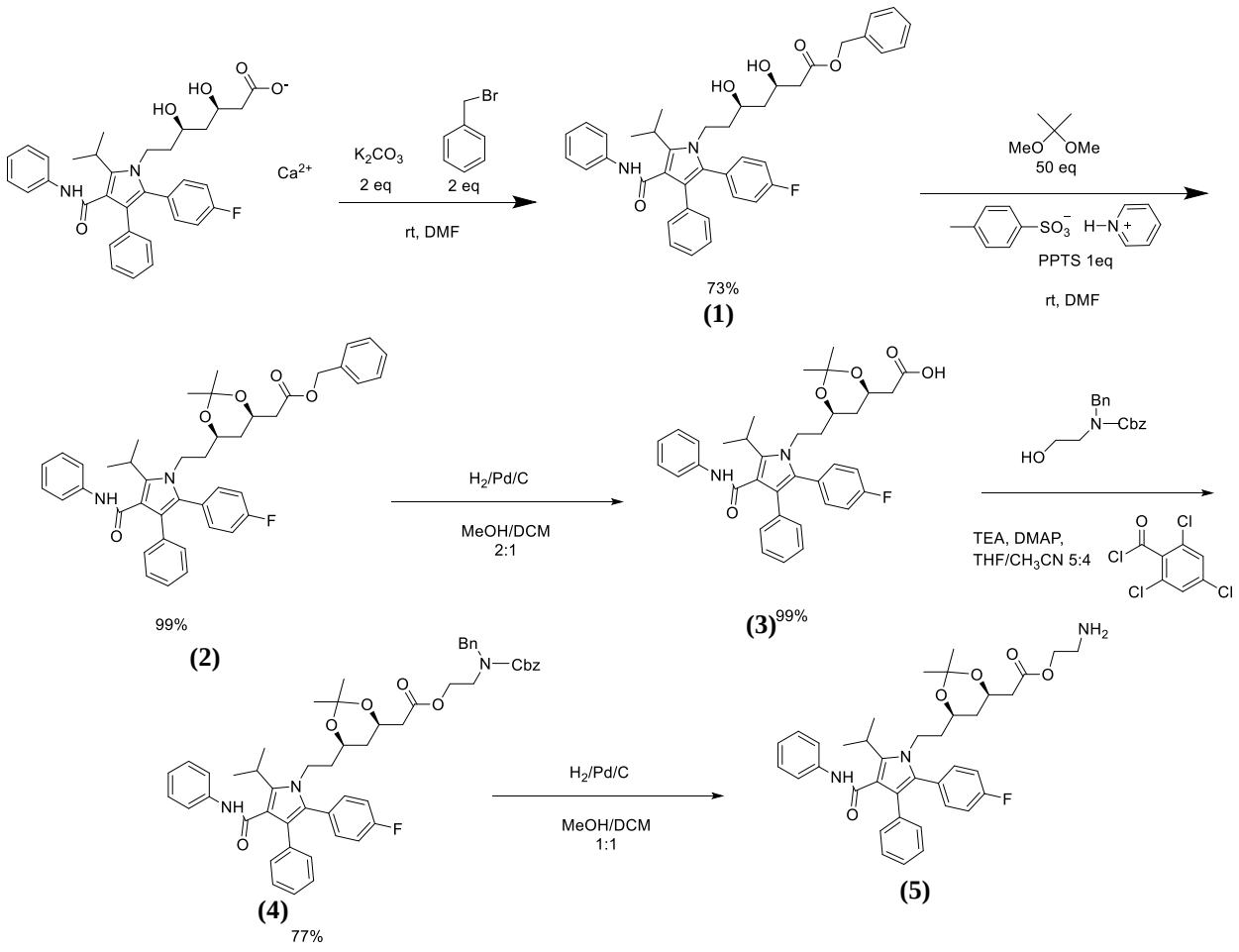

Figure 4-1. Synthesis of atorvastatin-linker (ATV-linker). Design and synthesis have been done by Dr. Sharif Ramadan.

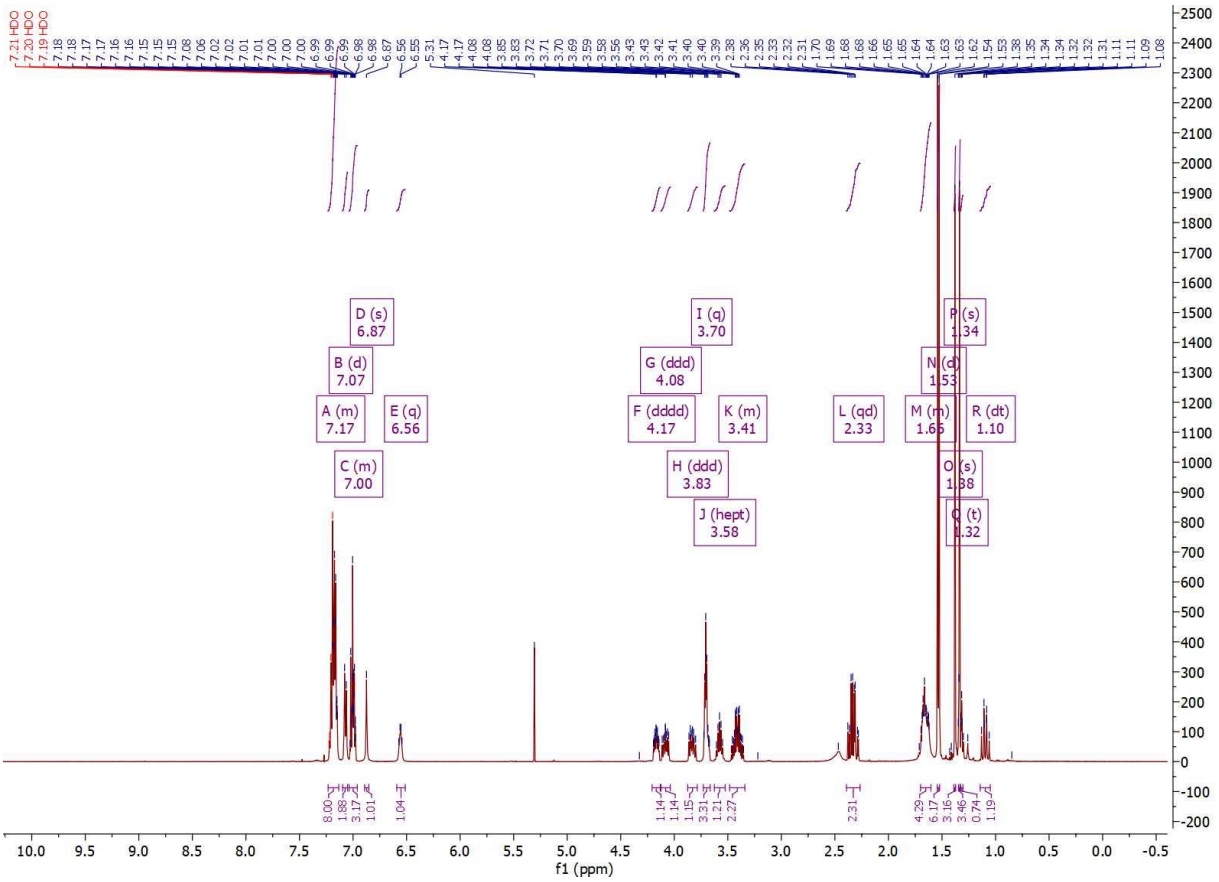

Figure 4-2. H-NMR of atorvastatin-linker (ATV-linker).

H NMR for Atorvastatin-linker:
^{1}H NMR (500 MHz, Chloroform-*d*) δ 7.23 – 7.13 (m, 8H), 7.07 (d, *J* = 8.0 Hz, 2H), 7.04 – 6.96 (m, 3H), 6.87 (s, 1H), 6.56 (q, *J* = 5.1 Hz, 1H), 4.17 (dddd, *J* = 11.7, 7.2, 4.3, 2.5 Hz, 1H), 4.08 (ddd, *J* = 14.5, 9.8, 6.0 Hz, 1H), 3.83 (ddd, *J* = 14.5, 9.7, 6.6 Hz, 1H), 3.70 (q, *J* = 5.1 Hz, 3H), 3.58 (hept, *J* = 7.1 Hz, 1H), 3.48 – 3.34 (m, 2H), 2.33 (qd, *J* = 14.9, 5.9 Hz, 2H), 1.70 – 1.60 (m, 4H), 1.53 (d, *J* = 7.1 Hz, 6H), 1.38 (s, 3H), 1.34 (s, 3H), 1.32 (t, *J* = 2.5 Hz, 1H), 1.10 (dt, *J* = 12.9, 11.6 Hz, 1H).

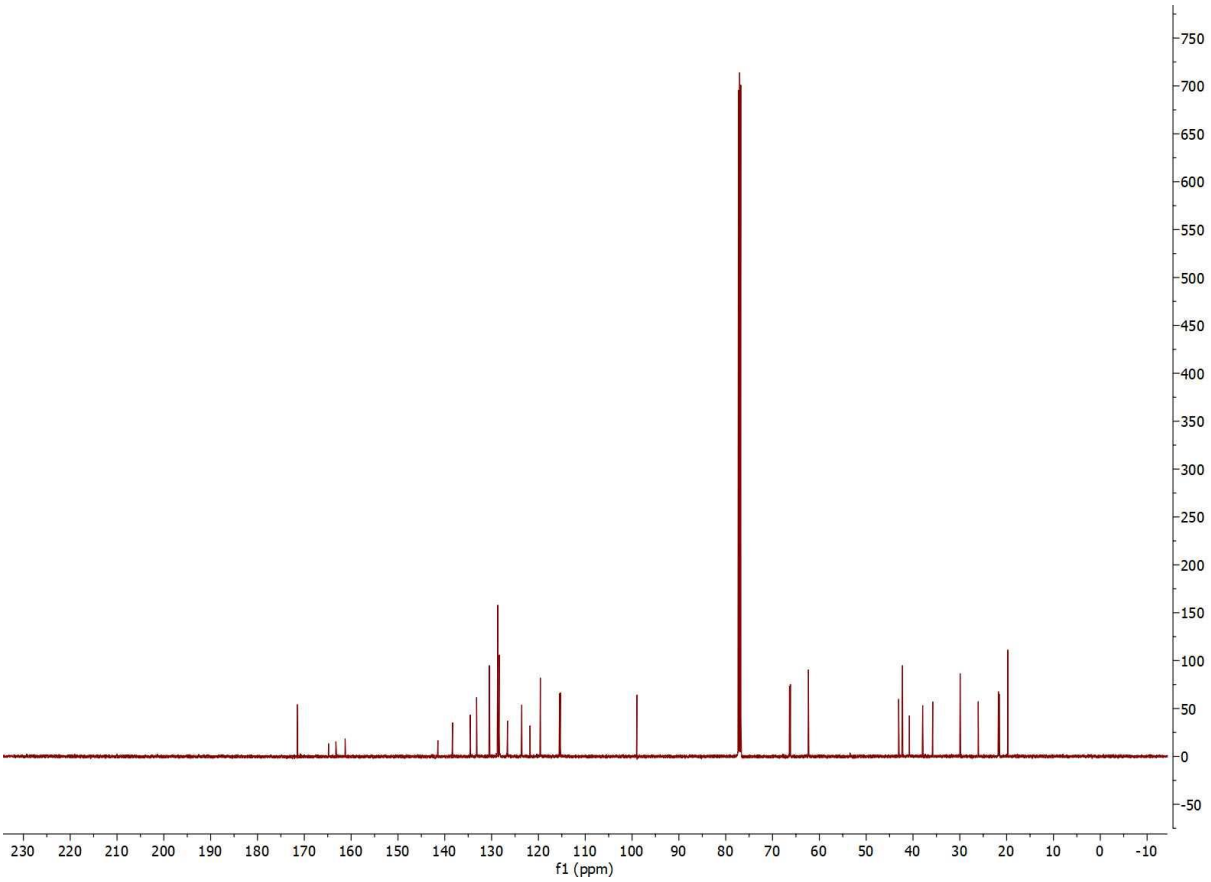

Figure 4-3. C-NMR spectrum of atorvastatin-linker (ATV-linker).

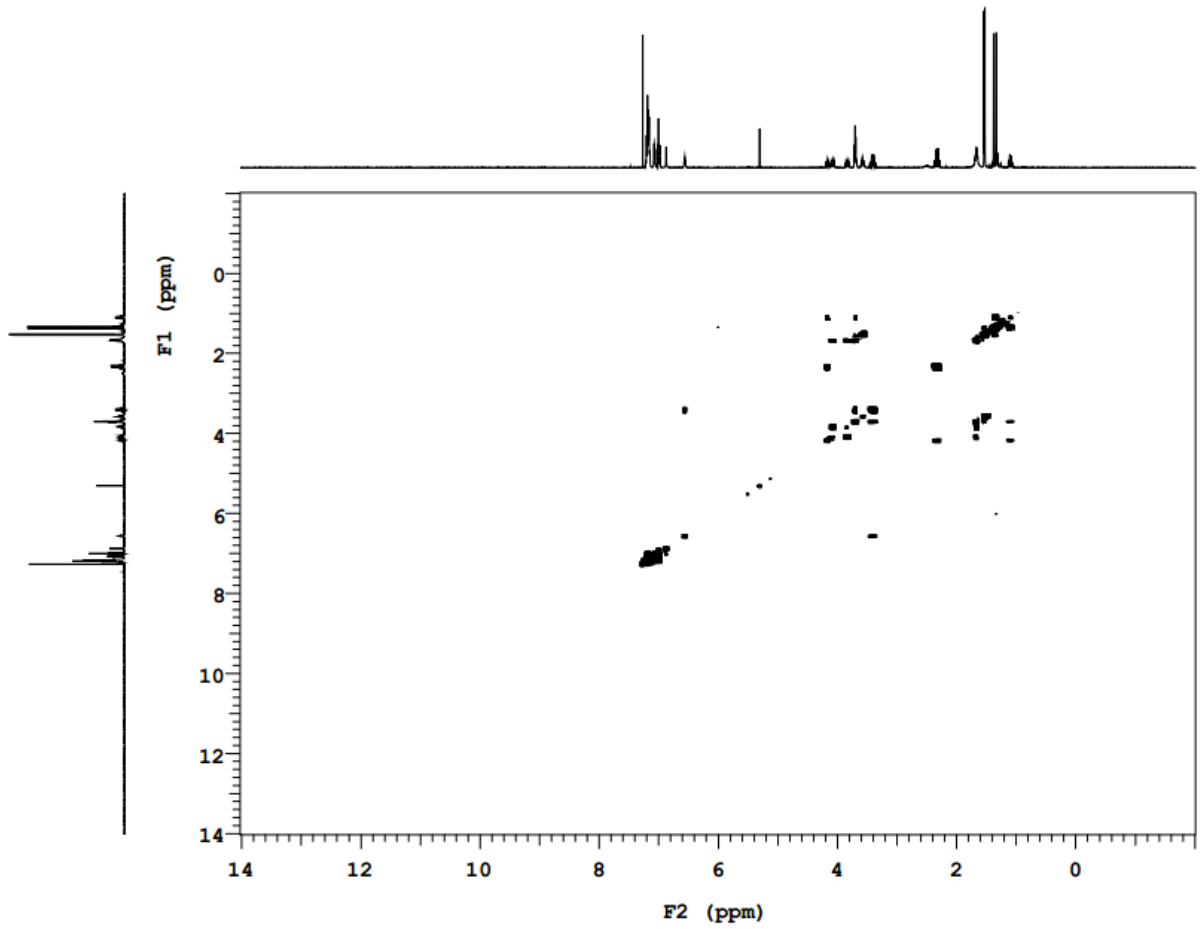

Figure 4-4. G-COSY spectrum of atorvastatin-linker (ATV-linker).

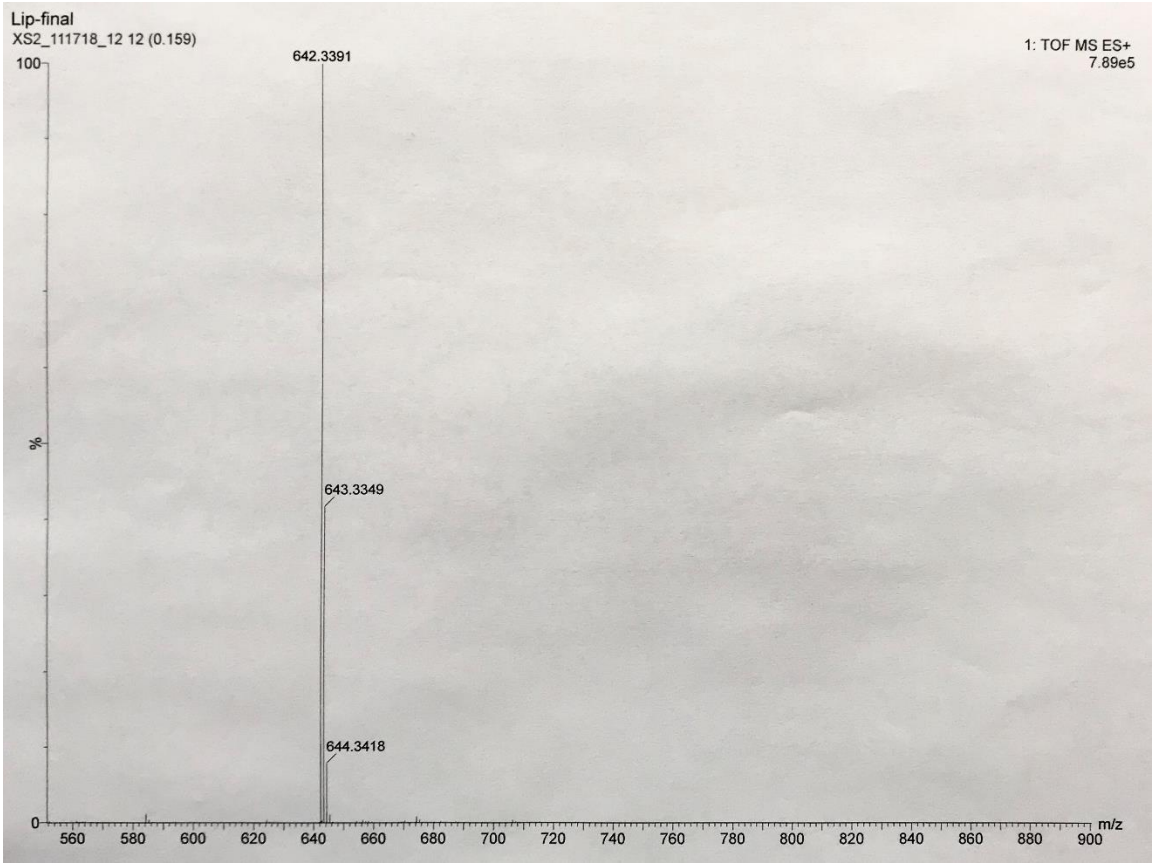

Figure 4-5. ESI mass spectrum for atorvastatin-linker (ATV-linker).

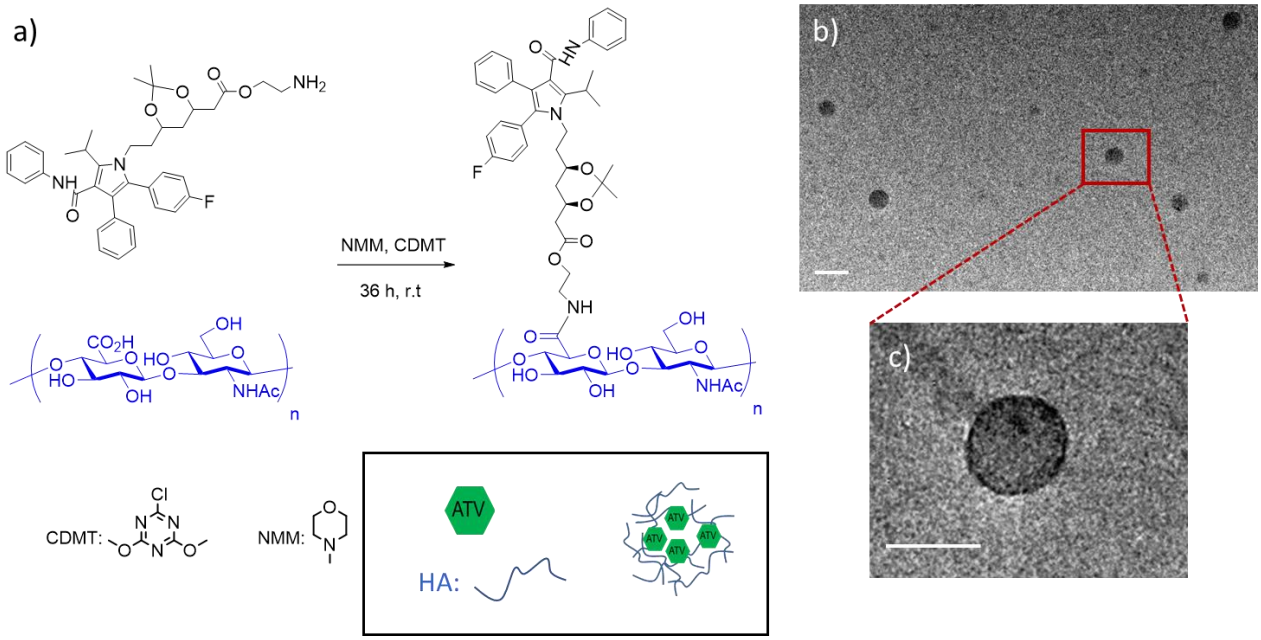

Figure 4-6. Preparation of hyaluronan conjugated atorvastatin nanoparticle (HA-ATV NP). a) conjugation of HA with ATV. (b and c) TEM images of prepared HA-ATV NP in water. Scale bars are 100 and 50 nm respectively.

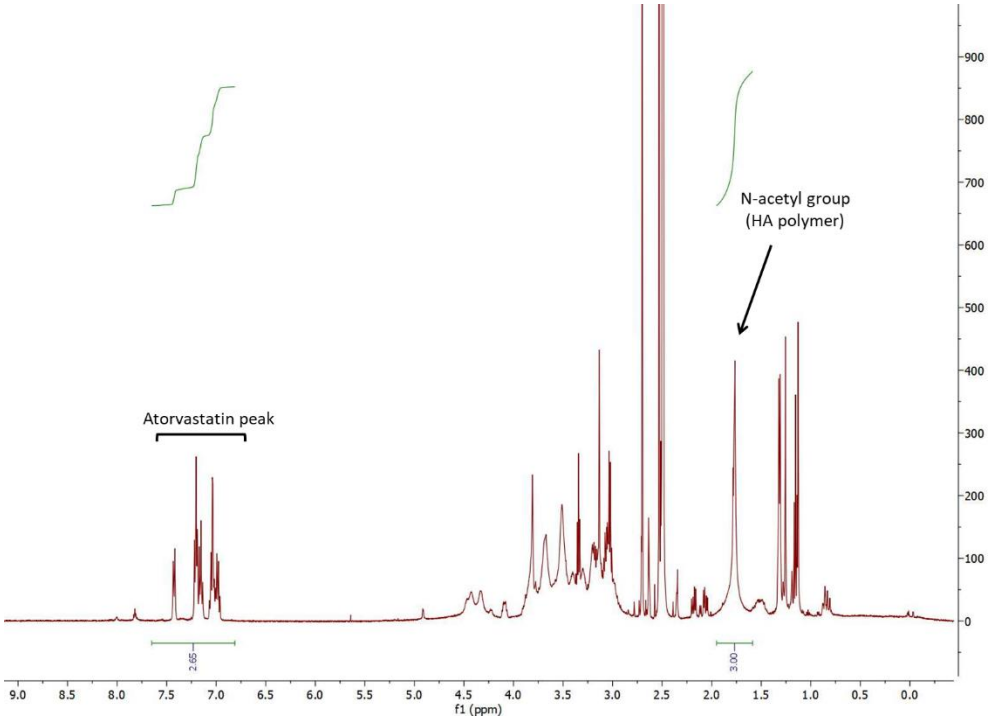

Figure 4-7. H-NMR of HA-ATV conjugate.

Figure 4-8. Agarose gel electrophoresis for free HA and HA-ATV conjugate. Free HA and HA-ATV conjugate were run on agarose gel and stained with Stains-All dye. Free HA has a blue color in this staining and HA-ATV conjugate has shown up purple.

Upon mixing with water, HA-ATV formed NPs due to its amphiphilic nature. The hydrodynamic diameter of HA-ATV NP was 122 nm as determined by dynamic light scattering (DLS). The zeta potential of HA-ATV NP in water was -35 mV, suggesting the presence of negatively charged carboxylic groups on the surface of the HA-ATV NPs. The morphology of the prepared HA-ATV

nanoparticles were also confirmed by TEM imaging indicating they have spherical shape **Figure 4-6b** and **c**. Interestingly, when 1H-NMR of HA-ATV NP was acquired in D_2O, only signals from HA were observed **Figure 4-9**. This is most likely because ATV aggregated in the core of HA-ATV NP, resulting in significant signal broadening in NMR. Lowering the amount of ATV to HA polymer backbone (1:10) led to increased hydrodynamic diameter (286 nm) probably due to the lower hydrophobicity of core in self-assembled nanoparticles.

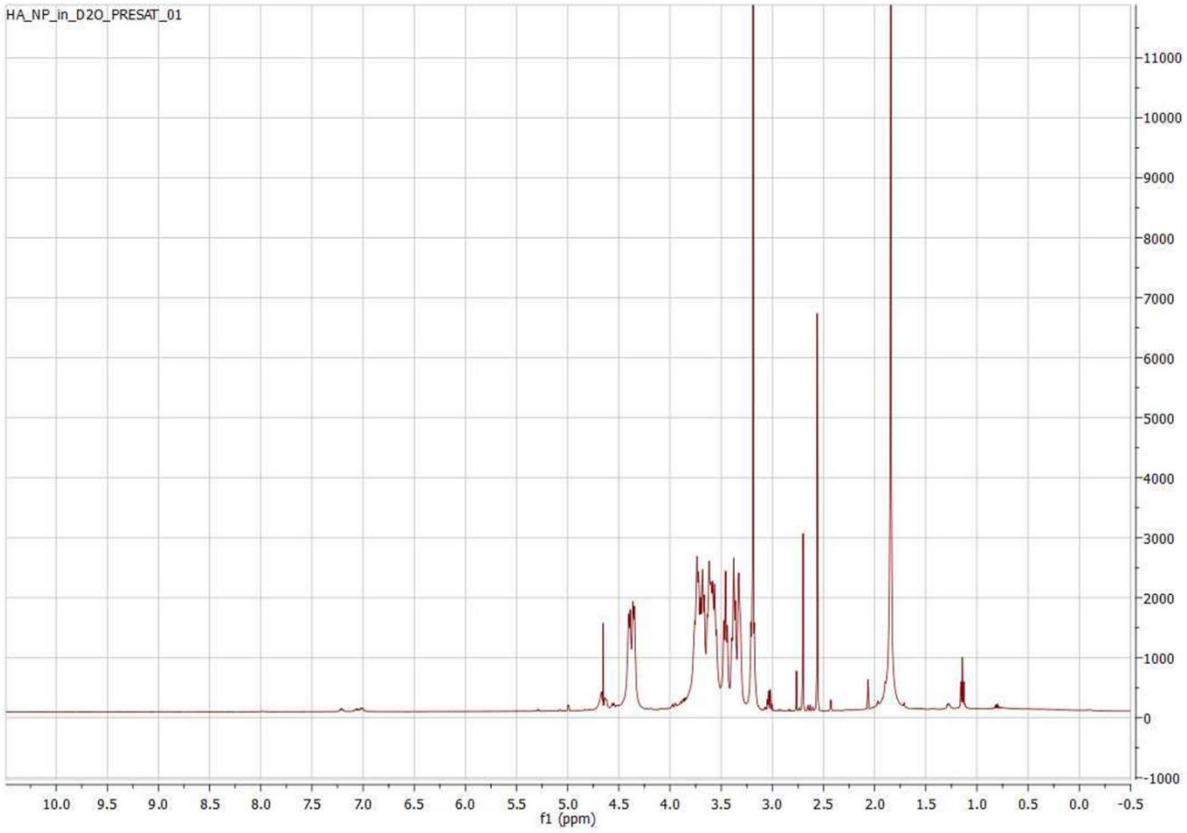

Figure 4-9. ^{1}H-NMR spectrum for HA-ATV conjugate in D_2O. ATV Peaks are almost absent presumably due to aggregation of ATV in the core of HA-ATV NP.

4.3. HA-ATV NP Retained the Ability to Bind with CD44 Receptor

The abilities of HA-ATV NP to bind with CD44 were analyzed next using a competitive ELISA. In this experiment, biotinated HA bound with CD44 immobilized in ELISA wells, to which

increasing concentrations of HA-ATV NPs were then added. If HA-ATV NP could bind with CD44, it would displace biotinated HA from CD44 resulting in reduced ELISA signals. As shown in **Figure 4-10**, HA-ATV NPs exhibited dose dependent inhibition of biotinated HA binding with CD44 with an apparent EC50 value of 3.5 ug/mL. This indicates that HA-ATV NPs retain the ability of HA to bind with CD44.

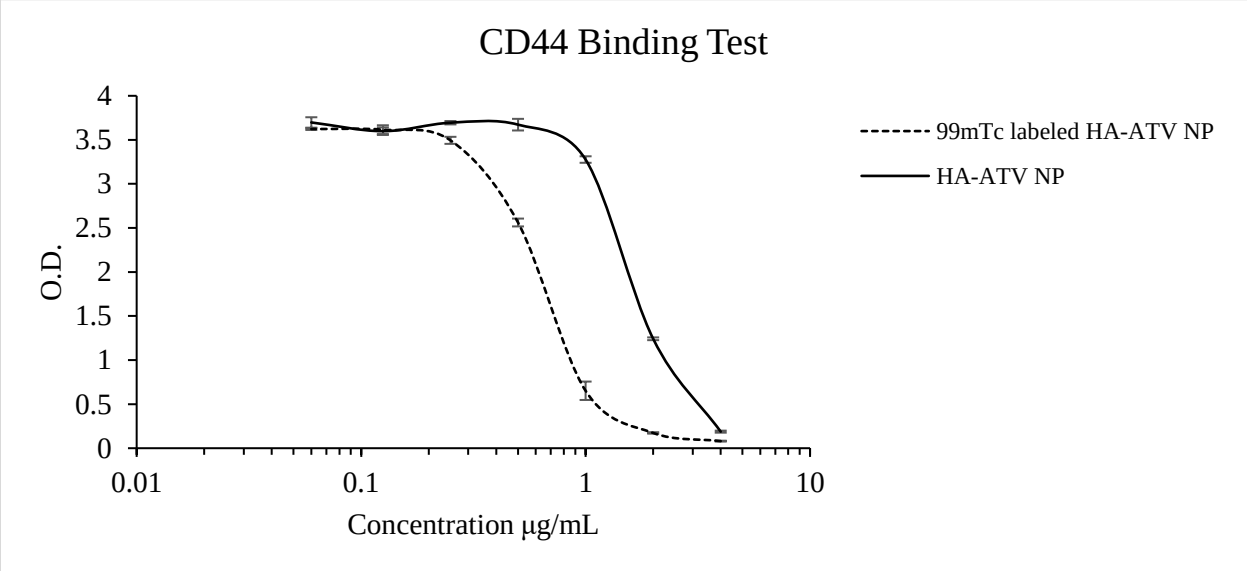

Figure 4-10. ELISA Experiment Confirmed CD44 Binding Ability of HA-ATV NP and ^{99m}Tc HA-ATV NP.

4.4. HA-ATV NP Could be Taken Up by Macrophages in An Energy Dependent Manner

With the ability of HA-ATV NP to bind with CD44 established, their interactions with CD44 expressing mouse macrophages were investigated. HA-ATV NPs were labeled with the fluorophore fluorescein isothiocyanate (FITC), incubated with macrophage RAW264.7 cells and analyzed by flow cytometry. Dose dependent increase of cellular uptake was observed **Figure 4-11**. The level of cellular uptake was much higher at 37 ^{o}C vs that at 4 ^{o}C, suggesting the interactions with RAW264.7 cells were energy dependent. Confocal microscopy of cells following

incubation with FITC labelled HA-ATV NP showed strong green fluorescent signals inside the cells. The green fluorescence was mainly in the cytoplasm and co-localized well with the red fluorescence from lysotracker, indicating internalization of NPs and their accumulation in the cytoplasm **Figure 4-12**.

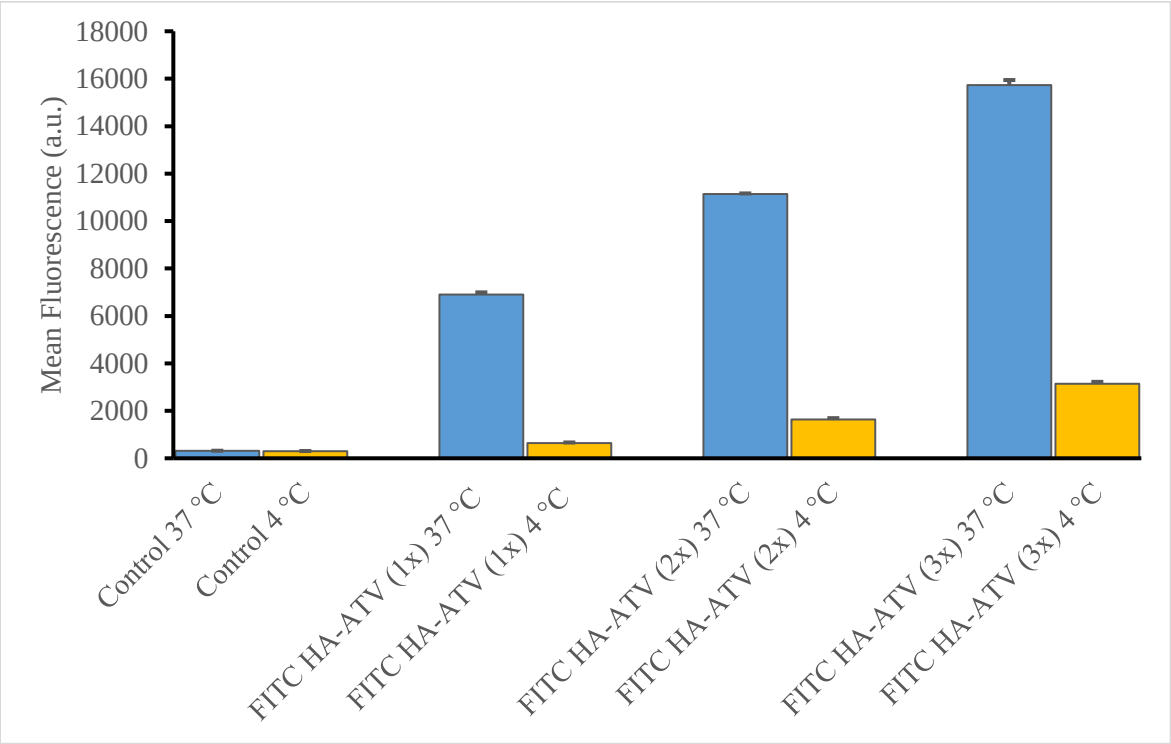

Figure 4-11. Cellular uptake of FITC HA-ATV NP. Cellular uptake of FITC HA-ATV NP is dose and energy dependent. FACS analysis of RAW264.7 cells after incubation with increasing doses of FITC HA-ATV NP at 37 ºC and 4 ºC.

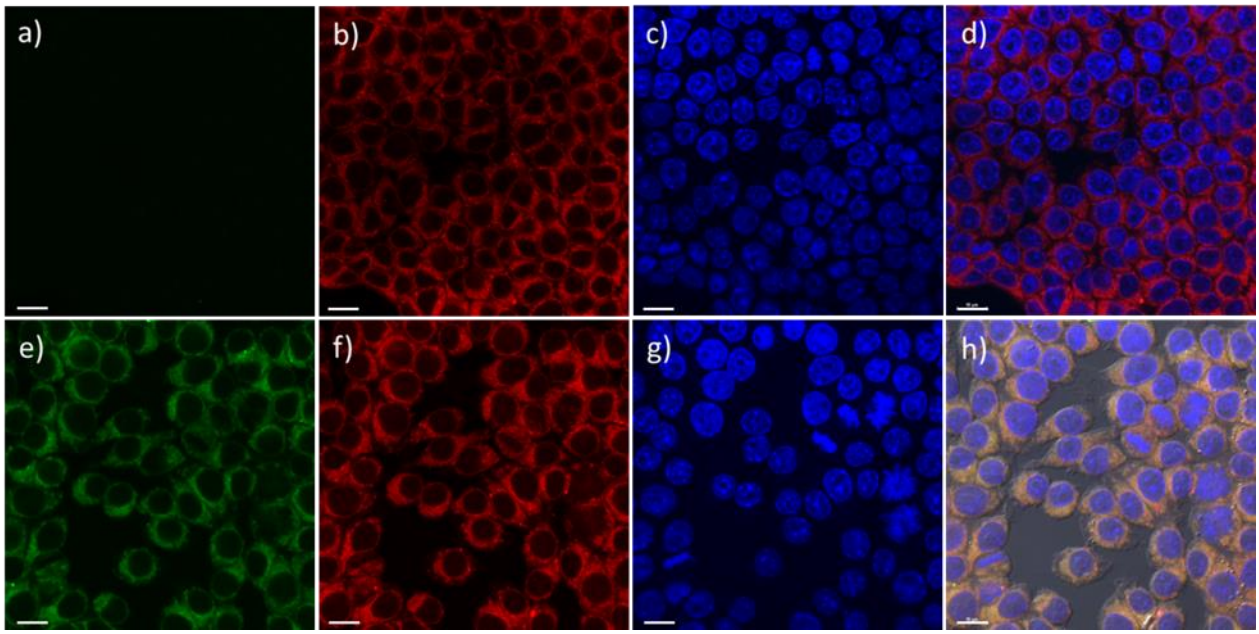

Figure 4-12. Confocal microscopy of RAW264.7 cells indicates FITC HA-ATV NP ends up in cellular cytoplasm. (a-d) shows control group of RAW264.7 cells and (e-h) are RAW264.7 cells images after incubation with FITC HA-ATV NP. FITC, Red Lysotracker and DAPI are respectively (a,e), (b,f) and (c,g). (d and h) are overlays of FITC, Red Lysotracker and DAPI channels. Scale bars are 10 μm.

To directly detect ATV inside the cells, HA-ATV NPs were irradiated by UV (λmax = 254 nm), which is known to result in a shift of ATV emission maximum from 350 nm into blue region 430 nm due to intramolecular photocyclization and formation of phenanthrene ring in ATV **Figure 4-13**.

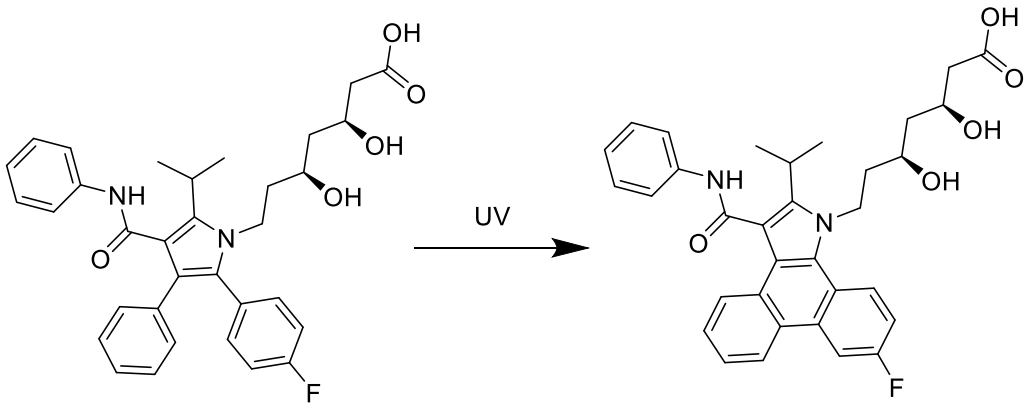

Figure 4-13. Formation of phenanthrene ring in ATV after UV irradiation.

RAW264.7 cells were imaged after treatment with UV irradiated HA-ATV NPs. Strong blue fluorescence was observed in the cytoplasm compared to non-treated cells following confocal imaging of samples confirming that ATV cargo was successfully delivered inside the cells (**Figure 4-14**).

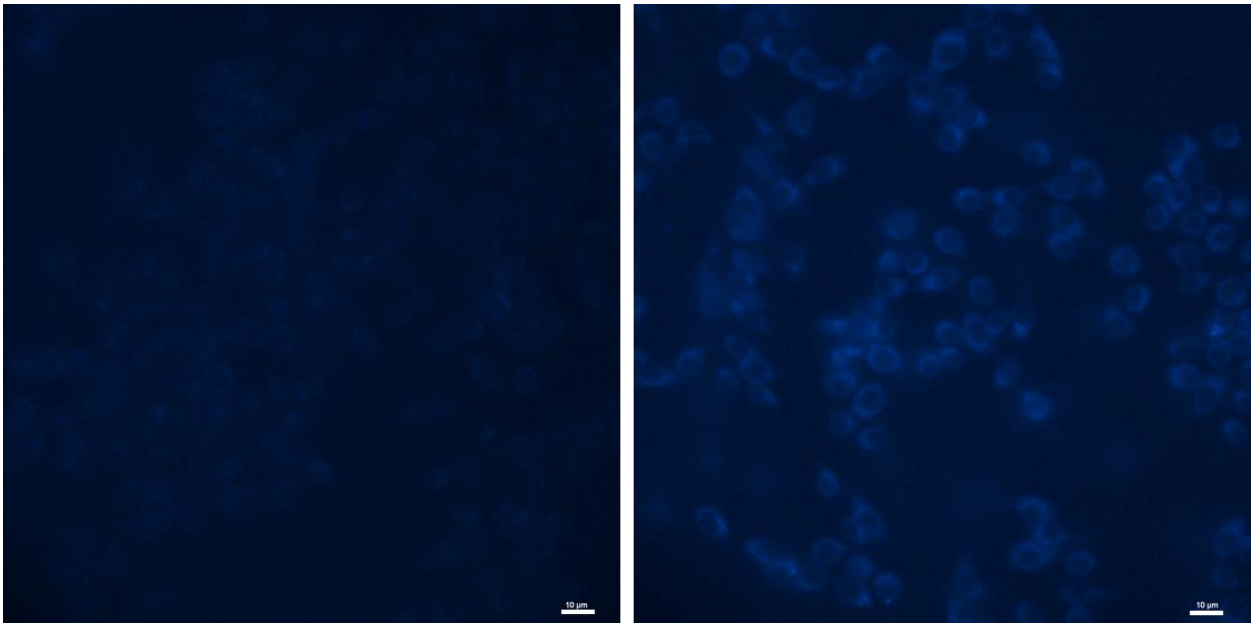

Figure 4-14. Confocal imaging of atorvastatin in RAW264.7 cells. RAW264.7 cells had been incubated with UV irradiated HA-ATV NP and images were collected by confocal microscopy (right image). Control study showing RAW264.7 cells image (left image). The significant increase in blue color (right image) indicates the presence of ATV in the cells. Scale bars are 10 μm.

4.5. HA is Necessary for Cellular Uptake of HA-ATV NP and CD44 Plays an Important Role for Cellular Interaction of HA-ATV NP

To better understand HA-ATV NP interaction with macrophages, RAW264.7 cells were incubated with FITC labeled HA-ATV NP in the presence of free HA. Free HA significantly reduced the levels of HA-ATV NP binding with the cells (91% at 37 ^{o}C and 100% at 4 ^{o}C) **Figure 4-15** suggesting the interactions were HA dependent. Furthermore, pretreatment of RAW264.7 cells with an anti-CD44 monoclonal antibody KM81 caused a 50% reduction of the cellular interactions with HA-ATV NP **Figure 4-16**. This is consistent with the idea that CD44 plays important roles in NP interactions with macrophages.

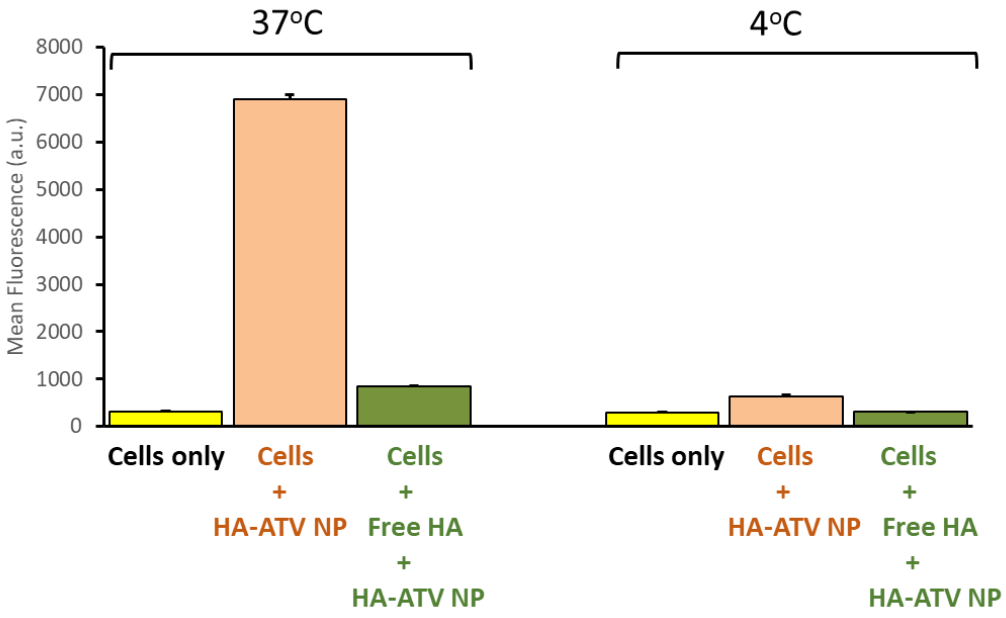

Figure 4-15. Cellular interaction with HA-ATV NP is HA dependent. Treatment of RAW264.7 cells with free HA significantly reduced cellular uptake of HA-ATV NP when evaluated with FACS analysis.

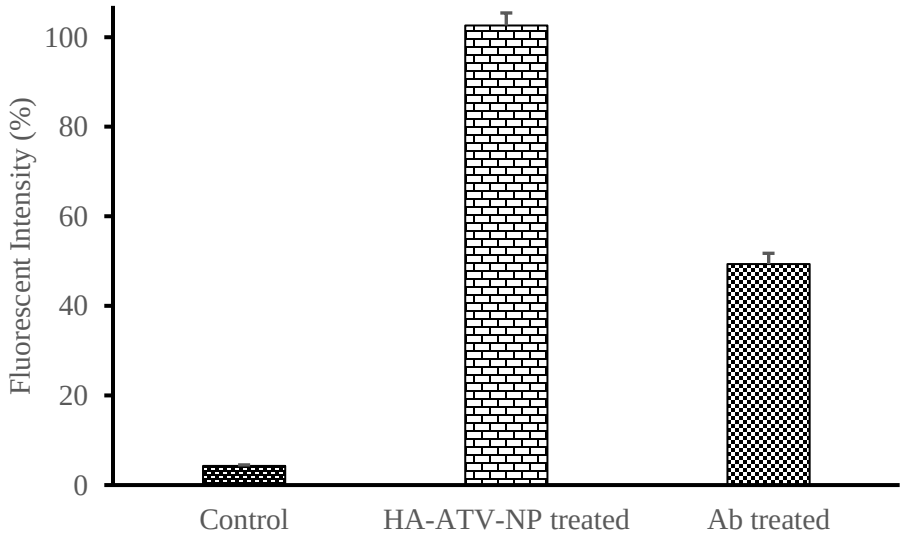

Figure 4-16. Cellular interaction with HA-ATV NP is CD44 dependent. Blocking CD44 receptor using [KM81] monoclonal antibody reduced 50% of HA-ATV NP cellular interaction.

4.6. HA-ATV NP Reduces the Expression Levels of Inflammatory Genes from Macrophages in Vitro

With the establishment of binding and uptake of HA-ATV NPs by macrophages, their impacts on inflammatory activities were analyzed. RAW264.7 cells were incubated with HA-ATV NPs followed by lipopolysaccharide (LPS). Control cells received free form of ATV rather than HA-ATV at equivalent ATV dose. The expression levels of inflammatory genes in the cells were then quantified by RT-PCR. LPS is known to stimulate inflammation, leading to the production of a wide range of molecules associated with inflammation including TNFα, IL-1β, IL-1α and ICAM-1 from RAW264.7 cells. Interestingly, while free ATV did not have decrease the levels of inflammatory molecules from RAW264.7 cells under the experimental conditions, HA-ATV NPs reduced TNFα, IL-1β, IL-1α and ICAM-1 levels by 45%, 81%, 65% and 95% respectively **Figure 4-17**. Furthermore, inflammatory cytokines can induce the production of inducible nitric oxide synthase (iNOS)[22], contributing to the inflammatory process of plaque development[23]. Inhibition of iNOS can mitigate atherosclerosis through impairing foam cell migration and cholesterol influx[24-25]. A 55% reduction in expression of iNOS from RAW264.7 cells was observed following incubation with HA-ATV NP **Figure 4-19**, while free ATV did not have much an effect **Figure 4-18**. In addition, when RAW264.7 cells were treated with free HA, there were no reductions of inflammatory activities highlighting the importance of having both HA and ATV. The superior in vitro anti-inflammatory activities of HA-ATV NP set the stage for *in vivo* evaluations.

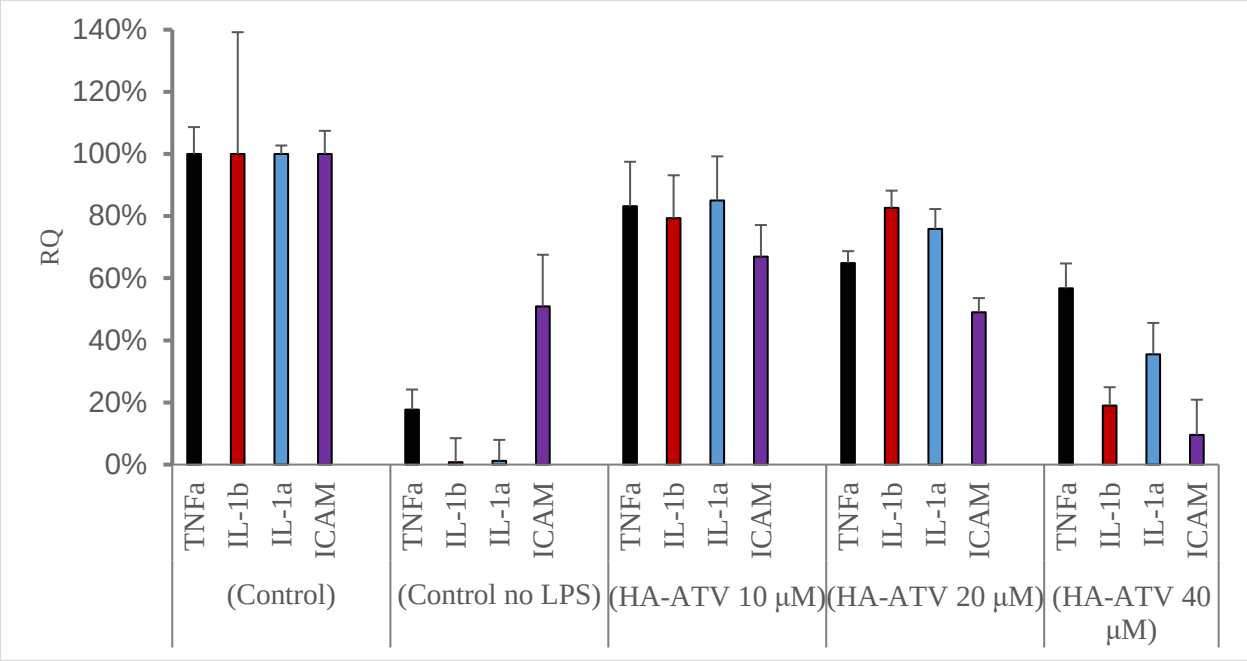

Figure 4-17. Reduction of inflammatory gene expression levels in RAW264.7 cells following treatment with HA-ATV NP. Cells were treated with HA-ATV NP and LPS, then mRNA expression levels were quantified using rt-PCR. Control group is RAW264.7 cells plus LPS and negative control (Control no LPS) are RAW264.7 cells with no LPS treatment.

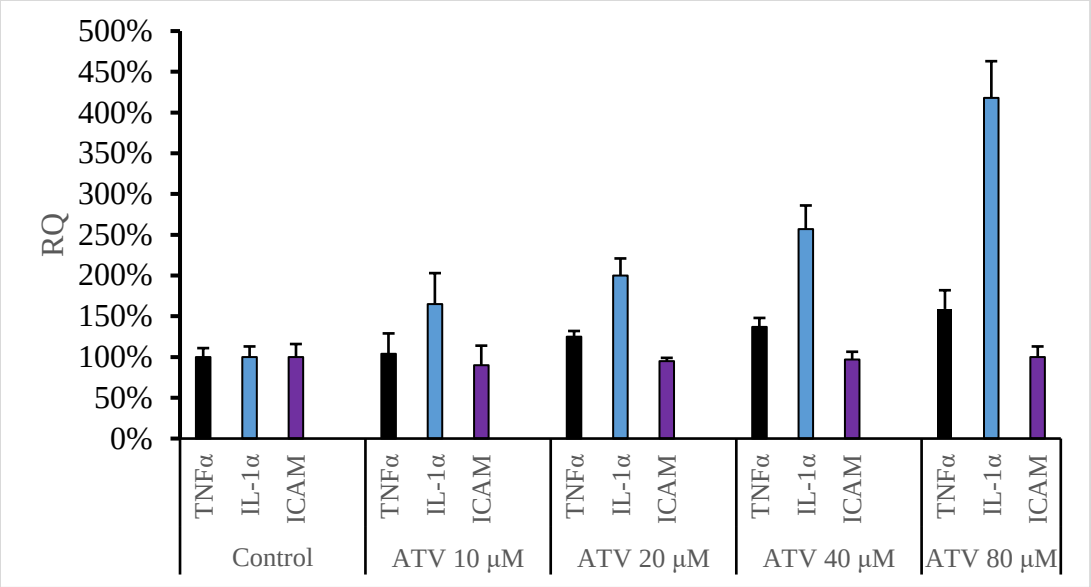

Figure 4-18. rt-PCR analysis of RAW264.7 cells treated with atorvastatin. Incubation of RAW264.7 cells with atorvastatin did not show anti-inflammatory effect. RAW264.7 cells were treated with increasing doses of atorvastatin for 15 hours and LPS was added for another 4 hours. The expression level of inflammatory genes was analyzed using rt-PCR.

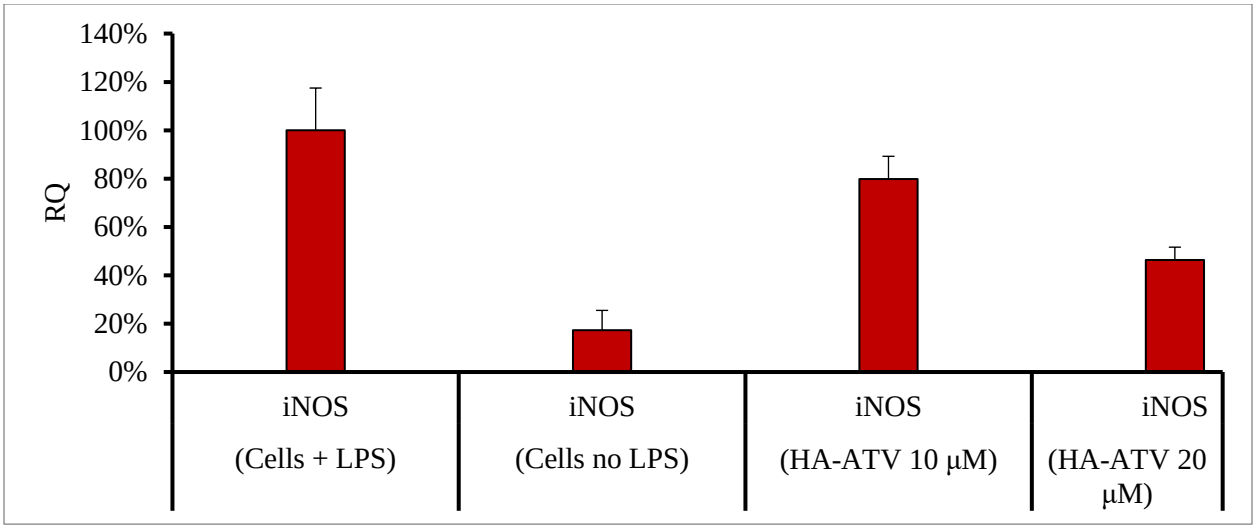

Figure 4-19. HA-ATV NP decreases the expression level of iNOS in LPS treated RAW264.7 cells. Control group is RAW264.7 cells plus LPS and negative control (Control no LPS) are RAW264.7 cells with no LPS treatment.

4.7. HA-ATV NP Could Decrease Atherosclerotic Plaque Inflammation in ApoE Knockout Mouse Model

ApoE knockout mice are a clinically relevant model of atherosclerosis, as these mice spontaneously develop atherosclerotic plaques which can be accelerated with a high fat diet[26]. Previously, we developed HA coated magnetic nanoworms, which could aid in the non-invasive detection of inflammatory atherosclerotic plaques by magnetic resonance imaging (MRI)[18]. To test the efficacy of HA-ATV NP for atherosclerosis treatment, groups of ApoE knockout mice were fed with a high fat diet, and then subjected to HA-nanoworm aided MRI. Consistent with our prior studies, six weeks after being on the high fat diet, ApoE knockout mice showed extensive signal loss on their aorta walls in the HA nanoworm aided T_2* weighted MRI indicating the development of inflammatory atherosclerotic plaques. These mice were then treated with HA-ATV NPs (4 intravenous injections every other day at the dose of 8.5 mg ATV/Kg body weight) and imaged

again by MRI. Interestingly, in contrast to untreated mice, T_2* weighted images of aorta walls of HA-ATV treated mice no longer exhibited any signal loss suggesting greatly reduced accumulation of HA-nanoworms at plaque sites **Figure 4-20**. This in turn indicates that HA-ATV NP treatment significantly decreased the degree of inflammation.

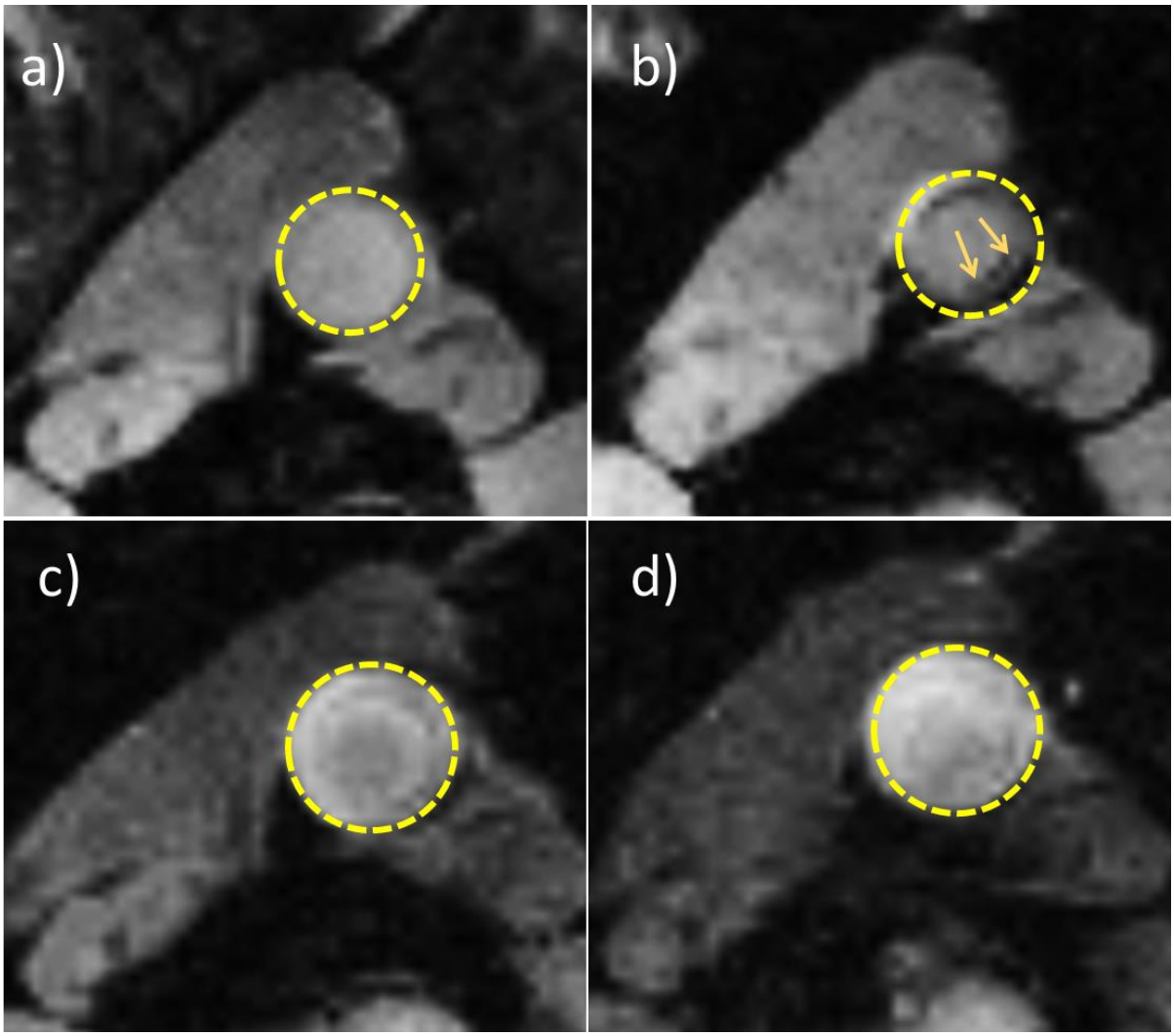

Figure 4-20. Atherosclerotic plaques were not detectable by MRI after HA-ATV NP treatment. (a) and (b) are ApoE knockout mouse aorta 6 weeks after high fat diet. (a) and (b) are MRI images before and after HA-NW injection, respectively. Arrows show the presence of plaques. (c) and (d)

Figure 4-20 (cont'd) are MRI images one week later after receiving HA-ATV NP. (c) and (d) are MRI images before and after injection of MRI probe (HA-NW) respectively.

In order to confirm the observation in MRI, ApoE knockout mice were sacrificed following HA-ATV NP treatment, and their aortas were extracted for histological studies **Figure 4-21c** and **f**. Another group of age matched mice were administered pharmaceutical grade ATV via oral garage with the same dose of ATV and schedule as HA-ATV. F4/80 staining showed significant reduction in macrophage content of plaques in HA-ATV treated group compared to ATV group or untreated control **Figure 4-21c** vs **b** and **a**. Similar reduction in CD44 levels at plaques was observed in HA-ATV treated group **Figure 4-21f** vs **e** and **d**. Moreover, the areas of plaque were quantified, which showed 69% reduction in treated group compared to non-treated control group **Figure 4-22**.

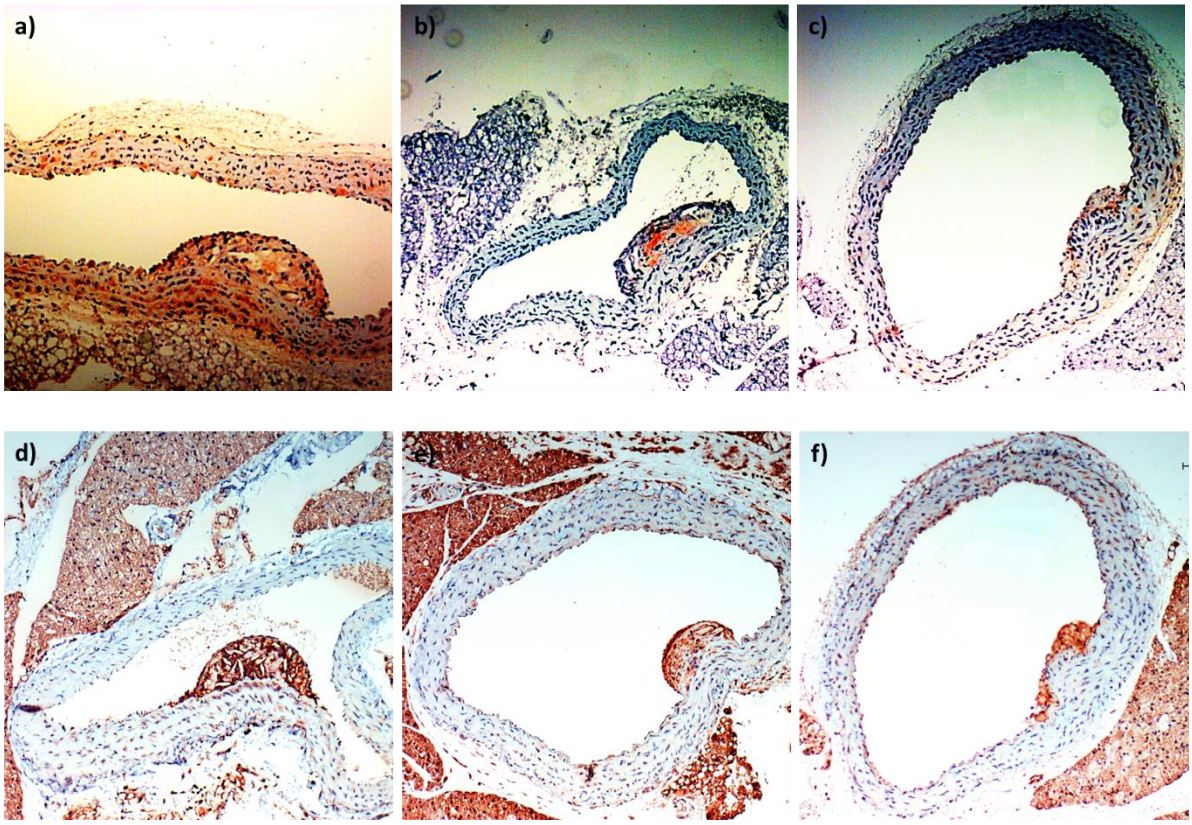

Figure 4-21. Histology study shows macrophage and CD44 reduction after HA-ATV NP treatment. F4/80 staining shows the presence of macrophage in atherosclerotic plaques in control ApoE knockout mouse aorta (a), ATV treated ApoE knockout mouse aorta (b) and HA-ATV treated ApoE knockout mouse aorta(c). CD44 staining shows the expression of CD44 receptor in atherosclerotic plaques in control ApoE knockout mouse aorta (d), ATV treated ApoE knockout mouse aorta (e) and HA-ATV treated ApoE knockout mouse aorta(f).

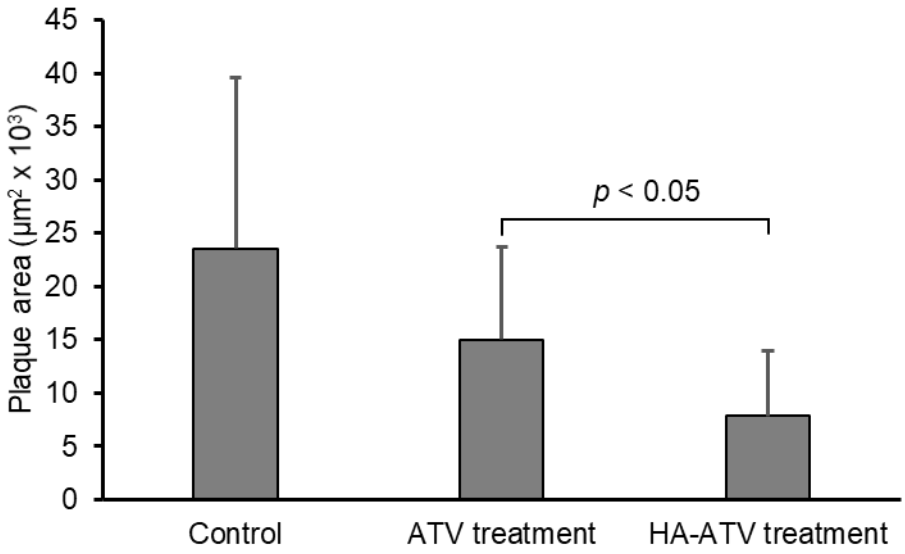

Figure 4-22. Plaque area quantification showed significant reduction in ApoE knockout mice group that received HA-ATV NP. ImageJ was used for plaque area measurement.

4.8. Biodistribution Study for HA-ATV NP

To analyze the biodistribution of HA-ATV NP in mice, ^{99m}Tc labeled HA-ATV NPs were synthesized with the metal chelator DTPA and incubated with ^{99m}Tc. The resulting ^{99m}Tc HA-ATV NPs retained their abilities to bind with CD44 as confirmed by ELISA. ApoE knockout mice as well as normal mice were injected with ^{99m}Tc HA-ATV NPs intravenously. Two hours after the injections, mice were sacrificed, and their organs were extracted to quantify the levels of radioactivity using a gamma counter. The highest uptake was observed in reticuloendothelial system organs such as liver and spleen **Figure 4-23**. About 1.7% of injected dose of HA-ATV NP was found in aortas, which was higher than those found in aortas of normal mice (1.1%).

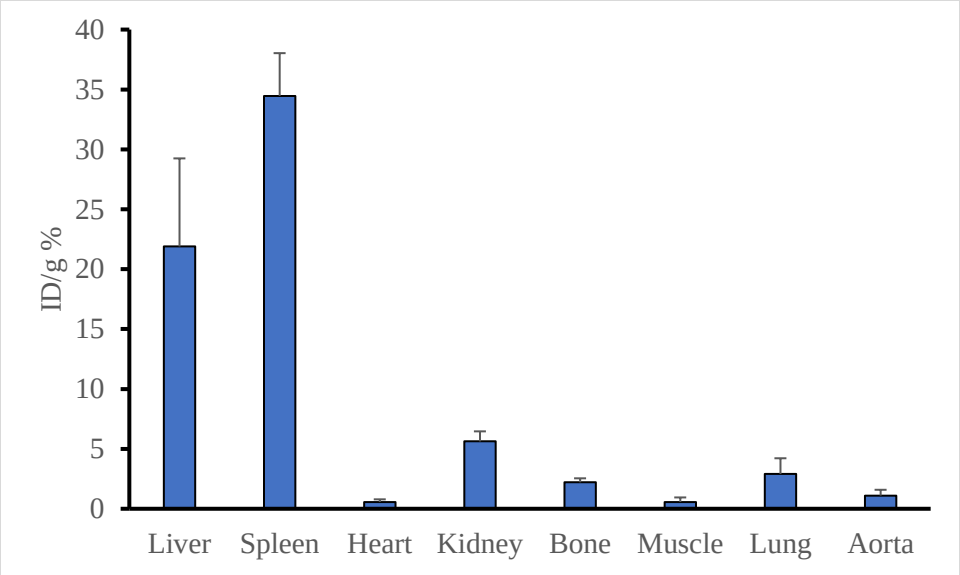

Figure 4-23. Biodistribution study of HA-ATV NP. Mice were injected with ^{99m}Tc labeled HA-ATV NP and organs radioactivity have been presented based on injected dose per gram animal tissue. Spleen and liver showed the highest uptake.

4.9. Discussion

In this work, HA-ATV conjugate has been synthesized through an ester bond between ATV and HA polymer backbone. This conjugate can self-assemble into HA-ATV NPs in water presumably by hydrophobic core formation through ATV moieties surrounded by the hydrophilic HA polymer. The NPs can be cleaved through enzymatic and acid promoted hydrolysis to release the active compound ATV. In addition, the conjugation chemistry allowed the tuning of ATV/HA ratio. The ratio of 4:10 (ATV/HA) has been used for cellular and animal studies corresponding to 35% of total mass of conjugate as the active drug. This is significantly higher than the typical cargo loading level of HA magnetic nanoparticles for drug delivery (2.1% w/w of the cargo). Thus, utilizing ATV as the hydrophobic core markedly increased the amount of drug per particle with the covalent linkage between ATV and HA mitigating the concern of premature drug leakage.

HA-ATV NPs retained their CD44 binding property as evident from the competitive ELISA results **Figure 4-10**. The interactions of HA-ATV NPs with RAW264.7 cells were shown to be almost entirely HA dependent as HA can block cellular uptake of HA-ATV NP. Pre-incubation of RAW264.7 cells with an anti-CD44 mAb reduced 50% of the cellular interaction, which is consistent with the idea that the cellular interactions of HA-ATV NP are at least partially mediated by CD44. Cellular interactions of HA-ATV were significantly reduced at 4 ^{o}C vs 37 ^{o}C suggesting HA-ATV NPs enter the cells through energy dependent endocytosis mechanisms.

A key finding of our study is that the HA-ATV NP treatment of macrophage cells in vitro effectively inhibited inflammatory responses induced by LPS. High molecular weight HA has been shown to exhibit anti-inflammatory activities. However, the activities of HA-ATV NP were likely not due to HA since free HA was not active under the same condition as HA-ATV NP. Interestingly, at the same dose, free ATV did not exhibit much anti-inflammatory function either. Thus, it is critical to conjugate ATV with HA to suppress macrophage inflammatory responses.

Recruitment of inflammatory cells is a key process in atherosclerosis development, which CD44 plays an important role. While CD44 is also present on cell surface under normal physiological conditions, it mainly exists in a low HA affinity state. During inflammation, the presence of inflammatory signals such as TNF-α induces sulfation of CD44, leading to conformational changes of the protein and resulting in its switch to high affinity state for HA binding[27]. The binding of HA with CD44 on macrophages leads to the trafficking of macrophages to plaques, which exacerbates inflammation in plaque sites. The HA-ATV-NP can mimic this process by binding with CD44. This enables selective accumulation of NPs in plaques, and delivery of ATV to plaque sites.

An atherosclerosis mouse model was established with ApoE knockout mice. To monitor inflammation in plaques *in vivo*, mice were imaged by MRI aided by HA coated magnetic

nanoworms. Upon feeding with a high fat diet for six weeks, mouse aortas exhibited significant signal loss in T_2* weighted MRI suggesting marked inflammation in aorta walls. Following one-week treatment with HA-ATV NP, the MRI signal changes were no longer observed indicating the reduction of CD44 levels. Histology analysis of treated mice confirmed that HA-ATV NPs led to drastic reduction of inflammation as reflected by significant decreases of macrophage content, CD44 level and sizes of the plaques, which supported the observations in MRI. The therapeutic effect was more pronounced with HA-ATV NPs than free ATV at the equivalent ATV dose. These results highlight that even with a relatively short one-week treatment regimen, significant benefits could be obtained using HA-ATV NPs. At the same time, our results confirmed that HA nanoworms could be a useful non-invasive method to monitor efficacy of atherosclerosis treatment.

In general, drug delivery can be performed through either passive (diffusion of drugs into the desired site) or active targeting (binding with receptors present in plaques)[28-29]. Active targeting can potentially improve the organ selectivity, enhance the percentage of drugs reaching plaque sites, and lower the dose needed[30]. A common strategy to actively target atherosclerotic plaques is to mimic the naturally existing HDL particles, as they are known to interact with atherosclerotic plaques through ApoA-1 binding with various receptors such as ABCA1, ABCG1, ecto-F1-ATPase and scavenger receptor B1 (SR-B1)[31-32]. HDL NPs encapsulating simvastatin have been constructed, which can deliver simvastatin to plaques to achieve local anti-inflammatory effects[33]. Compared to the untreated group, HDL-simvastatin NP at 60 mg kg^{-1} statin dose on one-week treatment regimen reduced plaque sizes as well as levels of inflammatory markers. While these studies demonstrated the effectiveness and feasibility of statin delivery for local inflammation reduction, the relatively high cost of production with HDL demonstrates other NP systems should

be explored. With our HA-ATV NPs, we achieved superior *in vivo* efficacy compared to free ATV with the readily available HA (~ $100/g) for NP construction.

High dose short term regimen of statin therapy to reduce plaque inflammation recently has got attention. It seems that this regimen is not going to be limited for statins[34] and other anti-inflammatory therapeutics are going to be investigated for this purpose[35].

4.10. Conclusion

In conclusion, we have synthesized a new type of NPs (HA-ATV NP) capable of delivering a large quantity of ATV per particle. The HA-ATV NPs can target inflammatory atherosclerotic plaques through targeting CD44 receptor and release its payload there. In addition, the NPs exhibited anti-inflammatory effects to macrophages in vitro and reduced atherosclerotic plaque inflammation *in vivo* in ApoE knockout mice model when administered during one-week treatment. Thus, with the high accessibility of HA and ATV, HA-ATV NP is an excellent candidate for the treatment of inflammatory atherosclerotic plaques.

4.11. Experimental

4.11.1. Materials

Dimethylsulfoxide (DMSO), formalin solution neutral buffered 10%, fetal bovine serum (FBS), Dulbecco's phosphate buffered saline (DPBS), Dulbecco's Modified Eagle Medium (DMEM), anti-CD44 antibody [MEM-85] and Amberlite® IR 120 hydrogen form (Amberlite H^+) were purchased from Sigma-Aldrich. Goat anti human IgG FC γ and centrifugal filter MWCO (10 kDa) were purchased from EMD Millipore. 2-Chloro-4,6-dimethoxy-1,3,5-triazine (CDMT) and N-methylmorpholine (NMM) were purchased form Acros Organics. Sodium hyaluronan (30 kDa)

was obtained from Lifecore Biomedicals. Fluorescein isothiocyanate (FITC), 4′,6-diamidino-2-phenylindole (DAPI), LysoTracker-594 DND and TURBO DNA-free™ Kit were purchased from Invitrogen. Penicillin-Streptomycin (Pen Strep) mixture, trypsin-EDTA (0.5%), Power SYBR® Green PCR Master Mix and L-glutamine were obtained from Thermo-Fisher. Recombinant human CD44 Fc chimera protein was ordered from R&D Systems®. RNeasy® Mini Kit was ordered from QIAGEN®. dNTP Mix, GoScript™ Reverse Transcriptase, Random Primers and CellTiter 96 Aqueous One solution containing 3-(4,5-dimethylthiazol-2-yl)-5-(3-carboxy-methoxyphenyl)-2-(4-sulfophenyl)-2H-tetrazolium (MTS) were purchased from Promega. S-2-(4-Isothiocyanatobenzyl)-diethylenetriamine pentaacetic acid (p-SCN-Bn-DTPA) was ordered from Macrocyclics™. Anti-CD44 antibody [KM81] and polyclonal rabbit anti-CD44 antibody were purchased from Abcam. Pyridine p-toluenesulfonate, 2,4,6-trimethylbenzoyl chloride, 4-(dimethylamino) pyridine, 4-methylmorpholine, 2-chloro-4,6-dimethoxy-1,3,5-triazine, H_2/Pd/C, lipopolysaccharide and N,N-dimethylformamide were ordered from Sigma. Rat anti-F4/80 antibody was purchased from Biorad. Atorvastatin was ordered from AstaTech Inc.

4.11.2. Synthesis of HA-ATV NP

Atorvastatin calcium salt (1g) was dissolved in DMF (15 mL) then 2 eq. of potassium carbonate and 2 eq of benzyl bromide were added and stirred for 3 hours at room temperature. Then, the reaction mixture was diluted with ethyl acetate and it was washed by sodium chloride solution. The product was purified by running a silica column (**1**). Thereafter, it was dissolved in DMF and 50 eq. of 2,2-dimethoxypropane and 1 eq. of pyridine p-toluenesulfonate (PPTS) were added and stirred for 8 hours at room temperature and the product was purified on column (**2**). Next, benzyl group was removed through catalytic hydrogenation in methanol/dichloromethane (2:1) solution (**3**). Subsequently, a linker (N-protected ethanolamine) was introduced into the diol protected

atorvastatin through an ester bond formation as follows: 1 eq. of (**3**) was dissolved in anhydrous acetonitrile, triethylamine (1 eq.), 2,4,6-trimethylbenzoyl chloride (1.2 eq.) and 4-(dimethylamino) pyridine (1 eq.) were added. Next, 1.2 eq. of N-protected ethanolamine was dissolved in anhydrous tetrahydrofuran and stirred for 1 hour. The reaction mixture was quenched using one drop of water and the product was purified by running a silica column (**4**). Finally, amine group was deprotected using catalytic hydrogenation in a mixture of methanol/dichloromethane (1:1) (**5**).

To prepare HA-ATV conjugate, HA was first protonated[36], then dissolved in a mixture of water/acetonitrile (3:2). Subsequently, 4-methylmorpholine (1.2 eq.) and 2-chloro-4,6-dimethoxy-1,3,5-triazine (0.4 eq) were added and stirred for 30 minutes. Then, ATV-linker (0.4 eq) (5) was dissolved in a mixture of acetonitrile/DMSO (1:3) and added to HA solution and stirred for 36 hours at room temperature. Next, the reaction mixture was transferred to a dialysis bag (MWCO: 3 kDa) and dialysis was done against distilled water and PBS. Eventually PBS was replaced with distilled water and the mixture was dried using a freeze-drier.

To prepare HA-ATV NP it was first dissolved in DMSO (8 mg/mL); then solution was transferred to a syringe (needle size G30) and it was added dropwise to Milli-Q water (15 mL) slowly for 15 minutes with stirring speed of 500 rpm. Subsequently, the mixture was transferred to a dialysis bag (MWCO: 3 kDa) to wash off the residue of DMSO. Dialysis was performed 6 time, every 12 hours in distilled water (2 L) at 4 ^{o}C. Then, nanoparticles were characterized for hydrodynamic size and zeta potential using a dynamic light scattering (DLS) Zetasizer Nano zs apparatus (Malvern, U.K.). To prepare FITC labeled HA-ATV-NP 1 mg of FITC was dissolved in HA-ATV solution in DMSO and preparation of nanoparticle was performed as explained above. It is noteworthy to mention that during FITC labelled HA-ATV NP preparation it was protected from light. In addition, dialysis was done in water and PBS until complete removal of FITC. Finally,

the prepared nanoparticles were concentrated using a centrifugal filter (MWCO: 10 kDa) and stored at 4 ^{o}C.

4.11.3. Electrophoresis Gel for HA-ATV Conjugate

Agarose gel (0.8 %) was prepared through dissolving 0.96 gram of agarose in 108 mL of hot water following addition of 12 mL of TAE buffer (10x). Then, pure HA (7 μg) and HA-ATV NP (11.7 μg) was placed on the gel and it was run at 150V for 1 hour. Next, the gel was stained using a freshly prepared Stains-All dye solution (0.005%) in 50% ethanol solution and was kept in dark overnight. Finally, the gel was destained in dark using 20% ethanol solution until HA spots were appeared on the gel.

4.11.4. Radiolabeling of HA-ATV NP with ^{99m}Tc

p-SCN-Bn-DTPA (200 μg) was dissolved in DMSO (10 μL), then it was added to HA-ATV NP solution (10 mg in 1 mL) and stirred overnight. Then *p*-SCN-Bn-DTPA conjugated HA-ATV NP purified by washing through centrifugal filter (MWCO: 10kDa). Next, *p*-SCN-Bn-DTPA conjugated HA-ATV NP (1.5 mg/mL) was mixed with 70 μL of pertechnetate ($^{99m}TcO^{4-}$) solution. Immediately, tin chloride (SnCl2) solution 20 μg in 2 μL of HCl (0.1 M) was added and the mixture was shaken for 30 minutes. Then, the nanoparticle solution was washed with water (4 times) and PBS (5 times) using centrifugal filter MWCO (10 kDa) to remove unbound ^{99m}Tc.

4.11.5. HA-ATV NP Binding with CD44

Each well of a 96 well plate was coated by 100 μL of goat anti human IgG FC γ containing 3μg antibody dispersed in PBS. The plate was kept at 4 ^{o}C overnight while it was sealed to prevent evaporation. Then, wells were washed with 200 μL of PBST solution (0.5% Tween 20) 3 times waiting 1 minute for each wash. Thereafter, microplate wells were incubated with BSA solution

(5% w/v) for 2 hours at 37 ^{o}C to block non-specific binding. Then, wells were washed 3 times using PBST solution (0.5% Tween 20) waiting 1 minute for each wash. After the last wash wells were incubated with 100 µL of CD44 Fc chimera solution (0.2 µg/well, in PBS) for 45 minutes at 37 ^{o}C. Next, wells were washed 3 times (1 minute for each wash) by 200 µL of PBST solution (0.05% Tween 20) and wells were incubated with 100 µL of different concentrations of HA-ATV NP (0.06, 0.125, 0.25, 0.5, 1, 2 and 4 µg/mL) containing 2.5 µg biotinated HA (b-HA) for 2 hours at room temperature. Subsequently, wells were washed 3 times using 200 µL of PBST solution (0.05 % Tween 20) and 2 times with PBS solution (1 minute for each wash). Then, 100 µL of freshly prepared avidin-HRP solution (1:2000 diluted, in 0.2% BSA) was added to each well and incubated for 1 hour at room temperature. Thereafter, wells were washed 3 times using 200 µL of PBST solution (0.05 % Tween) and 2 times with PBS solution (1 minute for each wash). Then, chromogenic TMB solution (100 µL) was added to each well for 15 minutes until blue color was developed. Finally, the reaction was quenched by adding 50 µL of H_2SO_4 (0.5 M) solution and the absorbance at 450 nm wavelength was measured by SpectraMax M3 plate reader.

4.11.6. HA-ATV NP Uptake by RAW264.7 Cells

Cellular uptake of HA-ATV NP by CD44 expressing cells RAW264.7 was examined by FACS analysis at 4 ^{o}C and 37 ^{o}C. Cells were cultured in a 6-well plate in the presence of 5% CO_2 at 37 ^{o}C until they become confluent. Then, fresh medium containing different concentration of FITC labeled HA-ATV NP (33, 66 and 99 µg/mL) was replaced and it was incubated for 1 hour. Thereafter, the medium was removed, and cells were washed with PBS. Next, cells were detached by trypsin following addition of 5 volume of medium to neutralize the trypsin. Then, cells were centrifuged, resuspended in DMEM and transferred to FACS tubes for analysis.

After cellular uptake of FITC labeled HA-ATV NP they were looked by confocal microscopy. RAW264.7 cells (2 x 10^5 cells/mL) were dispersed in DMEM containing FBS (10%) and allowed to grow on a cover glass placed in each well of a 6-well plate overnight. Then, the medium was removed and serum free DMEM containing FITC labeled HA-ATV NP (33 μg/mL) was incubated with cells for 1 hour. Subsequently, lysotracker red (1 μM) was added to each well and incubated for another 1 hour at 37 ^oC. Then, cells were washed 3 times by PBS and 1 mL of formalin solution neutral buffered 10% was added for 15 minutes. After fixation, cells were washed by PBS 3 times and 500 μL of DAPI solution (300 nM) was added for 5 minutes. Then, cells were washed 3 times using PBS and the cover glass was placed over a microscope slide and images were gathered on Nikon C2 confocal microscope.

4.11.7. Evaluating the Role of HA for Cellular Uptake of HA-ATV NP

RAW264.7 cells were cultured in a 6-well plate in the presence of 5% CO_2 at 37 ^oC until complete confluency. Then, free HA (10 mg/mL) was added to the medium and after 30 minutes FITC labeled HA-ATV NP (33 μg/mL) was added and incubated for another 45 minutes. Subsequently, the medium was removed, cells were washed with PBS (3 times) and trypsin was added to detach the cells. Then, 5 volume of DMEM was added to neutralize trypsin; cells were collected by centrifuge (1600 rpm, 5 minutes) and dispersed in DMEM for FACS analysis.

4.11.8. Assessing the Role of CD44 for Uptake of HA-ATV NP in CD44 Expressing Cells

In a 96-well plate RAW264.7 cells were cultured until confluency. Then, cells were fixed by addition of formalin solution neutral buffered 10% and they were washed by PBS 3 times using centrifugation. Subsequently, KM81 antibody (60 μg/mL) was added to the fixed cells dispersed in PBS for 1 hour. Then, cells were sedimented by centrifugation to remove unbound antibody and

incubated with FITC labeled HA-ATV NP for another 1 hour. Finally, cells were washed with PBS and their fluorescent intensity was measured using a plate reader.

4.11.9. Evidence for Cellular Uptake of ATV Through HA-ATV NP

It has been shown that statins become fluorescent after UV light exposure[37]. Then, a solution of HA-ATV NP was kept under UV light (254 nm) for 48 hours. Excitation and emission wavelengths were measured using a spectrophotometer SupraMax. RAW264.7 cells (2 x 10^5 cells/mL) were dispersed in DMEM containing FBS (10%) and allowed to grow on a cover glass placed in each well of a 6-well plate overnight. Then, the medium was removed and serum free DMEM containing UV-irradiated HA-ATV NP (33 μg/mL) was incubated with cells for 1 hour. Then, cells were washed 3 times by PBS and 1 mL of formalin solution neutral buffered 10% was added for 15 minutes. After fixation, cells were washed by PBS 3 times and the cover glass was placed over a microscope slide containing anti-fade solution to prevent sample drying. Images were gathered on Nikon C2 confocal microscope.

4.11.10. Measuring ATV Release from HA-ATV NP

In order to measure ATV release from HA-ATV NP UV absorbance of ATV was measured in a 1:1 ratio of THF/H_20 mixture due to poor solubility of ATV in water. Then, HA-ATV NP dispersed in water was kept in a dialysis bag (MWCO: 3kDa) under constant stirring in the presence of 0.5% (w/v) sodium hydroxide. Subsequently, ATV amount was quantified through measuring UV absorbance (λ=248.5) in different time intervals and the amount of released drug was plotted against time **Figure 4-24**. Calibration curve was obtained by measuring UV absorbance of standards amount of ATV in the THF/H_2O (1:1) solution containing 0.5% sodium hydroxide (v/w).

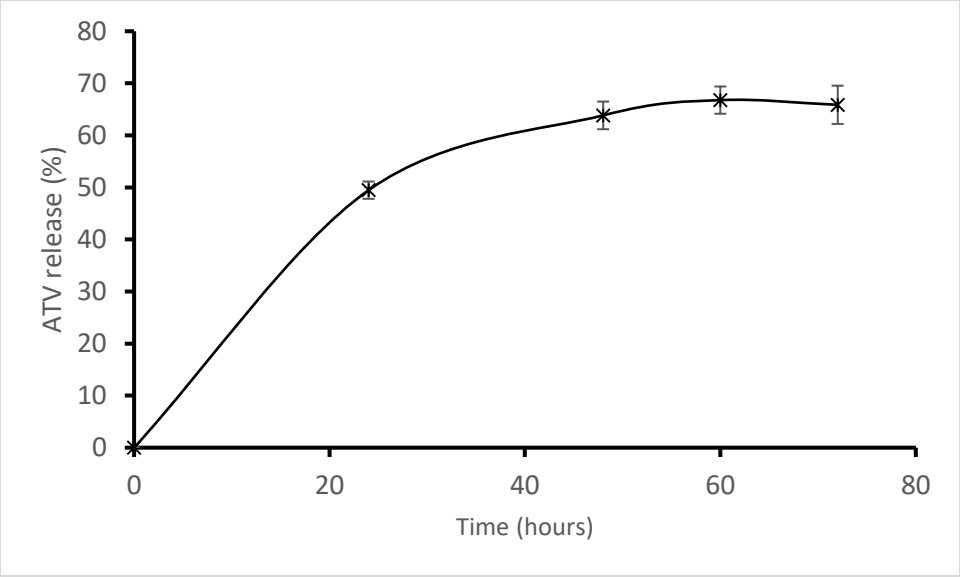

Figure 4-24. ATV Release from HA-ATV NP in basic solution (NaOH 0.5%).

4.11.11. Anti-inflammatory Effects of HA-ATV NP

Mouse macrophage cells (RAW264.7) was used for in vitro studying of anti- inflammatory effects of HA-ATV NP. Cells (2 x 10^5 /well) were dispersed in DMEM medium supplemented with FBS (10%) and Pen Strep (1%) and cultured overnight in a 6-well plate in the presence of 5% CO_2 at 37 ^oC. Then, the medium was removed and FBS free medium containing HA-ATV NP were added and incubated for 15 hours. Subsequently, LPS was added to each well to reach the final concentration of 100 ng/mL and incubated for another 4 hours. Then, the medium was removed, cells were washed with PBS (2 times) and total RNA content of each well was extracted using RNeasy Mini Kit. Immediately, the extracted RNA was purified using a TURBO DNA-free Kit, quantified by NanoDrop and stored at -80 ^oC. cDNA was prepared from purified RNA and used for real time PCR. All the primers for this experiment were purchased from IDT co **Table 4**. In addition to inflammatory genes, the level of inducible nitric oxide synthase iNOS has been

quantified in RAW264.7 cells. For this experiment cells were treated with LPS (100ng/mL) for 1 hour and then HA-ATV NP was added and incubated for 23 hours.

Table 4. Primer sequences of inflammatory genes for rt-PCR study.

gene	forward primer (5´⟶ 3´)	reverse primer (5´ ⟶ 3´)
TNFα	CAGGCGGTGCCTATGTCTC	CGATCACCCCGAAGTTCAGTAG
IL-1b	TTCAGGCAGGCAGTATCACTC	GAAGGTCCACGGGAAAGACAC
IL-1α	CGAAGACTACAGTTCTGCCATT	GACGTTTCAGAGGTTCTCAGAG
ICAM-1	GTGATGCTCAGGTATCCATCCA	CACAGTTCTCAAAGCACAGCG
iNOS	GTTCTCAGCCCAACAATACAAGA	GTGGACGGGTCGATGTCAC

4.11.12. Therapeutic Evaluation of HA-ATV NP In Vivo

For this experiment 20 weeks old ApoE knockout mice were fed a high fat Western diet (TD.88137 Harlan Laboratories) for 6 weeks. The presence of inflammatory atherosclerotic plaques was confirmed through T_2-weighted MRI using HA-NWs that was developed in our group earlier[18]. Then, therapeutic HA-ATV NP containing 8.5 mg ATV per one kg animal body weight was administered to each mouse intravenously every other day for one week. Similarly, PBS solution 100 μL was administered to the control group of mice. In addition, ATV (8.5 mg/kg) was administered orally through an oral gavage to positive control group of mice every other day for one week. Then, mice were sacrificed, and their aorta harvested for further histology studies. Moreover, T_2-weighted MRI images of control and treatment group were collected 24 hours after receiving the last shot of treatment.

4.11.13. Histology Study

Harvested aortas were soaked in 30% sucrose solution overnight. Then, samples were fixed in a freshly prepared formalin solution, processed and embedded in paraffin. Subsequently, aorta samples were sectioned using a rotary microtome and placed on glass slides and dried at 56 ^{o}C overnight. The slides were subsequently deparaffinized in xylene then descending grades of ethyl

alcohol to distilled water were used to hydrate the samples. Next, slides were placed in Tris Buffered Saline (pH=7.4) (Scytek Labs – Logan, UT) for 5 minutes for pH adjustment. Subsequently, sample pretreatment was performed using proteinase K (2%) in TE buffer (pH=8) at room temperature for 3 minutes. Then, the samples were washed several times in distilled water and endogenous peroxidase was blocked utilizing hydrogen peroxide/Methanol (3%) bath for 30 minutes followed by multiple water rinses. Next, pretreatments standard micro-polymer complex staining steps were performed at room temperature on the IntelliPath™ Flex Autostainer. All staining steps are followed by rinses in TBS autowash buffer (Biocare Medical – Concord, CA). After blocking for non-specific protein with Mouse Block (Biocare) for 5 minutes; sections were incubated with rat anti-F4/80 antibody (1:100) in normal antibody diluent (NAD-Scytek) for 60 minutes. Micro-Polymer (Biocare) reagents were subsequently applied for specified incubations (15 minutes probe, 15 minutes polymer) followed by reaction development with Romulin AEC™ (Biocare) for 5 minutes and counterstained with Cat Hematoxylin (1:10) for one minute.

For CD44 staining samples were processed as mentioned above until pH adjustment in TBS buffer (pH=7.4). Then, Heat Induced Epitope Retrieval in Citrate Plus (pH=6.0) (Scytek) performed in vegetable steamer at 100 °C for 30 minutes; followed by 10 minutes room temperature incubation and rinses in several changes of distilled water. Endogenous Peroxidase was blocked utilizing 3% hydrogen peroxide/methanol bath for 30 minutes followed by running tap and distilled water rinses. Following pretreatments standard micro-polymer complex staining steps were performed at room temperature on the IntelliPath™ Flex Autostainer. All staining steps are followed by rinses in TBS autowash buffer (Biocare Medical – Concord, CA). After blocking for non-specific protein with Rodent Block M (Biocare) for 20 minutes; sections were incubated with polyclonal rabbit anti-CD44 antibody (1:400) in normal antibody diluent (NAD-Scytek) for 60 minutes. Micro-

Polymer (Biocare) reagents were subsequently applied followed by reaction development with Romulin AEC™ (Biocare) for 5 minutes and counterstained with Cat Hematoxylin (1:10) for one minute.

4.11.14. Biodistribution Study

^{99m}Tc labeled HA-ATV NP (5 mCi/kg body weight) was administered intravenously to ApoE knockout mice. Activity of syringe content was quantified before and after injection using a dosimeter for precise quantification of administered dose. Comparably, ^{99m}Tc labeled HA-ATV NP was injected to wild type mice. Subsequently, animals were sacrificed two hours after injection; their organs (liver, kidney, spleen, heart, aorta, bone and lung) were collected and the radioactivity was measured using a gamma counter.

REFERENCES

REFERENCES

(1) Weber, C.; Noels, H. Atherosclerosis: current pathogenesis and therapeutic options. *Nature medicine* **2011,** *17* (11), 1410-22.

(2) Mozaffarian, D.; Benjamin, E. J.; Go, A. S.; Arnett, D. K.; Blaha, M. J.; Cushman, M.; Das, S. R.; de Ferranti, S.; Despres, J. P.; Fullerton, H. J.; Howard, V. J.; Huffman, M. D.; Isasi, C. R.; Jimenez, M. C.; Judd, S. E.; Kissela, B. M.; Lichtman, J. H.; Lisabeth, L. D.; Liu, S.; Mackey, R. H.; Magid, D. J.; McGuire, D. K.; Mohler, E. R., 3rd; Moy, C. S.; Muntner, P.; Mussolino, M. E.; Nasir, K.; Neumar, R. W.; Nichol, G.; Palaniappan, L.; Pandey, D. K.; Reeves, M. J.; Rodriguez, C. J.; Rosamond, W.; Sorlie, P. D.; Stein, J.; Towfighi, A.; Turan, T. N.; Virani, S. S.; Woo, D.; Yeh, R. W.; Turner, M. B. Heart Disease and Stroke Statistics-2016 Update: A Report From the American Heart Association. *Circulation* **2016,** *133* (4), e38-360.

(3) van der Wal, A. C.; Becker, A. E.; van der Loos, C. M.; Das, P. K. Site of intimal rupture or erosion of thrombosed coronary atherosclerotic plaques is characterized by an inflammatory process irrespective of the dominant plaque morphology. *Circulation* **1994,** *89* (1), 36-44.

(4) Kwak, B.; Mulhaupt, F.; Myit, S.; Mach, F. Statins as a newly recognized type of immunomodulator. *Nat. Med.* **2000,** *6* (12), 1399-1402.

(5) Sparrow, C. P.; Burton, C. A.; Hernandez, M.; Mundt, S.; Hassing, H.; Patel, S.; Rosa, R.; Hermanowski-Vosatka, A.; Wang, P. R.; Zhang, D.; Peterson, L.; Detmers, P. A.; Chao, Y. S.; Wright, S. D. Simvastatin has anti-inflammatory and antiatherosclerotic activities independent of plasma cholesterol lowering. *Arterioscler. Thromb. Vasc. Biol.* **2001,** *21* (1), 115-121.

(6) Armitage, J. The safety of statins in clinical practice. *Lancet (London, England)* **2007,** *370* (9601), 1781-1790.

(7) Liu, Y.; Cheng, Z.; Ding, L.; Fang, F.; Cheng, K. A.; Fang, Q.; Shi, G. P. Atorvastatin-induced acute elevation of hepatic enzymes and the absence of cross-toxicity of pravastatin. *Int. J. Clin. Pharmacol. Ther.* **2010,** *48* (12), 798-802.

(8) Laufs, U.; Scharnagl, H.; Halle, M.; Windler, E.; Endres, M.; März, W. Treatment Options for Statin-Associated Muscle Symptoms. *Dtsch. Arztebl. Int.* **2015,** *112* (44), 748-755.

(9) Lennernäs, H. Clinical Pharmacokinetics of Atorvastatin. *Clin. Pharmacokinet.* **2003,** *42* (13), 1141-1160.

(10) Hagg, D.; Sjoberg, S.; Hulten, L. M.; Fagerberg, B.; Wiklund, O.; Rosengren, A.; Carlsson, L. M.; Boren, J.; Svensson, P. A.; Krettek, A. Augmented levels of CD44 in macrophages from atherosclerotic subjects: a possible IL-6-CD44 feedback loop? *Atherosclerosis* **2007,** *190* (2), 291-297.

(11) Cuff, C. A.; Kothapalli, D.; Azonobi, I.; Chun, S.; Zhang, Y.; Belkin, R.; Yeh, C.; Secreto, A.; Assoian, R. K.; Rader, D. J.; Pure, E. The adhesion receptor CD44 promotes atherosclerosis by mediating inflammatory cell recruitment and vascular cell activation. *J. Clin. Invest.* **2001,** *108* (7), 1031-1040.

(12) McKee, C. M.; Penno, M. B.; Cowman, M.; Burdick, M. D.; Strieter, R. M.; Bao, C.; Noble, P. W. Hyaluronan (HA) fragments induce chemokine gene expression in alveolar macrophages. The role of HA size and CD44. *J. Clin. Investig.* **1996,** *98* (10), 2403-2413.

(13) Jain, M.; He, Q.; Lee, W. S.; Kashiki, S.; Foster, L. C.; Tsai, J. C.; Lee, M. E.; Haber, E. Role of CD44 in the reaction of vascular smooth muscle cells to arterial wall injury. *J. Clin. Investig.* **1996,** *97* (3), 596-603.

(14) Zhao, L.; Lee, E.; Zukas, A. M.; Middleton, M. K.; Kinder, M.; Acharya, P. S.; Hall, J. A.; Rader, D. J.; Pure, E. CD44 expressed on both bone marrow-derived and non-bone marrow-derived cells promotes atherogenesis in ApoE-deficient mice. *Arterioscler. Thromb. Vasc. Biol.* **2008,** *28* (7), 1283-1289.

(15) Zhao, L.; Hall, J. A.; Levenkova, N.; Lee, E.; Middleton, M. K.; Zukas, A. M.; Rader, D. J.; Rux, J. J.; Pure, E. CD44 regulates vascular gene expression in a proatherogenic environment. *Arterioscler. Thromb. Vasc. Biol.* **2007,** *27* (4), 886-892.

(16) Krettek, A.; Sukhova, G. K.; Schonbeck, U.; Libby, P. Enhanced expression of CD44 variants in human atheroma and abdominal aortic aneurysm: possible role for a feedback loop in endothelial cells. *Am. J. Pathol.* **2004,** *165* (5), 1571-1581.

(17) Kolodgie, F. D.; Burke, A. P.; Farb, A.; Weber, D. K.; Kutys, R.; Wight, T. N.; Virmani, R. Differential accumulation of proteoglycans and hyaluronan in culprit lesions: insights into plaque erosion. *Arteriosclerosis, thrombosis, and vascular biology* **2002,** *22* (10), 1642-8.

(18) Hossaini Nasr, S.; Tonson, A.; El-Dakdouki, M. H.; Zhu, D. C.; Agnew, D.; Wiseman, R.; Qian, C.; Huang, X. Effects of Nanoprobe Morphology on Cellular Binding and Inflammatory Responses: Hyaluronan-Conjugated Magnetic Nanoworms for Magnetic Resonance Imaging of Atherosclerotic Plaques. *ACS Appl. Mater. Interfaces* **2018,** *10* (14), 11495-11507.

(19) El-Dakdouki, M. H.; Pure, E.; Huang, X. Development of drug loaded nanoparticles for tumor targeting. Part 2: Enhancement of tumor penetration through receptor mediated transcytosis in 3D tumor models. *Nanoscale* **2013,** *5* (9), 3904-3911.

(20) El-Dakdouki, M. H.; Pure, E.; Huang, X. Development of drug loaded nanoparticles for tumor targeting. Part 1: Synthesis, characterization, and biological evaluation in 2D cell cultures. *Nanoscale* **2013,** *5* (9), 3895-3903.

(21) El-Dakdouki, M. H.; El-Boubbou, K.; Kamat, M.; Huang, R.; Abela, G. S.; Kiupel, M.; Zhu, D. C.; Huang, X. CD44 targeting magnetic glyconanoparticles for atherosclerotic plaque imaging. *Pharm. Res.* **2014,** *31* (6), 1426-1437.

(22) Gochman, E.; Mahajna, J.; Shenzer, P.; Dahan, A.; Blatt, A.; Elyakim, R.; Reznick, A. Z. The expression of iNOS and nitrotyrosine in colitis and colon cancer in humans. *Acta histochemica* **2012,** *114* (8), 827-835.

(23) Detmers, P. A.; Hernandez, M.; Mudgett, J.; Hassing, H.; Burton, C.; Mundt, S.; Chun, S.; Fletcher, D.; Card, D. J.; Lisnock, J.; Weikel, R.; Bergstrom, J. D.; Shevell, D. E.; Hermanowski-Vosatka, A.; Sparrow, C. P.; Chao, Y. S.; Rader, D. J.; Wright, S. D.; Pure, E. Deficiency in inducible nitric oxide synthase results in reduced atherosclerosis in apolipoprotein E-deficient mice. *J. Immunol.* **2000,** *165* (6), 3430-3435.

(24) Huang, H.; Koelle, P.; Fendler, M.; Schrottle, A.; Czihal, M.; Hoffmann, U.; Conrad, M.; Kuhlencordt, P. J. Induction of inducible nitric oxide synthase (iNOS) expression by oxLDL inhibits macrophage derived foam cell migration. *Atherosclerosis* **2014,** *235* (1), 213-222.

(25) Zhao, J. F.; Shyue, S. K.; Lin, S. J.; Wei, J.; Lee, T. S. Excess nitric oxide impairs LXR(alpha)-ABCA1-dependent cholesterol efflux in macrophage foam cells. *J. Cell. Physiol.* **2014,** *229* (1), 117-125.

(26) Meir, K. S.; Leitersdorf, E. Atherosclerosis in the apolipoprotein-E-deficient mouse: a decade of progress. *Arterioscler. Thromb. Vasc. Biol.* **2004,** *24* (6), 1006-1014.

(27) Maiti, A.; Maki, G.; Johnson, P. TNF-alpha induction of CD44-mediated leukocyte adhesion by sulfation. *Science (New York, N.Y.)* **1998,** *282* (5390), 941-3.

(28) Nakhlband, A.; Eskandani, M.; Omidi, Y.; Saeedi, N.; Ghaffari, S.; Barar, J.; Garjani, A. Combating atherosclerosis with targeted nanomedicines: recent advances and future prospective. *BioImpacts : BI* **2018,** *8* (1), 59-75.

(29) Kircher, M. F.; Grimm, J.; Swirski, F. K.; Libby, P.; Gerszten, R. E.; Allport, J. R.; Weissleder, R. Noninvasive in vivo imaging of monocyte trafficking to atherosclerotic lesions. *Circulation* **2008,** *117* (3), 388-395.

(30) Tarin, C.; Carril, M.; Martin-Ventura, J. L.; Markuerkiaga, I.; Padro, D.; Llamas-Granda, P.; Moreno, J. A.; Garcia, I.; Genicio, N.; Plaza-Garcia, S.; Blanco-Colio, L. M.; Penades, S.; Egido, J. Targeted gold-coated iron oxide nanoparticles for CD163 detection in atherosclerosis by MRI. *Scientific reports* **2015,** *5*, 17135.

(31) Röhrl, C.; Stangl, H. HDL endocytosis and resecretion(). *Biochimica et biophysica acta* **2013,** *1831* (11), 1626-1633.

(32) Kuai, R.; Li, D.; Chen, Y. E.; Moon, J. J.; Schwendeman, A. High-Density Lipoproteins (HDL) – Nature's Multi-Functional Nanoparticles. *ACS Nano* **2016,** *10* (3), 3015-3041.

(33) Duivenvoorden, R.; Tang, J.; Cormode, D. P.; Mieszawska, A. J.; Izquierdo-Garcia, D.; Ozcan, C.; Otten, M. J.; Zaidi, N.; Lobatto, M. E.; van Rijs, S. M.; Priem, B.; Kuan, E. L.; Martel, C.; Hewing, B.; Sager, H.; Nahrendorf, M.; Randolph, G. J.; Stroes, E. S.; Fuster, V.; Fisher, E. A.; Fayad, Z. A.; Mulder, W. J. A statin-loaded reconstituted high-density lipoprotein nanoparticle inhibits atherosclerotic plaque inflammation. *Nat. Commun.* **2014,** *5*, 3065.

(34) Ratchford, E. V.; Gutierrez, J.; Lorenzo, D.; McClendon, M. S.; Della-Morte, D.; DeRosa, J. T.; Elkind, M. S. V.; Sacco, R. L.; Rundek, T. Short-term Effect of Atorvastatin on Carotid Artery Elasticity: A Pilot Study. *Stroke* **2011,** *42* (12), 3460-3464.

(35) Lameijer, M.; Binderup, T.; van Leent, M. M. T.; Senders, M. L.; Fay, F.; Malkus, J.; Sanchez-Gaytan, B. L.; Teunissen, A. J. P.; Karakatsanis, N.; Robson, P.; Zhou, X.; Ye, Y.; Wojtkiewicz, G.; Tang, J.; Seijkens, T. T. P.; Kroon, J.; Stroes, E. S. G.; Kjaer, A.; Ochando, J.; Reiner, T.; Pérez-Medina, C.; Calcagno, C.; Fisher, E. A.; Zhang, B.; Temel, R. E.; Swirski, F. K.; Nahrendorf, M.; Fayad, Z. A.; Lutgens, E.; Mulder, W. J. M.; Duivenvoorden, R. Author Correction: Efficacy and safety assessment of a TRAF6-targeted nanoimmunotherapy in atherosclerotic mice and non-human primates. *Nat. Biomed. Eng.* **2018,** *2* (8), 623-623.

(36) Kamat, M.; El-Boubbou, K.; Zhu, D. C.; Lansdell, T.; Lu, X.; Li, W.; Huang, X. Hyaluronic acid immobilized magnetic nanoparticles for active targeting and imaging of macrophages. *Bioconjugate chemistry* **2010,** *21* (11), 2128-35.

(37) Montanaro, S.; Lhiaubet-Vallet, V.; Iesce, M. I.; Previtera, L.; Miranda, M. A. A mechanistic study on the phototoxicity of atorvastatin: singlet oxygen generation by a phenanthrene-like photoproduct. *Chem. Res. Toxicol.* **2009,** *22* (1), 173-178.